

A KERNEL BASED HIGH ORDER EXPLICIT UNCONDITIONALLY STABLE
CONSTRAINED TRANSPORT METHOD FOR IDEAL AND NON-IDEAL
MAGNETOHYDRODYNAMICS

By

Firat Cakir

A DISSERTATION

Submitted to
Michigan State University
in partial fulfillment of the requirements
for the degree of

Mathematics — Doctor of Philosophy

2020

ABSTRACT

A KERNEL BASED HIGH ORDER EXPLICIT UNCONDITIONALLY STABLE CONSTRAINED TRANSPORT METHOD FOR IDEAL AND NON-IDEAL MAGNETOHYDRODYNAMICS

By

Firat Cakir

The Magnetohydrodynamics (MHD) model is an important model to describe the behavior of the plasma phenomenon. The MHD equations are challenging because one needs to maintain the divergence free condition, $\nabla \cdot \mathbf{B} = 0$. Many numerical methods have been developed to enforce this condition. In this thesis we propose a hybrid MHD solver via the constrained transport method which is based on kernel based approximations to correct the solution of magnetic field equation so that it satisfies the divergence free condition. The main focus of this work is on the constrained transport methodology that intends to eliminate the need of artificial diffusion limiters (introduced in the previous work [29]) for the magnetic vector potential equation for ideal MHD and extend the proposed scheme to resistive MHD, which includes a term that takes the form of diffusion.

In the first part of the thesis, we focus on ideal MHD model and we further our work on mesh aligned constrained transport [29] by developing a new kernel based approach for the vector potential in 2D and 3D. The approach for solving the vector potential is based on the method of lines transpose and is A-stable, eliminating the need for diffusion limiters needed in our previous work in 3D. The work presented here is an improvement over the previous method in the context of problems with strong shocks due to the fact that we could eliminate the diffusion limiter that was needed in our previous version of constrained transport. The method is robust and has been tested on the 2D and 3D cloud shock, blast wave and field loop problems.

In the second part of the thesis, we turn our focus to resistive MHD model, which allows magnetic diffusion terms in the magnetic field induction equation. We derive magnetic potential equation with diffusion terms and develop our kernel based method for the second order derivative terms appearing in the magnetic potential equation. We update the magnetic field solutions using the constrained transport framework based on our novel kernel based scheme. Our novel scheme is robust and unconditionally stable. Numerical examples in 2D are provided to verify the order of accuracy and to test the performance of the proposed scheme.

ACKNOWLEDGMENTS

First and foremost, I would like to express my deepest and sincere gratitude to my advisor, Dr. Andrew Christlieb, for his continuous support and encouragement throughout my Ph.D study and related research. Andrew provided me tremendous knowledge, great insight, motivation, patient guidance and pleasant research environment. His guidance helped me in all the time of research and writing this thesis. I could not have imagined having a better advisor and mentor for my Ph.D study. It was also truly helpful to have weekly meetings with my advisor and other group members to discuss over the works with them. Besides my advisor, I would like to thank to Yan Jiang, Hyoseon Yang for their close collaborations and to William Sand for the help he offered me. I would also like to thank to my dissertation committee: Dr. Yingda Cheng, Dr. Qian Jianliang, and Dr. Brian O'Shea for their insightful comments and encouragement.

I am eternally grateful to my wife, Hayriye, for her support, encouragement, patience and endless love she has for me. I wouldn't have made it without her support, help and love. I always consider her as my life mentor. I love you my beautiful wife! I also want to express my deepest love to my lovely kids, Miran Aras and Nehir Lavin. Their existence made my life more meaningful. I also want to thank to the rest of my family: my parents, my parents in law, my siblings and my siblings in law, for their endless love, support and prayers. They have always been there for me and I have always felt their love in my heart. I am truly thankful to my mom for her continuous praying and love to me. Moreover, I would like to thank my special friends Ayse and Metin for their great friendship and support.

Last but not least, I am beyond words in my gratitude to Allah.

TABLE OF CONTENTS

| | |
|--|-------------|
| LIST OF TABLES | vii |
| LIST OF FIGURES | viii |
| Chapter 1 Introduction | 1 |
| 1.1 Outline of the Thesis | 1 |
| 1.2 Plasma Phenomenon | 3 |
| 1.3 Theoretical Overview of Plasma | 4 |
| 1.4 Review of Previous Work | 12 |
| 1.4.1 Numerical Methods for Hyperbolic Conservation Laws | 12 |
| 1.4.2 Numerical Methods for ideal MHD | 13 |
| 1.4.3 Method of Lines Transpose | 17 |
| 1.4.4 Numerical Methods for non-ideal MHD | 18 |
| Chapter 2 The Ideal MHD Equations | 21 |
| 2.1 The Ideal MHD Equations | 21 |
| 2.1.1 Hyperbolicity of the governing equations | 22 |
| 2.2 Overview of the Base Scheme WENO-HCL | 23 |
| 2.3 Magnetic potential in 3D | 27 |
| 2.3.1 Magnetic potential in 2D | 30 |
| 2.4 The advantage of MOLT based current method over WENO-HJ method | 31 |
| 2.5 Outline of the constrained transport methodology | 33 |
| Chapter 3 Kernel Based Approximation with Constrained Transport for Ideal MHD | 36 |
| 3.1 Hamilton-Jacobi equations | 37 |
| 3.1.1 1D Hamilton-Jacobi equations | 37 |
| 3.1.2 Approximation of the first order derivative ∂_x | 38 |
| 3.1.2.1 Periodic boundary conditions | 41 |
| 3.1.2.2 Non periodic boundary conditions | 44 |
| 3.1.2.3 Space Discretization and WENO-based Quadrature | 46 |
| 3.1.3 2D magnetic potential equation | 51 |
| 3.1.4 3D magnetic potential equation | 54 |
| 3.2 Central finite difference discretization of $\nabla \times \mathbf{A}$ | 55 |
| 3.2.1 Curl in 2D | 56 |
| 3.2.2 Curl in 3D | 56 |
| 3.3 Positivity Limiter | 57 |
| 3.4 Numerical Results | 61 |
| 3.4.1 Smooth vortex test in MHD | 61 |
| 3.4.2 2D Orszag-Tang Vortex | 62 |
| 3.4.3 Cloud Shock | 64 |

| | | |
|---------------------|--|------------|
| 3.4.4 | 2D Blast wave | 65 |
| 3.4.5 | 2D Field Loop | 68 |
| 3.4.6 | 3D Field Loop | 68 |
| 3.4.7 | 3D Blast wave | 70 |
| 3.4.8 | Kernel-based method with Diffusion Terms | 71 |
| Chapter 4 | MOLT for PEC for ideal MHD | 76 |
| 4.1 | MOLT for PEC for ideal MHD | 76 |
| 4.1.1 | Derivation of the Boundary Conditions for MOLT for Dirichlet BC | 78 |
| 4.2 | Hartmann Flow | 81 |
| 4.2.1 | Numerical Results for ideal MHD with PEC Boundary Conditions | 84 |
| Chapter 5 | Non-Ideal MHD Equations | 87 |
| 5.1 | NON- IDEAL MHD | 87 |
| 5.2 | Magnetic Vector Potential Formulation for Resistive MHD | 89 |
| 5.3 | Outline for Constrained Transport Framework for Non-ideal MHD | 93 |
| Chapter 6 | Kernel Based Approximation with Constrained Transport for Resistive MHD | 96 |
| 6.1 | Hamilton Jacobi with Diffusion terms | 97 |
| 6.2 | Approximation of the second order derivative ∂_{xx} | 97 |
| 6.2.0.1 | Periodic boundary conditions | 101 |
| 6.3 | Numerical Results for Resistive MHD for Periodic Boundary Condition | 101 |
| 6.3.1 | Refinement Study for Smooth Vortex Problem | 102 |
| 6.3.2 | Smooth Vortex Problem for Resistive MHD | 103 |
| 6.4 | Orszag Tang Vortex problem for Resistive MHD | 106 |
| 6.4.1 | Refinement Study for Orszag Tang Vortex problem for Resistive MHD | 106 |
| 6.4.2 | Orszag Tang Vortex problem with diffusion for Resistive MHD | 107 |
| Chapter 7 | MOLT for PEC for non-ideal MHD Equations | 110 |
| 7.1 | MOLT for PEC for non-ideal MHD | 110 |
| 7.2 | Numerical results for Hartmann Flow problem with diffusion | 111 |
| 7.3 | Magnetic reconnection: GEM challenge problem | 112 |
| Chapter 8 | Conclusion and Future Work | 119 |
| 8.1 | Conclusion | 119 |
| 8.2 | Future Work | 121 |
| APPENDIX | | 122 |
| BIBLIOGRAPHY | | 125 |

LIST OF TABLES

| | |
|---|-----|
| Table 3.1: $\beta_{k,\max}$ in Theorem 3.1.2 for $k = 1, 2, 3$ | 43 |
| Table 3.2: Smooth vortex problem. Errors of B and orders of accuracy. | 63 |
| Table 4.1: Hartmann Flow for ideal MHD. Errors of B and orders of accuracy. . . . | 84 |
| Table 6.1: Smooth vortex problem. Errors of A and orders of accuracy. | 103 |
| Table 6.2: Errors of A and orders of accuracy. | 107 |
| Table 6.3: Errors of A and orders of temporal accuracy. | 107 |
| Table 7.1: Hartmann flow problem. Errors of A and orders of accuracy. | 112 |

LIST OF FIGURES

| | | |
|--------------|---|----|
| Figure 3.1: | The structure of the stencils in WENO integration. | 48 |
| Figure 3.2: | Smooth vortex problem. L^2 norms of \mathbf{u} and \mathbf{B} at $t = 20$ with 160×160 grid points. Domain for the plots is $[-5, 5] \times [-5, 5]$ | 64 |
| Figure 3.3: | Orszag-Tang vortex problem. Contour plots of density at $t = 3$ with 192×192 grid points. | 65 |
| Figure 3.4: | Cloud shock problem. Contour plots of $\ \mathbf{B}\ $ at $t = 0.06$ with 512×512 grid points. | 66 |
| Figure 3.5: | 2D Blast wave problem. Contour plots at time $t = 0.01$ with 256×256 grid points. (a) density; (b) pressure; (c) the norm of \mathbf{u} ; (d) magnetic pressure $\ \mathbf{B}\ $ | 67 |
| Figure 3.6: | 2D Field loop. Contour plots at time $t = 1$ with 128×128 grid points. a) Magnetic Pressure $\ \mathbf{B}\ $; b) Magnetic Potential A^3 | 69 |
| Figure 3.7: | 3D Field loop. Contour plots at time $t = 1$ with 128×128 grid points. The loop has been advected around the grid once. a) Magnetic Pressure; b) Magnetic Potential. | 70 |
| Figure 3.8: | 3D Blast wave problem. Contour plots at time $t = 0.01$ with 150×150 grid points. | 72 |
| Figure 3.9: | 3D Blast wave problem. Contour plots at time $t = 0.01$ with 150×150 grid points. While the max $\ \mathbf{u}\ $ value for previous method is 261, it is 320 for the kernel-based method. Note that this is 23% higher than the old method, and is far less isotropic around the peak than the old method. | 73 |
| Figure 3.10: | 3D Blast wave from the kernel based method with having added the diffusion limiter. The max $\ \mathbf{u}\ $ value is 265. We note that these results are nearly identical to the old WENO-HJ method, which required the diffusion limiter. | 75 |
| Figure 4.1: | Sketch of a Hartmann type of flow [58]. | 83 |
| Figure 4.2: | 1D cross-sections of Hartmann problem for $Ha = 10$ at $t = 1$ with 128×128 | 85 |
| Figure 4.3: | Velocity profile for the Hartmann problem for $Ha = 10$ in 2D at $t = 1$ with 128×128 | 85 |

| | | |
|-------------|---|-----|
| Figure 4.4: | Induced magnetic field for the Hartmann problem for $Ha = 10$ at $t = 1$ with 128×128 | 86 |
| Figure 4.5: | Magnetic potential A for the Hartmann problem at $Ha = 10$ | 86 |
| Figure 6.1: | (FD) Contour plots of $\ \mathbf{B}\ $ at time $t = 20$ with $\Delta x = \Delta y = 0.2$ | 104 |
| Figure 6.2: | (Kernel based method) Contour plots of $\ \mathbf{B}\ $ at time $t = 20$ with $\Delta x = \Delta y = 0.2$ | 105 |
| Figure 6.3: | (FD) Contour plots of ρ at time $t = 3$ with 192×192 | 108 |
| Figure 6.4: | (MOLT) Contour plots of ρ at time $t = 20$ with 192×192 | 109 |
| Figure 7.1: | Velocity profile for the Hartmann problem at $Ha = 0, 2, 5, 10$ | 113 |
| Figure 7.2: | Exact and Numerical velocity solutions for the Hartmann problem at $Ha = 0, 2, 5, 10$ | 114 |
| Figure 7.3: | Induced magnetic field for the Hartmann problem at $Ha = 0, 2, 5, 10$. . . | 115 |
| Figure 7.4: | Exact and Numerical induced magnetic field solutions for the Hartmann problem at $Ha = 0, 2, 5, 10$ | 116 |
| Figure 7.5: | Magnetic Reconnection in Space. Credits: NASA | 117 |
| Figure 7.6: | Breaking and rejoining of magnetic field lines due to the presence of localized diffusion region (shaded). (Priest, E. R [63]) | 118 |
| Figure 7.7: | GEM Magnetic Reconnection Problem for diffusion $\eta = 0.001$ | 118 |

Chapter 1

Introduction

1.1 Outline of the Thesis

In this thesis, our first intention is to develop a hybrid Magnetohydrodynamics (MHD) solver to solve ideal MHD so that the solutions satisfy the divergence free constraint. Our second goal is to extend a similar approximation to the non-ideal MHD models, in particular to the resistive MHD model. In this section we will explain how this thesis is organized.

In Chapter 2, we briefly review the ideal MHD equations and the evolution of the magnetic vector equations with respect to magnetic potential equations. We propose the steps of our version of the constrained transpose framework, which is based on the our novel kernel based approximation scheme. Our proposed schemes are coupled with base-scheme weighted essentially non-oscillatory (WENO) with the kernel based scheme for the constrained transport (CT) methodology. Also, we give a short overview of WENO scheme which is designed to solve Hyperbolic Conservation Laws [48], which we refer as WENO-HCL. Note that this thesis is not about WENO, however WENO-HCL is a main tool we use in developing our solver.

In Chapter 3, we represent our novel kernel based numerical scheme for 1D Hamilton-Jacobi equations and present how we transform the first spatial derivative terms via convolution integrals. We develop a novel MOLT-HJ solver to address the Hamilton Jacobi

equations as a part of our MHD solver in 2D and 3D as well as the WENO-based quadrature formulation. The main advantage of the proposed scheme is to be able to avoid the artificial diffusion terms, which were needed in the previous work [29]. Moreover, the stability analysis is shown for the linear problems. Several test problems in 2D and 3D are presented in the numerical results section to verify the order of accuracy and to show the robustness of the scheme. We compare the new method with the old method to validate that the new method works well. We observe that the limiter needed in the 3D vector potential in the old method is causing a change in the structure of the solutions in the context of the strong shocks, while the new method conserve the solution structure for the problems with strong shocks, in particular for the blast wave problem.

In Chapter 4, we introduce our proposed scheme with respect to PEC boundary conditions and show it is equivalent to enforce Dirichlet boundary conditions. In fact, we develop the Dirichlet boundary conditions for magnetic potential in MOLT-HJ. Then, we go over the derivation of an important benchmark problem, Hartmann Flow problem [58]. Hartmann Flow problem is a well known test problem to check PEC boundary conditions. Our proposed kernel based scheme in the context of PEC boundary conditions are tested via the Hartmann Flow problem. We demonstrate that we could get high order accuracy and compare the numerical solutions with the analytical solutions.

In Chapter 5, we extend the MHD model to include diffusion terms in the magnetic field equation. Then we derive a set of magnetic potential equations for the new case of having diffusion terms in the magnetic field equation. Later, the constrained transport strategy for the case of resistive MHD is presented.

In Chapter 6, we extend the MOLT-HJ solver to include magnetic diffusion terms. We present kernel based representations for the second order spatial derivative terms in the

magnetic potential equation. Such representations are based on a successive convolution. Then we test the scheme with 2D benchmark problems to test our proposed method with respect to periodic boundary conditions.

In Chapter 7, we then present kernel based method for PEC boundary condition in the case of resistive MHD. We then work on several test problems such as Hartmann Flow and GEM Magnetic Reconnection problem. And in Chapter 8, we conclude with a brief discussion about the conclusions.

In the next section, we will explain the plasma phenomenon and then present some important models, which describe the behavior of plasma. We especially derive the equations for the MHD model. In the rest of this chapter we will present a literature review.

1.2 Plasma Phenomenon

One of the most common but least understood phenomenon in the universe is plasma. A plasma is a collection of charged particles, containing many interacting free electrons and ionized atoms or molecules which are obtained by heating a gas until it breaks down into its constitutive elements. A plasma is the fourth state of the matter: solid, liquid, gas, and plasma. The primary differences among solids, liquids, gases and plasmas are based on the molecular relationships between the particles in the states. The strength of the bonds that hold their constituent particles together is strong in a solid state, moderate in liquid state, and weak in the gaseous state. The thermal energy (random kinetic energy) level of the particles and the strength of the binding forces determines the state of a given substance. Applying a high enough constant temperature to a solid or liquid substance generates thermal kinetic energy to the molecules such that they exceed the binding potential energy and this

leads to red a phase transition. However, in the sense of thermodynamics, the transition from a gas to a plasma is not considered as a phase transition since a plasma occurs by heating a substance with gradually increasing temperature until a reasonable high fractional ionization is produced.

The particle interactions determine the properties of a plasma. For example, a basic feature of a plasma is that charged particles simultaneously interact each other over long distances, which is a distinct behavior of a plasma from ordinary fluids and solids. Since the particles in a plasma are interacting with electromagnetic fields, this provides many novel phenomena that do not exist in fluids or solids. A significant feature of a plasma is the ability to have a various wave phenomena. Therefore, the studies of waves in plasma present important information on plasma properties.

The plasma state commonly exists in the Universe. For example, common instances of matter in the plasma state are stars and galaxies. There are a range of man made plasma applications including thermonuclear fusion reactions, which is a possible source of energy; the magnetohydrodynamic generator, which converts kinetic energy of a plasma into electrical energy (MHD); and plasma propulsion systems for space propulsion.

1.3 Theoretical Overview of Plasma

The plasma dynamics is defined by the interaction between the plasma charged particles with internal and external fields. The motion of the charged particles can generate electric fields and magnetic fields. The dynamic behavior of the particles in plasma is described by the classical (non-quantum) mechanics laws. The *Lorentz Force* gives the interaction of charged particles with electromagnetic fields. For a particle with charge q , the motion of the

equation is

$$\frac{d\mathbf{p}}{dt} = q(\mathbf{E} + \mathbf{v} \times \mathbf{B}), \quad (1.3.1)$$

where m is mass, \mathbf{v} is the velocity of the moving particle, \mathbf{E} is the electric field and \mathbf{B} is the magnetic field, and $\mathbf{p} = m\mathbf{v}$ denotes the particle momentum. The dynamics of a plasma are described by solving the equation of motion for the each charged particle under the combined effect of the internally generated fields by all the other particles and external fields. For N number particles, N nonlinear coupled motion equations needs to be solved simultaneously. The electromagnetic fields are governed by the *Maxwell equations*

$$\nabla \times \mathbf{E} = -\frac{\partial \mathbf{B}}{\partial t}, \quad (1.3.2)$$

$$\nabla \times \mathbf{B} = \mu_0(\mathbf{J} + \epsilon_0 \frac{\partial \mathbf{E}}{\partial t}), \quad (1.3.3)$$

$$\nabla \cdot \mathbf{E} = \frac{\rho}{\epsilon_0}, \quad (1.3.4)$$

$$\nabla \cdot \mathbf{B} = 0, \quad (1.3.5)$$

where ρ is the total charge density, \mathbf{J} is the total electric current density, ϵ_0 is the electric permittivity, and μ_0 is the magnetic permeability of free space.

There are several different choices of approximations for the theoretical description of plasma phenomenon. Each of these models applies to different situations of plasma.

The first choice is to use a kinetic model of the plasma which is based on the distribution function for the system of particles at each point. The kinetic equations that describe the evolution of the distribution function in phase space are 6D plus time. One example of differential kinetic equations to describe plasma is the Boltzmann equation. It governs the

evolution of a probability density function $f_\alpha(t, x, v)$ of plasma species α in phase space (x, v) at a given time t . The function $f_\alpha(t, x, v)$ is also called the distribution function in phase space and represents the possibility of density of representative points of particles in phase space.

Another approach is two-fluid modeling, which is based on a local distribution function for each species. If there exists a very frequent collisions between the plasma particles, then each species (electrons and ions) can be considered as a fluid described by a local variables such as density, velocity and temperature. In this two fluid model, there exist conservation of mass, conservation of momentum, and conservation of energy for each species in the plasma.

A third model is magnetohydrodynamic (MHD), which is single fluid model, which treats two-fluid models as a single conducting fluid using unified macroscopic variables and their related conservation equations. Thus, the single fluid model is a set of coupled equations of two-fluid model equations, which is simpler to study. Single fluid model is less complete, but it is still gives important information about the behavior of a plasma.

The MHD model is applicable to the studies of highly conducting fluid plasmas engaged with magnetic fields. It's a model to understand the solar and stellar winds and transport of plasmas inside magnetospheres.

The derivation of fluid models from the Boltzmann equation requires the introduction of a "closure" model. This "closure" model is a key weakness in a fluid model because it introduces assumptions about the behavior of the underlying micro scale physics, but is necessary to arrive at a finite set of moments. Now we briefly show the general strategy to derive the fluid equations from kinetic equations, [12, 60].

Mathematically, the Boltzmann equation is as follows

$$\frac{\partial f_\alpha}{\partial t} + \mathbf{v} \cdot \nabla f_\alpha + \mathbf{a}_\alpha \cdot \nabla_{\mathbf{v}} f_\alpha = \left(\frac{\partial f_\alpha}{\partial t} \right)_{coll}, \quad (1.3.6)$$

with the acceleration

$$\mathbf{a}_\alpha = \frac{\mathbf{F}_\alpha}{m_\alpha} = \frac{q_\alpha}{m_\alpha} (\mathbf{E} + \mathbf{v} \times \mathbf{B}), \quad (1.3.7)$$

where m_α is the mass of species α and q_α is the charge of α . The term at the right hand side of the Boltzmann equation $\left(\frac{\partial f_\alpha}{\partial t} \right)_{coll}$ describes the changes of plasma due to particle collisions and is called a general collision operator. Also note that in the case where the collisions in particles are neglected, $\left(\frac{\partial f_\alpha}{\partial t} \right)_{coll} = 0$, the Boltzmann equation (1.3.6) is called the Vlasov equation.

The Boltzmann equation is multiplied by a weight function $\chi(\mathbf{v})$ and then the resulting equation is integrated with respect to the velocity space

$$\int \chi \left(\frac{\partial f_\alpha}{\partial t} + \mathbf{v} \cdot \nabla f_\alpha + \mathbf{a}_\alpha \cdot \nabla_{\mathbf{v}} f_\alpha \right) d\mathbf{v} = \int \chi \left(\frac{\partial f_\alpha}{\partial t} \right)_{coll} d\mathbf{v}. \quad (1.3.8)$$

These weight functions $\chi(\mathbf{v})$ represent some physical features of particles in plasma. By properly choosing the function $\chi(\mathbf{v})$, we end up with continuity equation, the momentum equation, and the energy equation. More precisely, if $\chi(\mathbf{v}) = m_\alpha$, we get the continuity equation, if $\chi(\mathbf{v}) = m_\alpha \mathbf{v}$, we get the momentum equation, and if $\chi(\mathbf{v}) = \frac{1}{2} m_\alpha \mathbf{v}^2$, we get the energy equation. Consequently, there is a system of transport equations for each α species since a plasma consists of multiple particle species such as electrons, ions, and

neutral particles. If we denote $\langle \chi \rangle_\alpha$ as the average over \mathbf{v} -space as

$$\langle \chi \rangle_\alpha = \int \chi f_\alpha d\mathbf{v}, \quad (1.3.9)$$

then we obtain the system of transport equations as follows

$$\frac{\partial \rho_\alpha}{\partial t} + \nabla \cdot (\rho_\alpha \mathbf{u}_\alpha) = \left(\frac{\partial \rho_\alpha}{\partial t} \right)_{coll}, \quad (1.3.10)$$

$$\rho_\alpha \left[\frac{\partial \mathbf{u}_\alpha}{\partial t} + (\mathbf{u}_\alpha \cdot \nabla) \mathbf{u}_\alpha \right] + \nabla \cdot (\mathbf{P}_\alpha) - \langle \mathbf{F}_\alpha \rangle_\alpha = m_\alpha \int \mathbf{v} \left(\frac{\partial f_\alpha}{\partial t} \right)_{coll} d\mathbf{v}, \quad (1.3.11)$$

$$\frac{\partial \epsilon_\alpha}{\partial t} + \nabla \cdot (\epsilon_\alpha \mathbf{u}_\alpha) + \nabla \cdot (\mathbf{P}_\alpha \cdot \mathbf{u}_\alpha) - n_\alpha q_\alpha \mathbf{u}_\alpha \cdot \mathbf{E} = \frac{1}{2} m_\alpha \int \|\mathbf{v}\|^2 \left(\frac{\partial f_\alpha}{\partial t} \right)_{coll} d\mathbf{v}, \quad (1.3.12)$$

where the right hand side of the above equations are collision terms. The fluid unknown quantities are the mass density $\rho_\alpha = n_\alpha m_\alpha = m_\alpha \langle 1 \rangle_\alpha$, the momentum density $\rho_\alpha \mathbf{u}_\alpha = \rho_\alpha \langle \mathbf{v} \rangle_\alpha$, and the energy density

$$\epsilon_\alpha = \frac{p_\alpha}{\gamma - 1} + \frac{1}{2} \rho_\alpha \|\mathbf{u}_\alpha\|^2, \quad (1.3.13)$$

where γ is the ideal gas constant, and $\mathbf{P}_\alpha = m_\alpha \langle (\mathbf{v} - \mathbf{u}_\alpha) \otimes (\mathbf{v} - \mathbf{u}_\alpha) \rangle_\alpha$ is the pressure tensor. If there exist Lorentz force, then the term $\langle \mathbf{F}_\alpha \rangle_\alpha$ becomes

$$\langle \mathbf{F}_\alpha \rangle_\alpha = q_\alpha (\mathbf{E} + \mathbf{u}_\alpha \times \mathbf{B}), \quad (1.3.14)$$

where \mathbf{E} is electric field and \mathbf{B} is magnetic field. In the case of collisionless plasma, the

conservation equations for each species α reduces to

$$\frac{\partial \rho_\alpha}{\partial t} + \nabla \cdot (\rho_\alpha \mathbf{u}_\alpha) = 0, \quad (1.3.15)$$

$$\rho_\alpha \left[\frac{\partial \mathbf{u}_\alpha}{\partial t} + (\mathbf{u}_\alpha \cdot \nabla) \mathbf{u}_\alpha \right] = n_\alpha q_\alpha (\mathbf{E} + \mathbf{u}_\alpha \times \mathbf{B}) - \nabla \cdot (\mathbf{P}_\alpha), \quad (1.3.16)$$

$$\frac{\partial \epsilon_\alpha}{\partial t} + \nabla \cdot (\epsilon_\alpha \mathbf{u}_\alpha) + \nabla \cdot (\mathbf{P}_\alpha \cdot \mathbf{u}_\alpha) - n_\alpha q_\alpha \mathbf{u}_\alpha \cdot \mathbf{E} = 0. \quad (1.3.17)$$

What we come up with is a fluid model that treats each species (ions and electrons) in a plasma as a different fluid, [12]. Therefore we end up with a model for two species so called two fluid model where each individual plasma species lead to a different system of transport equations. However, there is a simpler description of plasma dynamics as the evolution of one single fluid, where the plasma is considered a conducting fluid. It is a system of transport equations which treats a plasma as a whole by combining each species variables. In other words, the quantities that are relative to each species, we can actually deduce to the one-fluid quantities that are evolved by the single-fluid model. For example, some of the unknown variables such as the mass density $\rho(t, x)$, the momentum density $\rho \mathbf{u}(t, x)$, and the electric current density \mathbf{J} are given, respectively, by the sum of the electron contribution and the ion contribution as follows

$$\rho(t, x) = \sum_\alpha n_\alpha m_\alpha, \quad (1.3.18)$$

$$\rho \mathbf{u}(t, x) = \sum_\alpha n_\alpha m_\alpha \mathbf{u}_\alpha, \quad (1.3.19)$$

$$\mathbf{J} = \sum_\alpha n_\alpha q_\alpha \mathbf{u}_\alpha. \quad (1.3.20)$$

Then the conservation equations for the plasma as a whole can be given as

$$\frac{\partial \rho}{\partial t} + \nabla \cdot (\rho \mathbf{u}) = 0, \quad (1.3.21)$$

$$\rho \left[\frac{\partial \mathbf{u}}{\partial t} + (\mathbf{u} \cdot \nabla) \mathbf{u} \right] = \rho_c \mathbf{E} + \mathbf{J} \times \mathbf{B} - \nabla \cdot (\mathbf{P}_\alpha), \quad (1.3.22)$$

$$\frac{\partial \epsilon}{\partial t} + \nabla \cdot (\epsilon \mathbf{u}) + \nabla \cdot (\mathbf{P} \cdot \mathbf{u}) - \rho_c \mathbf{u} \cdot \mathbf{E} = 0, \quad (1.3.23)$$

where ρ_c is charge density so that $\rho_c = \sum n_\alpha q_\alpha$.

Furthermore, for the type of collisionless case of the transport equations with a closure condition on the pressure tensor \mathbf{P}_α and some additional assumptions, the system leads to the three conservation laws, which become the Magnetohydrodynamics (MHD) model, when an additional approximation is introduced for \mathbf{E} . The fourth equation of the MHD system is the magnetic field equation comes from the "modified" Maxwell equations,

$$\nabla \times \mathbf{E} = -\frac{\partial \mathbf{B}}{\partial t}, \quad (1.3.24)$$

$$\nabla \cdot \mathbf{B} = 0, \quad (1.3.25)$$

$$\nabla \times \mathbf{H} = \mathbf{J}, \quad (1.3.26)$$

$$\nabla \times \mathbf{D} = 0, \quad (1.3.27)$$

where $\mathbf{B} = \mu_0 \mathbf{H}$, $\mathbf{D} = \epsilon_0 \mathbf{E}$ and the electric field \mathbf{E} is obtained by the Ohm's law, [12, 60].

The generalized Ohm's law is

$$\mathbf{E} + \frac{\mathbf{u} \times \mathbf{B}}{c} = \eta \mathbf{J} + \frac{\mathbf{J} \times \mathbf{B}}{en_e c} - \frac{\nabla \cdot \mathbf{P}_e}{n_e e c} + \frac{m_e}{n_e e^2} \frac{d\mathbf{J}}{dt}. \quad (1.3.28)$$

There are multiple versions of the MHD models. Depending on which term we keep at the right hand side of the generalized Ohm's law, we end up with a specific MHD model. For example, keeping the all terms at the right hand side as zero is called the ideal Ohm's law

$$\mathbf{E} + \mathbf{u} \times \mathbf{B} = 0, \quad (1.3.29)$$

and the resulting system becomes the ideal MHD model by decoupling the system with Maxwell's equations by doing the following assumptions

$$\text{the current density: } \quad \mathbf{J} = e(n_i \mathbf{u}_i - n_e \mathbf{u}_e),$$

where $n_i = n_e = n$ since the plasma assumed to be quasi-neutral because of Gauss's law,

$$\text{the charge density: } \quad \rho_c = e(n_i - n_e) = 0.$$

So, the charge density is ignored by the MHD formulation. Also, another assumption is to neglect the electromagnetic waves which in practice means neglecting the displacement current $\epsilon_0 \frac{\partial \mathbf{E}}{\partial t}$ in the Maxwell's equations.

Moreover, keeping just the $\eta \mathbf{J}$ term in the Ohm's law gives the resistive MHD. Ohm's law then becomes

$$\mathbf{J} = \sigma(\mathbf{E} + \mathbf{u} \times \mathbf{B}). \quad (1.3.30)$$

Using this ohm's law in the Faraday's equation (1.3.29) to eliminate \mathbf{E}

$$\nabla \times \left(\frac{\mathbf{J}}{\sigma} - \mathbf{u} \times \mathbf{B} \right) = -\frac{\partial \mathbf{B}}{\partial t}. \quad (1.3.31)$$

Then using $\nabla \times \mathbf{H} = \mathbf{J}$ and $\mathbf{B} = \mu_0 \mathbf{H}$ relations, we get

$$\nabla \times \left(\frac{\nabla \times \mathbf{B}}{\mu_0 \sigma} \right) - \nabla \times (\mathbf{u} \times \mathbf{B}) = -\frac{\partial \mathbf{B}}{\partial t}. \quad (1.3.32)$$

Then applying the vector identity $\nabla \times (\nabla \times \mathbf{B}) = -\nabla^2 \mathbf{B} + \nabla(\nabla \cdot \mathbf{B})$ and $\nabla \cdot \mathbf{B} = 0$, we obtain the magnetic field evolution equation

$$\frac{\partial \mathbf{B}}{\partial t} = \frac{1}{\mu_0 \sigma} \nabla^2 \mathbf{B} + \nabla \times (\mathbf{u} \times \mathbf{B}), \quad (1.3.33)$$

where σ is conductivity and $\frac{1}{\mu_0 \sigma}$ is the magnetic viscosity. Also, $\frac{1}{\mu_0 \sigma} \nabla^2 \mathbf{B}$ describes the effects of diffusion in the resistive MHD model.

Another MHD model is the Hall MHD model, which is derived by keeping $\eta \mathbf{J} + \frac{\mathbf{J} \times \mathbf{B}}{enec}$ terms in the Ohm's law. In this work, our focus is on both the ideal MHD model and the resistive MHD model and we intend to work on the Hall MHD system in the future. For more details, see [12, 60].

1.4 Review of Previous Work

1.4.1 Numerical Methods for Hyperbolic Conservation Laws

As stated, the ideal and resistive MHD models are mathematically hyperbolic conservation laws. This is the base system of the MHD model before applying the constrained transport correction methodology. There have been many numerical methods applied to MHD system to solve it in the literature. For example, the discontinuous Galerkin method [30], the finite volume / finite difference essentially non-oscillatory (ENO) methods [41, 68, 69], and finite

volume / finite difference Weighted essentially non-oscillatory (WENO) methods [45, 53]. The WENO schemes are the most robust and efficient schemes for the problems that contains discontinuities comparing to other methods. Thus, we use the WENO scheme in this thesis as a base-scheme for the ideal and resistive MHD equations. In section (2.2), we will provide the WENO scheme described for Hyperbolic Conservation Laws [48], which we will refer to this method as the WENO-HCL scheme.

For the conservation laws type equations, the non-oscillatory property is required for the time discretization. Therefore, We use strong stability preserving (SSP) Runge Kutta methods for temporal evolution. In particular, we use the optimal third order SSP-RK scheme (SSP-RK3) in our works which can be given by [68]. For the following equation

$$\partial_t q = L(q), \tag{1.4.1}$$

the SSP-RK3 can be expressed as

$$\begin{aligned} q^{(1)} &= q^n + \Delta t L(q^n), \\ q^{(2)} &= \frac{3}{4}q^n + \frac{1}{4}q^{(1)} + \frac{1}{4}\Delta t L(q^{(1)}), \\ q^{n+1} &= \frac{1}{3}q^n + \frac{2}{3}q^{(2)} + \frac{2}{3}\Delta t L(q^{(2)}), \end{aligned} \tag{1.4.2}$$

where Δt denotes time step and the supper scripts mean stage of SSP-RK.

1.4.2 Numerical Methods for ideal MHD

The ideal Magnetohydrodynamics (MHD) equations are one of the most important classical models of plasma physics explaining the macroscopic phenomena of a quasi-neutral plasma system. The ideal MHD equations are the set of transport evolution equations for

the quantities of mass, momentum, and energy density as well as the magnetic field in a conducting fluid. Mathematically, the MHD equations are a system of nonlinear hyperbolic conservation laws with divergence-free magnetic field condition. Satisfying this condition in numerical simulations is the main challenge for the numerical methods. Many standard schemes fail to guarantee $\nabla \cdot \mathbf{B} = 0$. There have been overall four different dominant approaches overcoming the difficult in the literature: 8-wave formulation [61, 62]; projection methods [4, 71]; hyperbolic divergence cleaning methods [33]; and constrained transport methods [2, 8, 31, 37, 38, 42, 54, 55, 64, 65, 32, 71, 70, 29].

The first methodology used for divergence free condition is developed in [14] utilizing the classical projection method. They solve a Poisson equation to project the incorrect magnetic field to a divergence free subspace using the Hodge decomposition. However, it is difficult to extend the method to an Adaptive Mesh Refinement (AMR) approach, since this method has to solve a Poisson equation on each time step. The AMR idea is to refine the mesh based on an accuracy criterion, providing increased resolution at shock and increased computational efficiency. Zachary [79] presented a Riemann solver which removes negative pressures and densities and used the Projection method to get a divergence free magnetic field. The 8-wave scheme is the second approach, developed by Powell in [61]. He adds an extra source term to update the magnetic field which satisfies the divergence free condition. By this treatment, the ideal MHD equations, with constraint, becomes a 8×8 hyperbolic system with a source term. This scheme is robust and can easily be extended to an AMR framework. However, it has been shown in [71] that this method can create inaccurate jumps in a discontinuous example, such as rotated shock tube problem, since this procedure is non-conservative because of the source term. The third method introduced by Dedner [33] is the hyperbolic divergence-cleaning method. This method is a similar to the projection

method. In this method, hyperbolic and parabolic corrections are combined together and solved for the magnetic field divergence error. This method is fully explicit, efficient and fast. However, this method has two tunable parameters, the speed of propagation of the error and the damped divergence error rate, which needed to be adjusted to ensure good solutions. This method gives a damped hyperbolic equation for the divergence error and it does not exactly satisfy divergence free condition.

The main focus in this work is the constrained transport (CT) method for correcting the magnetic field to satisfy the divergence free constraint. This methodology was invented by Evans and Hawley in [37]. The original CT method is considered to be a modification of the Yee method [78] from electromagnetics for the ideal MHD equations. In the original constrained transport methodology, staggered electric and magnetic fields are used to create appropriate finite difference operators. These operators eventually lead to a globally divergence-free magnetic field.

In the literature, various modification of the constrained transport method have been presented. In particular, high resolution shock capturing schemes have been a primary focus. DeVore [34] presented an application of a flux corrected transport approach satisfying a divergence free magnetic field. There are a range of different approaches for building the electric field using Ohm's law in a constrained transport methodology including those presented by Balsara and Spicer [8], Dai and Woodard [31], and Ryu et al. [65]. Londrillo and Zanna [54, 55] constructed one of the first high order upwind scheme based on the work of Evans and Hawley. De Sterck [32] introduced a similar constrained transport scheme on unstructured triangle grids based on multidimensional upwind advection schemes. Balsara [1] described a divergence free adaptive mesh refinement (AMR) method utilizing a constrained transport approach. Tóth [71] compared several of these schemes maintaining divergence free

condition and also showed a staggered magnetic field is unnecessary as well as developing some unstaggered CT frameworks.

Unstaggered Constrained Transport schemes are getting increased attention over the last few years, since it is easy to implement and to extend to adaptive mesh refinement (AMR) methods. For example, Fey and Torrilhon [38] developed an unstaggered upwind method satisfying the divergence free constraint. Rossmannith [64] designed an unstaggered wave propagation scheme for MHD flows based on the algorithms in [51] using a constrained transport method to keep the divergence free magnetic field. Helzel et al. [42, 43] generalized the 2D unstaggered CT work to 3D MHD equations so that the method is applicable on both Cartesian and rectangular mapped grids.

In recent years, several high order methods have been developed for the ideal MHD equations using various discretization approaches. Balsara [3] designed a third order divergence-free weighted essentially non-oscillatory (WENO) methods for MHD equations with third order Runge-Kutta time integration using a staggered magnetic field. Balsara et al. [5, 6] introduced a high accuracy ADER-WENO schemes for divergence free magnetohydrodynamics on structured meshes, again using a staggered magnetic field. Li et al. [52, 39] and Cheng et al. [20] presented high order central discontinuous Galerkin schemes satisfying the divergence free constraint globally for ideal MHD simulations on two overlapping meshes, called primal and dual meshes, by utilizing different discretization for magnetic induction equations. Kawai [49] introduced a divergence-free high order accurate finite difference scheme which has an effective shock capturing capability for the MHD equations by constructing artificial diffusion terms to capture numerical discontinuities in the magnetic field.

In our previous paper [29], we introduced a high order FD-WENO for the ideal MHD in 2D and 3D by developing a high order unstaggered constrained transport methodology for

Hamilton Jacobi equations using a version of FD-WENO. In that work, WENO formulation is applied to the central derivative of the solution \mathbf{A} instead of the flux values on grid points to approximate the one-sided partial derivative terms A_x^- and A_x^+ appear in HJ equation. If explicit time stepping is used for HJ equation, then it looks like a convection reaction equation and it tends to be unstable. That's why we needed to add artificial resistivity terms for the 3D case to stabilize it and to control unphysical oscillations in the magnetic field.

1.4.3 Method of Lines Transpose

In this current work, we further our work [29] on mesh aligned constrained transport by developing a new kernel-based approach for the magnetic vector potential to solve the ideal MHD equations in 2D and 3D. The approach is based on a kernel-based numerical scheme [22, 23], which is derived from the Method of Lines Transpose (MOL^T) [19, 16, 18, 17, 21, 15]. The equation is first discretized in time with an explicit method and transformed to a boundary value problem (BVP) at discrete time levels. The spatial operators are converted from local representations, i.e.. derivatives, to global representations using convolutions with kernels, i.e. Green's functions, and is similar in spirit of taking a Fast Fourier transform. Thus our method is fully implicit since the partial derivative terms are represented by global operators using convolution integrals which are communicating all the previous and future data. By this methodology, we update the predicted magnetic field obtained from the base scheme by a corrected divergence free magnetic field. The approach for solving the vector potential is derived from the method of lines transpose and is A-stable, eliminating the need of diffusion limiters introduced in our previous work in 3D [29] since the kernel based method is a fully implicit method. The corrected magnetic field is computed by 4th-order

accurate central finite difference operators that approximates the curl of the magnetic vector potential. The magnetic vector potential is made to satisfy a weakly hyperbolic system using the Weyl gauge condition. This system is solved using our kernel based scheme developed for Hamilton-Jacobi equations. Our solver is coupled with the 5th-order FD-WENO scheme of Jiang and Shu [47] as the base scheme for ideal MHD equations. Third order explicit strong-stability-preserving (SSP) Runge-Kutta (RK) is used for the time discretization. The work presented here is an improvement over the previous method in the context of problems with strong shocks due to the fact that, using the kernel-based approach, we could eliminate the diffusion limiter that was needed in our previous version of constrained transport. This method is robust and has been tested on the 2D and 3D cloud shock, blast wave and field loop problems.

1.4.4 Numerical Methods for non-ideal MHD

Magnetic reconnection is a significant phenomenon occurring in our solar system. When oppositely directed magnetic field lines in plasma come together, a strong current sheet is established. Even a small resistivity in this region becomes important, allowing plasma diffusion and thus, magnetic reconnection happens. In an ideal MHD model, there is a frozen-in flux condition, therefore there is no reconnection happening. However, Biskamp showed in his work [10] that for the resistive MHD model, the frozen-in constraint is broken in the dissipation region and reconnection occurs. The dissipation region establishes Sweet-Parker layer for a small resistivity value and the rate of reconnection is very low. In [50, 74], the inertia of electrons breaks the frozen-in constraint and the collision rate is very small in the magnetosphere. In the work about hybrid simulation with resistivity [57], in the work about two fluid simulations [56, 11] and in the work about the particle simulations [67, 44] it is

found that the rate of reconnection is insensitive to the strength of dissipation. Furthermore, the narrow current layers remain microscopic in length opposed to macroscopic Sweet-Parker current sheet. In [11], it is shown that the macroscopic current reappears, when the Hall term is removed from the simulations, thus the reconnection rate is decreased and it becomes sensitive to the electron inertia. Therefore, the Hall effect in the MHD model is an important term in determining collisionless magnetic reconnection rates. In [9] they investigated the magnetic reconnection in 2D in a simple Harris sheet configuration for resistive MHD and hall MHD. Our goal is to test our kernel based approximation on some magnetic reconnection benchmark problems.

Moreover, the choice of time stepping is also important for solving the non-ideal MHD equations, which have diffusion terms. For choice of explicit time stepping, there is very strict constraint for Δt due to the stability condition (i.e., $\Delta t \leq \frac{(\Delta x)^2}{2b}$), where b is the diffusivity parameter. This stability condition of explicit schemes gives the size of the time step and forces Δt to be very small, which leading to many time steps and taking quite computational time in the simulations. However, there are other ways of solving diffusion equations like using implicit solver for time stepping. Implicit schemes reduce the stability condition and allow larger time steps, but then there is a resulting a system of linear equations needed to be solved which may also take time. In the end, using implicit schemes may still save some computational time. In [72] Udrea develops an implicit algorithm for solution of the resistive MHD. The implicit formulation employed by their solver (WARP3) is a two level scheme and they use symmetric Gauss-Seidel method to solve the linear system resulting from the implicit scheme. Their solver addresses to solve steady state problems and their code also has an explicit mode capability. They tested that for time dependent simulations the implicit scheme in their solver WARP3 is faster than the explicit scheme. In a similar work, in [36]

Dubuc used a generalized conjugate gradient scheme to solve the linear system that results from the implicit discretization of the Euler equations. For the linear system resulting from the implicit discretization there are other direct methods (such as Gaussian elimination), which requires larger computer memory and thus not desired. Vanden and Whitfield [73] investigated the use of a direct method for a linear system that results from the discretization of Euler equations and they showed that their implementation of the direct method required approximately 3.5 more memory and 14.5 more CPU time than a Gauss-Seidel iterative scheme.

In this work, we choose explicit time stepping to solve resistive MHD and aim to develop an unconditionally stable kernel based approximation to solve Hamilton Jacobi equations with diffusion terms, which will allow us to take larger time steps. We will test our solver with our previous work [29], which is originally designed to solve ideal MHD. However, we will add second order approximation for diffusion terms in previous finite difference weighted essentially non-oscillatory (FD-WENO) solver.

Chapter 2

The Ideal MHD Equations

2.1 The Ideal MHD Equations

In this section we present a brief review of the ideal MHD equations, which is a first order hyperbolic system of conservation laws. The conservative form of the ideal MHD equations can be written as

$$\partial_t \begin{bmatrix} \rho \\ \rho \mathbf{u} \\ \mathcal{E} \\ \mathbf{B} \end{bmatrix} + \nabla \cdot \begin{bmatrix} \rho \mathbf{u} \\ \rho \mathbf{u} \otimes \mathbf{u} + p_{\text{tot}} \mathbb{I} - \mathbf{B} \otimes \mathbf{B} \\ \mathbf{u}(\mathcal{E} + p_{\text{tot}}) - \mathbf{B}(\mathbf{u} \cdot \mathbf{B}) \\ \mathbf{u} \otimes \mathbf{B} - \mathbf{B} \otimes \mathbf{u} \end{bmatrix} = 0, \quad (2.1.1)$$

$$\nabla \cdot \mathbf{B} = 0, \quad (2.1.2)$$

with the equation of state as

$$\mathcal{E} = \frac{p}{\gamma - 1} + \frac{\rho \|\mathbf{u}\|^2}{2} + \frac{\|\mathbf{B}\|^2}{2}. \quad (2.1.3)$$

where the total mass ρ , the momentum $\rho \mathbf{u} = (\rho u^1, \rho u^2, \rho u^3)^T$, the energy densities \mathcal{E} of the plasma system, and the magnetic field vector $\mathbf{B} = (B^1, B^2, B^3)^T$ are all conserved variables.

The velocity \mathbf{u} and the total pressure $p_{\text{tot}} = p + \frac{1}{2}\|\mathbf{B}\|^2$, together with the hydrodynamic

pressure, which is given by the ideal gas law as

$$p = (\gamma - 1)\left(\mathcal{E} - \frac{1}{2}\|\mathbf{B}\|^2 - \frac{1}{2}\rho\|\mathbf{u}\|^2\right), \quad (2.1.4)$$

are derived quantities. $\gamma = 5/3$ is the ideal gas constant and the notation $\|\cdot\|$ is used for the purpose of the Euclidean vector norm. The MHD equations (2.1.1)-(5.1.2) are derived and discussed in many standard plasma textbooks (e.g., [59]).

2.1.1 Hyperbolicity of the governing equations

The system (2.1.1) along with the equation of state (5.1) comprise a system of hyperbolic conservation laws

$$\mathbf{q}_t + \nabla \cdot \mathbf{F}(\mathbf{q}) = 0. \quad (2.1.5)$$

This set of equations describes the time evolution of all eight conserved variables, $\mathbf{q} = (\rho, \rho\mathbf{u}, \mathcal{E}, \mathbf{B})$. We will denote the Jacobian of the hyperbolic system as $M(\mathbf{q}) = \partial\mathbf{F}/\partial\mathbf{q}$, which is a diagonalizable matrix with real eigenvalues. The eigenvalues of the Jacobian matrix represent the wave speeds of the eight waves in MHD system. In particular, in some arbitrary direction \mathbf{n} ($\|\mathbf{n}\| = 1$), they can be written as

$$\lambda^{1,8} = \mathbf{u} \cdot \mathbf{n} \mp c_f \quad \text{fast magnetosonic waves,} \quad (2.1.6a)$$

$$\lambda^{2,7} = \mathbf{u} \cdot \mathbf{n} \mp c_a \quad \text{Alvén waves,} \quad (2.1.6b)$$

$$\lambda^{3,6} = \mathbf{u} \cdot \mathbf{n} \mp c_s \quad \text{slow magnetosonic waves,} \quad (2.1.6c)$$

$$\lambda^4 = \mathbf{u} \cdot \mathbf{n} \quad \text{entropy waves,} \quad (2.1.6d)$$

$$\lambda^5 = \mathbf{u} \cdot \mathbf{n} \quad \text{divergence waves,} \quad (2.1.6e)$$

where

$$a \equiv \sqrt{\frac{\gamma p}{\rho}} \quad (2.1.7a)$$

$$c_a \equiv \sqrt{\frac{(\mathbf{B} \cdot \mathbf{n})^2}{\rho}} \quad (2.1.7b)$$

$$c_f \equiv \left\{ \frac{1}{2} \left[a^2 + \frac{\|\mathbf{B}\|^2}{\rho} + \sqrt{\left(a^2 + \frac{\|\mathbf{B}\|^2}{\rho} \right)^2 - 4a^2 \frac{(\mathbf{B} \cdot \mathbf{n})^2}{\rho}} \right] \right\}^{1/2} \quad (2.1.7c)$$

$$c_s \equiv \left\{ \frac{1}{2} \left[a^2 + \frac{\|\mathbf{B}\|^2}{\rho} - \sqrt{\left(a^2 + \frac{\|\mathbf{B}\|^2}{\rho} \right)^2 - 4a^2 \frac{(\mathbf{B} \cdot \mathbf{n})^2}{\rho}} \right] \right\}^{1/2} \quad (2.1.7d)$$

The eight eigenvalues are well ordered as

$$\lambda^1 \leq \lambda^2 \leq \lambda^3 \leq \lambda^4 \leq \lambda^5 \leq \lambda^6 \leq \lambda^7 \leq \lambda^8 \quad (2.1.8)$$

where the fast and slow magnetosonic waves are nonlinear while the rest of the waves are linearly degenerate.

2.2 Overview of the Base Scheme WENO-HCL

Assuming that \mathbf{B} is always divergence free, we can simply apply the standard WENO methodology. Here we review this methodology before talking about of form of constrained transport. We present the 5th-order Weighted Essentially Non-Oscillatory method developed for Hyperbolic Conservation Laws (WENO-HCL) [48] for the MHD system that comprises the base scheme in the CT procedure. WENO-HCL method is described by Jiang and Wu

in [48]. We will briefly explain the scheme for a one dimensional MHD model

$$\frac{\partial q}{\partial t} + \frac{\partial \mathbf{f}(q)}{\partial x} = 0 \quad (2.2.1)$$

where

$$q = (\rho, \rho u^1, \rho u^2, \rho u^3, \mathcal{E}, B^1, B^2, B^3)^T, \quad (2.2.2)$$

$$\mathbf{f}(q) = \left(\rho u^1, \rho u^1 u^1 + p + \frac{1}{2} \|\mathbf{B}\|^2 - B^1 B^1, \rho u^1 u^2 - B^1 B^2, \rho u^1 u^3 - B^1 B^3, \right. \quad (2.2.3)$$

$$\left. u^1 (\mathcal{E} + p + \frac{1}{2} \|\mathbf{B}\|^2) - B^1 (\mathbf{u} \cdot \mathbf{B}), 0, u^1 B^2 - u^2 B^1, u^1 B^3 - u^3 B^1 \right)^T$$

Also, we denote the primitive variables as

$$w = (\rho, u^1, u^2, u^3, p, B^1, B^2, B^3)^T \quad (2.2.4)$$

The Jacobian of the flux $\frac{\partial \mathbf{f}}{\partial q}$ of the above equation can be decomposed based on eigenvectors since the MHD system is hyperbolic

$$\frac{\partial \mathbf{f}}{\partial q} = \mathbf{R} \mathbf{\Lambda} \mathbf{L} \quad (2.2.5)$$

where $\mathbf{\Lambda}$ is the diagonal matrix of real eigenvalues, \mathbf{R} is the right eigenvectors, and $\mathbf{L} = \mathbf{R}^{-1}$ is the left eigenvectors.

We discretize the space into uniform intervals with Δx size. Denoting $q_i(t)$ as the numerical solution of the MHD model at the point $x = x_i$, the WENO-HCL method for the

MHD system in the conservative form

$$\frac{dq_i(t)}{dt} = \frac{1}{\Delta x} \left(\hat{\mathbf{F}}_{i+\frac{1}{2}} - \hat{\mathbf{F}}_{i-\frac{1}{2}} \right) \quad (2.2.6)$$

The following WENO procedure is applied to get the numerical flux $\hat{\mathbf{F}}_{i+\frac{1}{2}}$ for the above semi discrete form:

1. Compute the physical flux and the solution q_i for all i

$$\mathbf{f}_i = \mathbf{f}(q_i). \quad (2.2.7)$$

2. Do the following steps at each fixed $x_{i+\frac{1}{2}}$

- (a) Compute the average state $w_{i+\frac{1}{2}}$ using Roe average

$$w_{i+\frac{1}{2}} = \frac{1}{2}(w_i + w_{i+1}) \quad (2.2.8)$$

- (b) Compute the eigenvalues $\Lambda_{i+\frac{1}{2}}$ of the Jacobian of flux, $\frac{\partial \mathbf{f}}{\partial q}$, at the point $x_{i+\frac{1}{2}}$.

Also, compute the right eigenvector $\mathbf{R}_{i+\frac{1}{2}}$ and left eigenvector $\mathbf{L}_{i+\frac{1}{2}}$

$$\Lambda_{i+\frac{1}{2}} = \Lambda\left(w_{i+\frac{1}{2}}\right), \quad \mathbf{R}_{i+\frac{1}{2}} = \mathbf{R}\left(w_{i+\frac{1}{2}}\right), \quad \mathbf{L}_{i+\frac{1}{2}} = \mathbf{L}\left(w_{i+\frac{1}{2}}\right). \quad (2.2.9)$$

- (c) Project the solution and the physical flux to local characteristic field (right eigenvector space)

$$\mathbf{V}_j = \mathbf{L}_{i+\frac{1}{2}} q_j \quad \text{and} \quad \mathbf{G}_j = \mathbf{L}_{i+\frac{1}{2}} \mathbf{f}_j \quad (2.2.10)$$

where $j = i - 2, i - 1, i, i + 1, i + 2, i + 3$ for the 5th-order WENO.

- (d) Perform the Lax Friedrichs flux splitting procedure for the each component of the characteristic variables, to obtain the corresponding component of the \mathbf{V}_j and \mathbf{G}_j . We can assume the m-th component of the characteristic variables of the \mathbf{V}_j and \mathbf{G}_j as v_j and g_j , respectively and compute

$$g_j^\pm = \frac{1}{2}(g_j \pm \alpha^{(m)}v_j), \quad (2.2.11)$$

where the maximum wave speed of the m-th component of characteristic variables is

$$\alpha^{(m)} = \max_k |\lambda^{(m)}(q_k)| \quad (2.2.12)$$

- (e) Compute the numerical flux by applying a WENO reconstruction on the computed flux components g_j^\pm . Let's WENO5 denotes the 5-th order WENO reconstruction, then the numerical flux is obtained as

$$\hat{g}_{i+\frac{1}{2}}^+ = WENO5\left(g_{i-2}^+, g_{i-1}^+, g_i^+, g_{i+1}^+, g_{i+2}^+\right), \quad (2.2.13)$$

$$\hat{g}_{i+\frac{1}{2}}^- = WENO5\left(g_{i+3}^-, g_{i+2}^-, g_{i+1}^-, g_i^-, g_{i-1}^-\right). \quad (2.2.14)$$

Then we compute the m-th component of the numerical flux $\hat{\mathbf{G}}_{i+\frac{1}{2}}$ as

$$\hat{g}_{i+\frac{1}{2}} = \hat{g}_{i+\frac{1}{2}}^+ + \hat{g}_{i+\frac{1}{2}}^- \quad (2.2.15)$$

- (f) Project the numerical flux back into physical space

$$\hat{\mathbf{F}}_{i+\frac{1}{2}} = \hat{\mathbf{R}}_{i+\frac{1}{2}} \hat{\mathbf{G}}_{i+\frac{1}{2}} \quad (2.2.16)$$

The scheme described above is the WENO-HCL scheme that serves as the base scheme in our Constrained Transport framework. Also, the high order SSP-RK methods are used for the time discretization for the MHD model.

As mentioned earlier, the direct application of the WENO-HCL scheme to the MHD model leads to divergence error in the magnetic field, and we update the magnetic field solution through magnetic potential equation by the CT method. In the next section, we will derive the magnetic potential equation from the magnetic field equation for the ideal MHD model.

2.3 Magnetic potential in 3D

There have been many numerical methods presented in the literature for numerically solving the MHD system, but they have faced the main challenge of satisfying the divergence free condition on the magnetic field. Here, we will derive the magnetic vector potential equation from the magnetic field equation given in (2.1.1)-(5.1.2) system. This will serve as the foundation of our constrained transport framework.

Since the magnetic field is divergence free, it can always be written as the curl of a magnetic vector potential

$$\mathbf{B} = \nabla \times \mathbf{A}. \tag{2.3.1}$$

We show in the section (3.2) that if we construct the curl using 4th order central differences, we locally preserve the divergence free property. The key step of the constrained transport scheme is to solve the magnetic potential for correcting the magnetic field. The evolution of

the magnetic field in (2.1.1) can be written in the following form

$$\mathbf{B}_t + \nabla \times (\mathbf{B} \times \mathbf{u}) = 0, \quad (2.3.2)$$

using the relation

$$\nabla \cdot (\mathbf{u} \otimes \mathbf{B} - \mathbf{B} \otimes \mathbf{u}) = \nabla \times (\mathbf{B} \times \mathbf{u}).$$

Since \mathbf{B} is divergence free, we set $\mathbf{B} = \nabla \times \mathbf{A}$ and rewrite the evolution equation (2.3.2) as

$$\nabla \times \{\mathbf{A}_t + (\nabla \times \mathbf{A}) \times \mathbf{u}\} = 0.$$

This implies that there exists a scalar function ψ such that

$$\mathbf{A}_t + (\nabla \times \mathbf{A}) \times \mathbf{u} = -\nabla\psi.$$

There are various choices of the gauge conditions depending on how we chose the ψ . Helzel et al. [42] showed that using the Weyl gauge, i.e., setting $\psi \equiv 0$, one can achieve stable solutions. This condition results in the evolution equation for the magnetic vector potential as

$$\partial_t \mathbf{A} + (\nabla \times \mathbf{A}) \times \mathbf{u} = 0, \quad (2.3.3)$$

which can be written as:

$$\partial_t \mathbf{A} + N_1 \mathbf{A}_x + N_2 \mathbf{A}_y + N_3 \mathbf{A}_z = 0, \quad (2.3.4)$$

with

$$N_1 = \begin{bmatrix} 0 & -u^2 & -u^3 \\ 0 & u^1 & 0 \\ 0 & 0 & u^1 \end{bmatrix}, \quad N_2 = \begin{bmatrix} u^2 & 0 & 0 \\ -u^1 & 0 & -u^3 \\ 0 & 0 & u^2 \end{bmatrix}, \quad N_3 = \begin{bmatrix} u^3 & 0 & 0 \\ 0 & u^3 & 0 \\ -u^1 & -u^2 & 0 \end{bmatrix}.$$

The resulting system is only weakly hyperbolic since the matrix of right eigenvectors of the flux Jacobian doesn't have full rank in certain directions. We begin with the flux Jacobian matrix in some arbitrary direction $\mathbf{n} = (n^1, n^2, n^3)$ to show the weakly hyperbolicity:

$$M(\mathbf{n}, \mathbf{u}) := n^1 N_1 + n^2 N_2 + n^3 N_3 = \begin{bmatrix} n^2 u^2 + n^3 u^3 & -n^1 u^2 & -n^1 u^3 \\ -n^2 u^1 & n^1 u^1 + n^3 u^3 & -n^2 u^3 \\ -n^3 u^1 & -n^3 u^2 & n^1 u^1 + n^2 u^2 \end{bmatrix}, \quad (2.3.5)$$

which has real eigenvalues for all $\|\mathbf{n}\| = 1$ as

$$\lambda^1 = 0, \quad \lambda^2 = \lambda^3 = \mathbf{n} \cdot \mathbf{u}, \quad (2.3.6)$$

and the right eigenvectors matrix is

$$R = \left[r^{(1)} \middle| r^{(2)} \middle| r^{(3)} \right] = \begin{bmatrix} n^1 & n^2 u^3 - n^3 u^2 & u^1 (\mathbf{u} \cdot \mathbf{n}) - n^1 \|\mathbf{n}\|^2 \\ n^2 & n^3 u^1 - n^1 u^3 & u^2 (\mathbf{u} \cdot \mathbf{n}) - n^2 \|\mathbf{n}\|^2 \\ n^3 & n^1 u^2 - n^2 u^1 & u^3 (\mathbf{u} \cdot \mathbf{n}) - n^3 \|\mathbf{n}\|^2 \end{bmatrix}. \quad (2.3.7)$$

If we assume that $\|\mathbf{u}\| \neq 0$ and $\|\mathbf{n}\| = 1$, then the determinant of the matrix of the right

eigenvector R can be found as

$$\det(R) = -\|\mathbf{u}\|^3 \cos(\alpha) \sin^2(\alpha)$$

where α is the angle between the vectors \mathbf{n} and \mathbf{u} . Hence, given any nonzero velocity vector \mathbf{u} , there exist four degenerate directions $\alpha = 0, \pi/2, \pi, 3\pi/2$, where the eigenvectors are incomplete due to $\det(R) = 0$. Therefore, the system (2.3.4) is only weak hyperbolic.

2.3.1 Magnetic potential in 2D

In the two dimensional case (e.g., in the xy-plane), each conserved variable, $\mathbf{q} = (\rho, \rho\mathbf{u}, \mathcal{E}, \mathbf{B})$, depends only on t, x , and y independent variables. Thus, the divergence free condition can be simplified as

$$\nabla \cdot \mathbf{B} = B_x^1 + B_y^2.$$

There is no point to define B^3 since any value of B^3 satisfies the divergence free condition in 2D. The evolution of the magnetic field involves only the third component of the magnetic vector potential, so that magnetic field components, B^1 and B^2 , can be found as

$$B^1 = A_y^3 \quad \text{and} \quad B^2 = -A_x^3. \quad (2.3.8)$$

Since we only need the third component of the magnetic vector potential to define magnetic field, the constrained transport scheme in 2D is reduced to the magnetic vector potential to a magnetic scalar potential equation as

$$A_t^3 + u^1 A_x^3 + u^2 A_y^3 = 0 \quad (2.3.9)$$

This scalar advection equation is strongly hyperbolic by contrast with the 3D case.

2.4 The advantage of MOLT based current method over WENO-HJ method

As we will explain in the next chapter about the Constrained Transport Methodology, the magnetic vector field is updated so that it satisfies the divergence free condition by solving the magnetic vector potential equations (2.3.9) in 2D and (2.3.4) in 3D. Although the CT method that we use is the same idea that we used in our previous work [29], in this section we will explain the challenges of the previous work and present the advantages of the current work.

The magnetic potential equation is a Hamilton-Jacobi equation since the components of the velocity are given from the previous time step such that

$$A_t^3 + H(x, y, A_x^3 + u^2 A_y^3) = 0 \quad (2.4.1)$$

with Hamiltonian

$$H(x, y, A_x^3 + u^2 A_y^3) = u^1 A_x^3 + u^2 A_y^3 \quad (2.4.2)$$

In the previous work [29], the WENO-HJ scheme is directly applied to two-dimensional magnetic scalar potential equation (2.3.9). However, the scheme cannot be directly applied to the three-dimensional magnetic vector potential equation due the problem being weakly hyperbolic of the 3D system (2.3.4). Because of the problem is weakly hyperbolic, we applied a finite difference weighted essentially non-oscillatory (WENO-FD) discretization using

arithmetic averages to define derivatives at grid points in the old work [29]. But this type of discretization approach leads a lack of insufficient numerical resistivity in order to control unphysical oscillations in the 3D magnetic field equation. Therefore, artificial resistivity terms into the magnetic vector potential equation were introduced for solving 3D system. For brevity, we give only the equation of the first component of the magnetic vector potential system with artificial resistivity term:

$$A_t^1 - u^2 A_x^2 - u^3 A_x^3 + u^2 A_y^1 + u^3 A_z^1 = \varepsilon^1 \frac{\partial^2 A^1}{\partial x^2} \quad (2.4.3)$$

The above equation is the equation of the first component of magnetic vector potential A^1 , but this equation also contains other two components A^2 and A^3 . With explicit time stepping, it tends to be unstable. Therefore, we added the the term that is on the right hand side of the (2.4.3) to stabilize the equation. The additional term on the right hand side of the equation (2.4.3) is an artificial resistivity in the missing direction, which in the above equation for A^x , it has an artificial resistivity term in the x -direction. The artificial resistivity is defined as

$$\varepsilon^1 = 2\nu\gamma^1 \frac{\Delta x^2}{\delta + \Delta t}, \quad (2.4.4)$$

where δ is a very small parameter to ensure that ε^1 remains bounded as $\Delta t \rightarrow 0^+$, γ^1 is the smoothness indicator of A^x , and ν is a constant to control the magnitude of the artificial resistivity. Note that the limiter is off in smooth regions.

In the current work, we will circumvent the stabilization challenges by introducing a new $\mathcal{O}(N)$ implicit method that solves magnetic potential equation with an unconditionally stable solver using the Method of Lines Transpose idea. We no longer need artificial resistivity terms for solving the magnetic vector potential equations in this novel method. The rest of the

scheme is still using the same WENO architecture that we've used in the previous work. We are targeting a better solver that handle things like strong shocks since we do not need to introduce a limiter for A. We will show the examples of this in the results section.

In the next section we will present the overview of the Method of Lines Transpose which have been presented in the previous work [23].

2.5 Outline of the constrained transport methodology

The major challenge when dealing with the numerical solution of the system (2.1.1)-(5.1) is to satisfy the divergence-free condition (5.1.2). The constrained transport methodology is one of the dominant approach in the literature to overcome this challenge. In this section we will give the main idea of this method and our perspective how we are using high order CT framework. The idea of the constrained transport methodology is based on updating the conserved variables $\mathbf{q} = (\rho, \rho\mathbf{u}, \mathcal{E}, \mathbf{B})$. One of the early works on this idea of using the magnetic vector potential equations for CT solution to the MHD equations is presented by Wilson in [75], as well as Dorfi [35]. However, modern shock capturing strategies were not used in those works and hence caused strong numerical diffusion. Londrillo and Del Zanna [54] used the magnetic potential solutions in the context of shock capturing methods, along with De Sterck [32], Londrillo and Del Zanna [55], and Rossmannith [64]. Helzet et al. [43] developed a framework for unstaggered CT scheme coupling a conservative finite volume hyperbolic scheme for the MHD equations with a non conservative finite volume scheme for the magnetic vector potential equation. In our previous work [29], we developed a high order finite difference constrained transport scheme. In this paper, we present a kernel based high order unconditionally stable CT method. We correct the conserved variables, \mathbf{q} , using the

magnetic vector potential formulation with respect to relation $\mathbf{B} = \nabla \times \mathbf{A}$. Here, we give an outline of the general unstaggered CT framework listing all important steps. Consider a semi discrete system of ordinary differential equations for MHD equations (2.1.1)

$$\mathbf{q}'_{mhd}(t) = \mathcal{L}(\mathbf{q}_{mhd}(t)) \quad (2.5.1)$$

where $\mathbf{q}_{mhd}(t)$ represents the grid function at time t consisting of all point-wise values of the conserved quantities in the ideal MHD system $\mathbf{q}_{mhd} = (\rho, \rho\mathbf{u}, \mathcal{E}, \mathbf{B})$. The details about $\mathcal{L}(\mathbf{q}_{mhd}(t))$ were presented in [29].

And also consider the update for the magnetic potential equation ((2.3.9) for 2D case and (2.3.4) for 3D case) on the mesh,

$$\mathbf{q}'_A(t) = \mathcal{H}(\mathbf{q}_A(t), \mathbf{u}(t)), \quad (2.5.2)$$

where \mathbf{q}_A denotes vector potential \mathbf{A} in 3D or the scalar potential A^3 in 2D.

The key steps advancing the solution from its current time step $t = t^n$ (or the initial condition at t^0) to its new time step t^{n+1} are listed below:

- step 0: Start with the given current time step $\mathbf{q}_{mhd}^n = (\rho^n, \rho\mathbf{u}^n, \mathcal{E}^n, \mathbf{B}^n)^T$ and \mathbf{q}_A^n .
- step 1: Obtain \mathbf{q}_{mhd}^* and \mathbf{q}_A^{n+1} separately, where

$$\mathbf{q}_{mhd}^* = (\rho^{n+1}, \rho^{n+1}\mathbf{u}^{n+1}, \mathcal{E}^*, \mathbf{B}^*).$$

Here, \mathcal{E}^* and \mathbf{B}^* are given with a * superscript instead of $n + 1$ to indicate that the predicted \mathbf{B} and \mathcal{E} will be corrected by a predictor-corrector Constrained Transpose

method before the end of the time step.

- step 2: Replace \mathbf{B}^* to \mathbf{B}^{n+1} by a discrete curl of \mathbf{q}_A^{n+1} .

$$\mathbf{B}^{n+1} = \nabla \times \mathbf{q}_A^{n+1}.$$

- step 3: Set the corrected total energy density value \mathcal{E}^{n+1} based on one of the following options:

Option 1: Keep the total energy conserved

$$\mathcal{E}^{n+1} = \mathcal{E}^*.$$

Option 2: Keep the pressure the same after updating the magnetic field

$$\mathcal{E}^{n+1} = \mathcal{E}^* + \frac{1}{2}(\|\mathbf{B}^{n+1}\|^2 - \|\mathbf{B}^*\|^2)$$

(Second option sometimes helps to prevent negative pressure).

In Section 3.2, we show that our approach leads to a divergence free solution. We now describe how we constraint the update for \mathbf{q}_A^{n+1} using our kernel based approach.

Chapter 3

Kernel Based Approximation with Constrained Transport for Ideal MHD

In this chapter we develop a kernel based approximation for magnetic scalar/vector potential equations, which are considered as Hamilton Jacobi equations since the velocity variables are given in the previous time step. We also present a WENO quadrature formulation to approximate the convolution integrals, which appears in our kernel based formulation. We will refer this new kernel based approximation coupled with WENO quadrature as MOLT-HJ scheme [23]. This proposed scheme is a key part of the constrained transport method used to update the solutions such that the magnetic field solution satisfies the divergence free condition. Our goal is to eliminate the need of artificial terms such as the diffusion limiter (introduced in the previous work [29]) and to understand what that means for strong shocks. We develop our solver for both 2D and 3D. We later include the artificial diffusion terms into the MOLT-HJ scheme in 3D to be able to compare the the new scheme with the old method. We demonstrate the robustness of the new method on several test problems in 2D and 3D and validate that the new method works well for the blast wave and strong shocks by comparing with the old method. Further, we validate the negative impact of the diffusion limiter by adding the artificial limiters to MOLT-HJ scheme. MOLT with diffusion limiter obtains very similar results with the previous method.

3.1 Hamilton-Jacobi equations

In this section we introduce the main ideas in our kernel-based method [22, 23], which is derived from the Method of Lines Transpose (MOL^T) [19, 16, 18, 17, 21, 15]. The simplest way to describe MOL^T is: we start by discretizing the problem in time; we then use a global approximation for the inherently local term (the derivative). By doing this, we are able to make an explicit approximation unconditionally stable. As for the global approximation, think FFT, but with a different convolution kernel. The form of the approximation is what facilitates the stability of the method. The method is an $\mathcal{O}(N)$ because the convolution with the kernels can be evaluated using a three term recursion.

3.1.1 1D Hamilton-Jacobi equations

We start with a 1D Hamilton-Jacobi equation

$$A_t + H(A_x) = 0, \quad A(x, 0) = A^0(x), \quad x \in [a, b], \quad (3.1.1)$$

where H is the Hamiltonian flux. For the time discretization purpose to evolve the solution from time t^n to t^{n+1} , we use the classical explicit SSP RK schemes [40]. In this work, we propose to use the following SSP RK schemes such as the first order forward Euler scheme

$$A^{n+1} = A^n - \Delta t \hat{H}(A_x^{n,-}, A_x^{n,+}); \quad (3.1.2)$$

the second order SSP RK scheme

$$A^{(1)} = A^n - \Delta t \hat{H}(A_x^{n,-}, A_x^{n,+}),$$

$$A^{n+1} = \frac{1}{2}A^n + \frac{1}{2} \left(A^{(1)} - \Delta t \hat{H}(A_x^{(1),-}, A_x^{(1),+}) \right); \quad (3.1.3)$$

and the third order SSP RK scheme

$$\begin{aligned} A^{(1)} &= u^n - \Delta t \hat{H}(A_x^{n,-}, A_x^{n,+}), \\ A^{(2)} &= \frac{3}{4}A^n + \frac{1}{4} \left(A^{(1)} - \Delta t \hat{H}(A_x^{(1),-}, A_x^{(1),+}) \right), \\ A^{n+1} &= \frac{1}{3}A^n + \frac{2}{3} \left(A^{(2)} - \Delta t \hat{H}(A_x^{(2),-}, A_x^{(2),+}) \right). \end{aligned} \quad (3.1.4)$$

Here, Δt denotes the time step and \hat{H} is the numerical Hamiltonian, e.g., the local Lax-Friedrichs Hamiltonian flux [46]:

$$\hat{H}(\phi^-, \phi^+) = H\left(\frac{\phi^- + \phi^+}{2}\right) - c(\phi^-, \phi^+) \frac{(\phi^+ - \phi^-)}{2}, \quad (3.1.5)$$

with $c(\phi^-, \phi^+) = \max_{\phi \in [\min(\phi^-, \phi^+), \max(\phi^-, \phi^+)]} |H'(\phi)|$. A_x^- and A_x^+ are one-side derivatives with *left*-biased and *right*-biased methods, respectively, to approximate A_x . Finding these derivatives has the dominant role in our work and we will present the details of the construction of them in the following subsection.

3.1.2 Approximation of the first order derivative ∂_x

Approximating the partial spatial derivative terms with kernel based scheme is the major part of this work. In this section we briefly review the construction of the ∂_x derivative approximation using kernel based formulation established in [22]. Let's define operators \mathcal{L}_L

and \mathcal{L}_R on the closed interval $[a, b]$, and their inverse operators

$$\mathcal{L}_L = \mathcal{I} + \frac{1}{\alpha} \partial_x \Rightarrow \mathcal{L}_L^{-1}[v, \alpha](x) = \alpha \int_a^x e^{-\alpha(x-y)} v(y) dy + A_L e^{-\alpha(x-a)}, \quad (3.1.6a)$$

$$\mathcal{L}_R = \mathcal{I} - \frac{1}{\alpha} \partial_x \Rightarrow \mathcal{L}_R^{-1}[v, \alpha](x) = \alpha \int_x^b e^{-\alpha(y-x)} v(y) dy + B_R e^{-\alpha(b-x)}, \quad (3.1.6b)$$

where \mathcal{I} is the identity operator and α is a positive constant. We use I^L and I^R to denote the convolution integral as

$$I^L = \alpha \int_a^x e^{-\alpha(x-y)} v(y) dy, \quad I^R = \alpha \int_x^b e^{-\alpha(y-x)} v(y) dy. \quad (3.1.7)$$

We can see that I^L depends on the function values of v from left end point a to x , as well as I^R is for right end point b to x . Also note that A_L and B_R are determined by the boundary conditions. For instance, if we assume periodic boundary conditions, i.e.,

$$\mathcal{L}_L^{-1}[v, \alpha](a) = \mathcal{L}_L^{-1}[v, \alpha](b), \quad \text{and,} \quad \mathcal{L}_R^{-1}[v, \alpha](a) = \mathcal{L}_R^{-1}[v, \alpha](b).$$

then we obtain

$$A_L = \frac{I^L[v, \alpha](b)}{1 - \mu}, \quad \text{and} \quad B_R = \frac{I^R[v, \alpha](a)}{1 - \mu}, \quad (3.1.8)$$

where $\mu = e^{-\alpha(b-a)}$. If we require

$$\mathcal{L}_L^{-1}[v, \alpha](a) = C_a, \quad \text{and} \quad \mathcal{L}_R^{-1}[v, \alpha](b) = C_b$$

with given numbers C_a and C_b , then, the boundary coefficients are obtained as

$$A_L = C_a, \quad \text{and} \quad B_R = C_b. \quad (3.1.9)$$

Now, let's define new operators \mathcal{D}_L and \mathcal{D}_R ,

$$\mathcal{D}_L = \mathcal{I} - \mathcal{L}_L^{-1}, \quad \text{and} \quad \mathcal{D}_R = \mathcal{I} - \mathcal{L}_R^{-1}.$$

Then $\frac{1}{\alpha}\partial_x$ can be represented using the infinite series of these operators as

$$\frac{1}{\alpha}\partial_x = \mathcal{L}_L - \mathcal{I} = \mathcal{L}_L(\mathcal{I} - \mathcal{L}_L^{-1}) = \mathcal{D}_L(\mathcal{I} - \mathcal{D}_L)^{-1} = \sum_{p=1}^{\infty} \mathcal{D}_L^p \quad (3.1.10a)$$

$$\frac{1}{\alpha}\partial_x = \mathcal{I} - \mathcal{L}_R = \mathcal{L}_R(\mathcal{L}_R^{-1} - \mathcal{I}) = -\mathcal{D}_R(\mathcal{I} - \mathcal{D}_R)^{-1} = -\sum_{p=1}^{\infty} \mathcal{D}_R^p \quad (3.1.10b)$$

where, \mathcal{D}^p is successively defined as $\mathcal{D}^p = \mathcal{D}[\mathcal{D}^{p-1}]$. In the kernel-based method, we will truncate the series (3.1.10) and only compute the corresponding partial sum to approximate the A_x^\pm in (3.1.2)-(3.1.4). Moreover, an additional term \mathcal{D}_0 is introduced for reasons related to stability of our high order method

$$\mathcal{D}_0[v, a] = v(a) - \frac{\alpha}{2} \int_a^b e^{-\alpha|x-y|} v(y) dy - A_0 e^{-\alpha(x-a)} - B_0 e^{-\alpha(b-x)}, \quad (3.1.11)$$

where A_0 and B_0 are determined by boundary conditions. For example, if \mathcal{D}_0 is a periodic function such that

$$\mathcal{D}_0[v, \alpha](a) = \mathcal{D}_0[v, \alpha](b), \quad \text{and} \quad \partial_x \mathcal{D}_0[v, \alpha](a) = \partial_x \mathcal{D}_0[v, \alpha](b),$$

then we get

$$A_0 = \frac{I^0[v, \alpha](b)}{1 - \mu}, \quad B_0 = \frac{I_0[v, \alpha](a)}{1 - \mu}, \quad (3.1.12)$$

with $I^0[v, \alpha](x) = \frac{\alpha}{2} \int_a^b e^{-\alpha|x-y|} v(y) dy$. And if we require

$$\mathcal{D}_0[v, \alpha](a) = C_a, \quad \text{and} \quad \mathcal{D}_0[v, \alpha](b) = C_b,$$

with given numbers C_a and C_b , then the boundary coefficients are obtained as

$$A_0 = \frac{1}{1 - \mu^2} \left(\mu (I^0[v, \alpha](b) - v(b) + C_b) - (I^0[v, \alpha](a) - v(a) + C_a) \right), \quad (3.1.13a)$$

$$B_0 = \frac{1}{1 - \mu^2} \left(\mu (I^0[v, \alpha](a) - v(a) + C_a) - (I^0[v, \alpha](b) - v(b) + C_b) \right). \quad (3.1.13b)$$

In fact, $-\alpha^2 \mathcal{D}_0[v, \alpha]$ is an approximation to v_{xx} , which we present the details in the section (6.2).

In the following, we will study the properties of the partial sums with different boundary conditions. Additionally, the parameter α would be chose carefully to make this scheme high order of accuracy and unconditionally stable properties.

3.1.2.1 Periodic boundary conditions

If A is a periodic function, we define the approximations of the first derivatives A_x^\pm using partial sums as

$$A_x^- \approx \mathcal{P}_k^- [A, \alpha](x) = \begin{cases} \alpha \sum_{p=1}^k \mathcal{D}_L^p [A, \alpha](x), & k = 1, 2, \\ \alpha \sum_{p=1}^k \mathcal{D}_L^p [A, \alpha](x) - \alpha \mathcal{D}_0 * \mathcal{D}_L^2 [A, \alpha](x), & k = 3, \end{cases} \quad (3.1.14a)$$

and

$$A_x^+ \approx \mathcal{P}_k^+[A, \alpha](x) = \begin{cases} -\alpha \sum_{p=1}^k \mathcal{D}_R^p[A, \alpha](x), & k = 1, 2, \\ -\alpha \sum_{p=1}^k \mathcal{D}_R^p[A, \alpha](x) + \alpha \mathcal{D}_0 * \mathcal{D}_R^2[A, \alpha](x), & k = 3. \end{cases} \quad (3.1.14b)$$

Note that we have an extra term for the case of $k = 3$. This term is necessary to ensure unconditional stability and show up in all MOLT approximations with $k > 2$. The scheme for $k > 2$ is $A(\alpha)$ - stable, however with the modification shown above for $k = 3$ scheme A - stable for properly chosen of the constant β [22, 23]. Then, we have the following theorem, which gives an error estimate for the partial sums approximation and has been proven in [22].

Theorem 3.1.1. *Suppose $v(x) \in C^{k+1}[a, b]$ is a periodic smooth function. Consider the operators D_* with the boundary treatment $\mathcal{D}_*(a) = \mathcal{D}_*(b)$. Here, $*$ can be L , R , and 0 . Then,*

$$\|A_x - \mathcal{P}_k^-[A, \alpha]\|_\infty = \mathcal{O}(1/\alpha^k), \quad \|A_x - \mathcal{P}_k^+[A, \alpha]\|_\infty = \mathcal{O}(1/\alpha^k). \quad (3.1.15)$$

Here, we take $\alpha = \beta/(c\Delta t)$, where c is the maximum wave speed and β is a constant independent of the time step Δt . Therefore, the accuracy for the approximation (3.1.14) to the $\partial_x A$ is $\mathcal{O}(\Delta t^k)$. Note that, to achieve k^{th} order accuracy in time, $k = 1, 2, 3$, we should employ the k^{th} order SSP RK method (3.1.2)-(3.1.4) as well as \mathcal{P}_k^\pm in (3.1.14). Moreover, if β is chosen appropriately, the semi-discrete scheme (without numerical approach to \mathcal{D}^p) is A -stable and hence allows for large time step evolution. Additionally, the linear stability of the method which argued in the following theorem has been proven in [22].

Theorem 3.1.2. For the linear equation $\phi_t + c\phi_x = 0$, (i.e. the Hamiltonian is linear) with periodic boundary conditions, we consider the k^{th} order SSP RK method as well as the k^{th} partial sum in (3.1.14), with $\alpha = \beta/(|c|\Delta t)$. Then there exists a constant $\beta_{k,\max} > 0$ for $k = 1, 2, 3$, such that the scheme is A-stable provided $0 < \beta \leq \beta_{k,\max}$. The constants $\beta_{k,\max}$ for $k = 1, 2, 3$ are summarized in Table 3.1.

Table 3.1: $\beta_{k,\max}$ in Theorem 3.1.2 for $k = 1, 2, 3$.

| | | | |
|------------------|---|---|-------|
| k | 1 | 2 | 3 |
| $\beta_{k,\max}$ | 2 | 1 | 1.243 |

Proof. Let's review the key points of proof for the case of $k = 1$. A von Neumann analysis is applied to the advection equation to obtain the amplification factor λ for the given ansatz $\phi^n = \hat{\phi}e^{ikx}$. According to the von Neumann analysis if $|\lambda| \leq 1$ for any k and time step Δt , then the scheme is unconditionally stable. Now we apply the Fourier transform in space to the operators \mathcal{D}_L and \mathcal{L}_L

$$\mathcal{L}_L = \mathcal{I} + \frac{1}{\alpha_L} \partial_x \quad \Rightarrow \quad \hat{\mathcal{L}}_L = 1 + \frac{ik}{\alpha_L}, \quad (3.1.16)$$

$$\mathcal{D}_L = \mathcal{I} - \mathcal{L}_L^{-1} \quad \Rightarrow \quad \hat{\mathcal{D}}_L = 1 - \frac{1}{\hat{\mathcal{L}}_L} = \frac{ik/\alpha_L}{1 + ik/\alpha_L}. \quad (3.1.17)$$

Now, once we apply the Forward Euler scheme and integral approximation

$$\phi^{n+1} = \phi^n - \Delta t \alpha_L \mathcal{D}_L[c\phi^n, \alpha_L], \quad (3.1.18)$$

where $\alpha_L = \frac{\beta}{(c\Delta t)}$. Thus,

$$\lambda = \frac{\phi^{n+1}}{\phi^n} = 1 - \beta \frac{ikc\Delta t/\beta}{1 + ikc\Delta t/\beta}. \quad (3.1.19)$$

For $\beta \leq 2$, the amplification factor satisfies $|\lambda| \leq 1$, which means the scheme is A - stable. In other words, the scheme is unconditionally stable for appropriately chosen constant value β from the table (3.1). The same argument holds for $k > 1$. This is discussed in [23, 24]. \square

3.1.2.2 Non periodic boundary conditions

Next, we introduce a modification of the partial sums (3.1.14) to achieve a higher order accuracy for the non-periodic case. Assume that we have some derivative values at boundary, i.e., $\partial_x^m A(a)$ and $\partial_x^m A(b)$, $m \geq 1$. Using integration by parts one can derive the following modified partial sums for $k \leq 3$ to deal with the non-periodic boundary conditions

$$A_x^- \approx \tilde{\mathcal{P}}_k^- [A, \alpha](x) = \begin{cases} \alpha \sum_{p=1}^k \mathcal{D}_L[A_{1,p}, \alpha](x), & k = 1, 2, \\ \alpha \sum_{p=1}^k \mathcal{D}_L[A_{1,p}, \alpha](x) - \alpha \mathcal{D}_0[A_{1,3}, \alpha](x), & k = 3, \end{cases} \quad (3.1.20a)$$

$$A_x^+ \approx \tilde{\mathcal{P}}_k^+ [A, \alpha](x) = \begin{cases} -\alpha \sum_{p=1}^k \mathcal{D}_R[A_{2,p}, \alpha](x), & k = 1, 2, \\ -\alpha \sum_{p=1}^k \mathcal{D}_R[A_{2,p}, \alpha](x) + \alpha \mathcal{D}_0[A_{2,3}, \alpha](x), & k = 3. \end{cases} \quad (3.1.20b)$$

And $A_{1,p}$ and $A_{2,p}$ are given as

$$\begin{cases} A_{1,1} = A, \\ A_{1,2} = \mathcal{D}_L[A_{1,1}, \alpha] - \sum_{m=2}^k \left(-\frac{1}{\alpha}\right)^m \partial_x^m A(a) e^{-\alpha(x-a)}, \\ A_{1,3} = \mathcal{D}_L[A_{1,2}, \alpha] + \sum_{m=2}^k (m-1) \left(-\frac{1}{\alpha}\right)^m \partial_x^m A(a) e^{-\alpha(x-a)}, \end{cases} \quad (3.1.21a)$$

$$\begin{cases} A_{2,1} = A, \\ A_{2,2} = \mathcal{D}_R[A_{2,1}, \alpha] - \sum_{m=2}^k \left(\frac{1}{\alpha}\right)^m \partial_x^m A(b) e^{-\alpha(b-x)}, \\ A_{2,3} = \mathcal{D}_R[A_{2,2}, \alpha] + \sum_{m=2}^k (m-1) \left(\frac{1}{\alpha}\right)^m \partial_x^m A(b) e^{-\alpha(b-x)}, \end{cases} \quad (3.1.21b)$$

where the boundary conditions for the operators are imposed as

$$\begin{aligned} \alpha \mathcal{D}_L[A_{1,1}, \alpha](a) &= A_x(a), & \alpha \mathcal{D}_R[A_{2,1}, \alpha](b) &= -A_x(b), \\ \alpha \mathcal{D}_L[A_{1,p}, \alpha](a) &= \alpha \mathcal{D}_R[A_{2,p}, \alpha](b) = 0, & \text{for } p &\geq 2, \\ \alpha \mathcal{D}_0[A_{*,3}, \alpha](a) &= \alpha \mathcal{D}_0[A_{*,3}, \alpha](b) = 0, & * &\text{ could be 1 or 2.} \end{aligned}$$

Then, the modified partial sum (3.1.20) agrees with the derivative values at the boundary

$$\widetilde{\mathcal{P}}_k^- [A, \alpha](a) = A_x(a), \quad \widetilde{\mathcal{P}}_k^+ [A, \alpha](b) = A_x(b).$$

Furthermore, we have the following theorem, which is a result of the Theorem 2.3 from [23].

Theorem 3.1.3. *Suppose $A \in \mathcal{C}^{k+1}[a, b]$. Then the modified partial sums (3.1.20) satisfy*

$$\|A_x - \widetilde{\mathcal{P}}_k^- [A, \alpha]\|_\infty = \mathcal{O}(1/\alpha^k), \quad \|A_x - \widetilde{\mathcal{P}}_k^+ [A, \alpha]\|_\infty = \mathcal{O}(1/\alpha^k), \quad k = 1, 2, 3. \quad (3.1.22)$$

Again, we take $\alpha = \beta/(c\Delta t)$ in application, where c is the maximum wave speed and β is taken as the same as periodic boundary condition, see Table 3.1.

As we have seen in (3.1.21), we need the derivatives $\partial_x^m A(a)$ and $\partial_x^m A(b)$, $m \geq 1$, for non periodic boundary conditions. Here, we will only focus on the outflow boundary conditions. High order extrapolations are used to get all the derivatives at boundaries (that is, there

are no physical boundary given). The details of the general non-periodic conditions can be found in our previous work [23].

3.1.2.3 Space Discretization and WENO-based Quadrature

According to the kernel based method, the spatial derivatives can be approximated by the partial sums based on an integral formulation. A fully discrete numerical solution is then obtained by discretizing \mathcal{D}_L and \mathcal{D}_R operators in space. In this subsection we will give the details of the spatial discretization of the \mathcal{D}_L and \mathcal{D}_R operators and the WENO-based quadrature formulation to approximate the convolution integrals appearing in the \mathcal{D}_L and \mathcal{D}_R operators.

Suppose we divide the domain $[a, b]$ with $N + 1$ uniformly distributed grid points

$$\Delta x = (b - a)/N, \quad x_i = a + i\Delta x, \quad i = 0, 1, \dots, N.$$

The convolution integrals $I_i^L = I^L[v, \alpha](x_i)$ and $I_i^R = I^R[v, \alpha](x_i)$ satisfy a recursive relation

$$I_i^L = e^{-\alpha\Delta x_i} I_{i-1}^L + J_i^L, \quad i = 1, \dots, N, \quad I_0^L = 0, \quad (3.1.23a)$$

$$I_i^R = e^{-\alpha\Delta x_{i+1}} I_{i+1}^R + J_i^R, \quad i = 0, \dots, N - 1, \quad I_N^R = 0, \quad (3.1.23b)$$

where,

$$J_i^L = \alpha \int_{x_{i-1}}^{x_i} v(y) e^{-\alpha(x_i - y)} dy, \quad J_i^R = \alpha \int_{x_i}^{x_{i+1}} v(y) e^{-\alpha(y - x_i)} dy. \quad (3.1.24)$$

Since there is a unique polynomial $p(x)$ of degree at most k that interpolates $v(x)$ at the

nodes in the interpolation stencil $S(i) = \{x_{i-r}, \dots, x_{i-r+k}\}$, which contains x_{i-1} and x_i , we can approximate J_i^L with k^{th} order accuracy by

$$J_i^L \approx \alpha \int_{x_{i-1}}^{x_i} p(y) e^{-\alpha(x_i-y)} dy, \quad (3.1.25)$$

Note that, the integral on the right hand side can be evaluated exactly. Similarly, J_i^R can be approximated by

$$J_i^R \approx \alpha \int_{x_i}^{x_{i+1}} p(y) e^{-\alpha(y-x_i)} dy, \quad (3.1.26)$$

with polynomial $p(x)$ interpolating $v(x)$ on stencil $S(i) = \{x_{i+r-k}, \dots, x_{i+r}\}$, which includes x_i and x_{i+1} .

Since the quadratures with a fixed stencil for approximating the J_i^L and J_i^R may develop spurious oscillations which violates the entropy solutions, we will use WENO-based quadrature formula and the nonlinear filter to control oscillations and capture the correct solution, which is proposed in [23]. Here we will provide a brief description of methodology.

To summarize, if A_x is periodic function, then we will be using the following modified sums framework instead of (3.1.14) for approximation of A_x^\pm at x_i :

$$A_{x,i}^- = \alpha \mathcal{D}_L[A, \alpha](x_i) + \alpha \sum_{p=2}^k \sigma_{i,L}^{p-2} \mathcal{D}_L^p[A, \alpha](x_i), \quad (3.1.27a)$$

$$A_{x,i}^+ = -\alpha \mathcal{D}_R[A, \alpha](x_i) - \alpha \sum_{p=2}^k \sigma_{i,R}^{p-2} \mathcal{D}_R^p[A, \alpha](x_i); \quad (3.1.27b)$$

and if A_x is non periodic function, then we will use the following formulation instead of

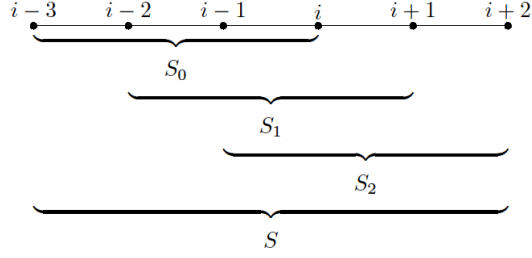


Figure 3.1: The structure of the stencils in WENO integration.

(3.1.20)

$$A_{x,i}^- = \alpha \mathcal{D}_L[A_{1,1}, \alpha](x_i) + \alpha \sum_{p=2}^k \sigma_{i,L}^{p-2} \mathcal{D}_L[A_{1,p}, \alpha](x_i), \quad (3.1.28a)$$

$$A_{x,i}^+ = -\alpha \mathcal{D}_R[A_{2,1}, \alpha](x_i) - \alpha \sum_{p=2}^k \sigma_{i,R}^{p-2} \mathcal{D}_R[A_{2,p}, \alpha](x_i). \quad (3.1.28b)$$

Moreover, we only use the WENO formulation when $p = 1$ while we use cheap high order linear formulation (3.1.25) and (3.1.26) for the case $p > 1$. The filters $\sigma_{i,L}$ and $\sigma_{i,R}$ are obtained based on the smoothness indicators from the WENO quadrature.

The fifth order WENO quadrature for J_i^L is presented here as an example. The related stencil is given in Figure 4.1. We choose the big stencil as $S(i) = \{x_{i-3}, \dots, x_{i+2}\}$ and the three small stencils as $S_r(i) = \{x_{i-3+r}, \dots, x_{i+r}\}$, $r = 0, 1, 2$.

1. We approximate the integrals on each small stencils $S_r(i)$ as follows

$$J_{i,r}^L = \alpha \int_{x_{i-1}}^{x_i} e^{-\alpha(x_i-y)} p_r(y) dx, = \sum_{j=0}^3 c_j^{(r)} v_{i-3+r+j}, \quad (3.1.29)$$

where $p_r(x)$ is the polynomial interpolating $v(x)$ on nodes $S_r(i)$, and the coefficients $c_j^{(r)}$ depend on α and the cell size Δx , but not on v .

2. Similarly, on the big stencil $S(i)$, we obtain

$$J_i^L = \alpha \int_{x_{i-1}}^{x_i} e^{-\alpha(x_i-y)} p(y) dx = \sum_{r=0}^2 d_r J_{i,r}^L, \quad (3.1.30)$$

with the linear weights d_r satisfying $\sum_{r=0}^2 d_r = 1$.

3. We develop the following nonlinear weights ω_r using the linear weights d_r

$$\omega_r = \tilde{\omega}_r / \sum_{s=0}^2 \tilde{\omega}_s, \quad r = 0, 1, 2, \quad (3.1.31)$$

with

$$\tilde{\omega}_r = d_r \left(1 + \frac{\tau_5}{\epsilon + \beta_r} \right).$$

We take $\epsilon = 10^{-6}$ as a small positive number, $\epsilon > 0$, in our numerical test problems to avoid zero at the denominator. The smoothness indicator β_r is determined as

$$\beta_r = \sum_{l=2}^3 \int_{x_{i-1}}^{x_i} \Delta x_i^{2l-3} \left(\frac{\partial^l p_r(x)}{\partial x^l} \right)^2 dx, \quad (3.1.32)$$

which is used to measure the relative smoothness of the function $v(x)$ in the stencil $S_r(i)$. Here, $\tau_5 = |\beta_0 - \beta_2|$. Furthermore, we introduce a parameter ξ_i as

$$\xi_i = \frac{\beta_{min}}{\beta_{max}}, \quad (3.1.33)$$

which will be use to create the nonlinear filter. Here,

$$\beta_{max} = 1 + \left(\frac{\tau_5}{\epsilon + \min(\beta_0, \beta_2)} \right)^2, \quad \beta_{min} = 1 + \left(\frac{\tau_5}{\epsilon + \max(\beta_0, \beta_2)} \right)^2.$$

Note that we have developed the nonlinear weights using the idea of the WENO-Z method proposed in [13], which has less dissipation and higher resolution comparing to the original WENO method.

4. Lastly, we obtain the approximation

$$J_i^L = \sum_{r=0}^2 \omega_r J_{i,r}^L. \quad (3.1.35)$$

The filter $\sigma_{i,L}$ is determined as

$$\sigma_{i,L} = \min(\xi_{i-1}, \xi_i). \quad (3.1.36)$$

All coefficients are given in Appendix. The process to obtain J_i^R and $\sigma_{i,R}$ is mirror symmetric to that of J_i^L and $\sigma_{i,L}$ with respect to point x_i .

To close this section, we summarize the proposed method for approximating one-dimensional problem (3.1.1) in the following algorithm flowchart.

Given the function u^n , the approximation order $k \leq 3$, the mesh size Δx and the time step Δt .

1. Choose β from the Table 3.1. Compute $c = \max |H'(\phi)|$ at time t^n .
2. On each inner stage of the k^{th} order SSP RK scheme:
 - (a) Compute c , and then obtain parameters $\alpha = \beta/(c\Delta t)$. For non periodic boundary conditions, compute the derivatives $\partial_x^m A(a)$ and $\partial_x^m A(b)$, $m = 1, \dots, k$.

- (b) Apply \mathcal{D}_L and \mathcal{D}_R on A , respectively. Use the WENO quadrature to calculate $J^{L,R}$ and at the same time obtain the nonlinear filter $\sigma_{L,R}$. Compute $I^{L,R}$ via (6.2.6) and then calculate the parameter A_L and B_R based on the boundary condition. Combine $I^{L,R}$, A_L and B_R to construct $\mathcal{D}_L[A]$ and $\mathcal{D}_R[A]$.
- (c) For $k > 1$, further construct $\mathcal{D}_L^p[A] = \mathcal{D}_L^{p-1}[\mathcal{D}_L[A]]$ and $\mathcal{D}_R^p[A] = \mathcal{D}_R^{p-1}[\mathcal{D}_R[A]]$, or the modified functions $\mathcal{D}_{L,R}[A_{1,2,k}]$ in (3.1.21), by a similar procedure for $1 < p \leq k$. WENO quadrature is not needed for construction of these high order terms.
- (d) Construct A_x^\pm based on the the partial sum approximations (3.1.14) or (3.1.20).
- (e) Substitute into the Lax-Friedrichs Hamiltonian flux (3.1.5) and update the solution accordingly.
-

3.1.3 2D magnetic potential equation

In this section we develop our proposed MOLT-HJ scheme in 2D, which still use the WENO-quadrature formulation presented in the previous section to approximate the convolution integrals. According to the Constrained Transport formulation described in Section 2.5, we must update the solution of the magnetic potential equation by solving a discrete version of the following equation

$$A_t^3 + u^1(x, y)A_x^3 + u^2(x, y)A_y^3 = 0 \quad (3.1.37)$$

where the velocity components u^1 and u^2 are known from the previous time step due to the solution of the base part, HCL. Since the velocity functions are given, we can consider

(3.1.37) as a Hamilton-Jacobi equation

$$A_t^3 + H(A_x^3, A_y^3) = 0 \quad (3.1.38)$$

with Hamiltonian flux

$$H(A_x^3, A_y^3) = u^1(x, y)A_x^3 + u^2(x, y)A_y^3. \quad (3.1.39)$$

We can directly apply a two dimensional version of the kernel-based framework presented in Section 3.1.1. The 2D semi-discrete scheme can be written as

$$\frac{dA_{i,j}^3(t)}{dt} = -\hat{H}(A_x^{3-}|_{i,j}, A_x^{3+}|_{i,j}, A_y^{3-}|_{i,j}, A_y^{3+}|_{i,j}) \quad (3.1.40)$$

on each point (x_i, y_j) , where \hat{H} is a Lipschitz continuous Hamiltonian flux. We use the Lax-Friedrichs flux and the equation (3.1.40) becomes

$$\begin{aligned} \frac{dA_{i,j}^3(t)}{dt} = & -u_{i,j}^1 \left(\frac{A_x^{3-} + A_x^{3+}}{2} \right) |_{i,j} - u_{i,j}^2 \left(\frac{A_y^{3-} + A_y^{3+}}{2} \right) |_{i,j} \\ & + c_1 \left(\frac{A_x^{3+} - A_x^{3-}}{2} \right) |_{i,j} + c_2 \left(\frac{A_y^{3+} - A_y^{3-}}{2} \right) |_{i,j} \end{aligned} \quad (3.1.41)$$

with

$$c_1 = \max_{i,j} |u_{i,j}^1| \quad \text{and} \quad c_2 = \max_{i,j} |u_{i,j}^2|.$$

We remark that the scheme (3.1.41) with this global c_m can be very dissipative for some Hamilton-Jacobi equations. There is another way of choosing c_m which is by taking the max

value on the local stencil.

The approximations $A_x^{3\pm}|_{i,j}$ and $A_y^{3\pm}|_{i,j}$ to the derivatives of functions $A_x(x, y)$ and $A_y(x, y)$ at (x_i, y_j) , respectively calculated directly using one dimensional formulation of the scheme, e.g., when computing $A_x^{3\pm}$, we fix y and apply 1D scheme in x -direction. For example, when A_x is periodic in x -direction, we get

$$A_x^- \approx \alpha_1 \mathcal{D}_L^p[A(\cdot, y), \alpha_1](x) + \alpha_1 \sum_{p=2}^k \sigma_{i,L}^{p-2} \mathcal{D}_L^p[A(\cdot, y), \alpha_1](x),$$

$$A_x^+ \approx -\alpha_1 \mathcal{D}_R[A(\cdot, y), \alpha_1](x) - \alpha_1 \sum_{p=2}^k \sigma_{i,R}^{p-2} \mathcal{D}_R^p[A(\cdot, y), \alpha_1](x).$$

Here, we choose $\alpha_1 = \beta/(c_1 \Delta t)$. Similarly, to approximate A_y^\pm , we fix x and obtain

$$A_y^- \approx \alpha_2 \mathcal{D}_L[A(x, \cdot), \alpha_2](y) + \alpha_2 \sum_{p=2}^k \sigma_{i,L}^{p-2} \mathcal{D}_L^p[A(x, \cdot), \alpha_2](y),$$

$$A_y^+ \approx -\alpha_2 \mathcal{D}_R[A(x, \cdot), \alpha_2](y) - \alpha_2 \sum_{p=2}^k \sigma_{i,R}^{p-2} \mathcal{D}_R^p[A(x, \cdot), \alpha_2](y),$$

with $\alpha_2 = \beta/(c_2 \Delta t)$. Note that in the 2D case, we need to choose β_{max} as half of that for the 1D case to ensure the unconditional stability of the scheme.

At an outflow boundary condition, we still use extrapolation with suitable order of accuracy for the derivative values, as in the 1D formulation. In the case of outflow boundary conditions, in the sense of characteristic propagation, it is natural to apply high order extrapolation to get the boundary values.

3.1.4 3D magnetic potential equation

In this section we present MOLT-HJ scheme in 3D, which is a key scheme in our proposed 3D MHD solver. The main accomplishment in 3D MOLT-HJ scheme is that we avoid the artificial diffusion limiters, which were needed in the previous work [29]. Note that we can include those artificial limiters to our 3D MOLT-HJ solver to compare the new method with the old method. Although the evolution equation for the 3D magnetic potential (2.3.4) is significantly different from the evolution equation for the 2D scalar magnetic potential (2.3.9), we can still directly apply the scheme presented in section (3.1.1) to the 3D case. In our previous paper [29], we needed an artificial resistivity term in the 3D case. However, with the kernel based approach we no longer need those artificial terms in our equations, since our method is fully implicit.

Writing out the magnetic vector potential equation derived in section (2.3) in component form we have:

$$\partial_t A^1 = u^2(\partial_x A^2) + u^3(\partial_x A^3) - u^2(\partial_y A^1) - u^3(\partial_z A^1) \quad (3.1.42)$$

$$\partial_t A^2 = -u^1(\partial_x A^2) + u^1(\partial_y A^1) + u^3(\partial_y A^3) - u^3(\partial_z A^2) \quad (3.1.43)$$

$$\partial_t A^3 = -u^1(\partial_x A^3) - u^2(\partial_y A^3) + u^1(\partial_z A^1) + u^2(\partial_z A^2) \quad (3.1.44)$$

with $\mathbf{A} = (A^1, A^2, A^3)$ and $\mathbf{u} = (u^1, u^2, u^3)$. While \mathbf{A} in 3D is not strictly a H-J equation, with the new implicit approach we can simply apply the ideas from the 2D case. Then we can obtain the following equations using the Lax-Friedrichs flux splitting:

$$\frac{dA^1(t)}{dt} = u^2 \frac{(A_x^{2+} + A_x^{2-})}{2} - c_2 \frac{(A_x^{2-} - A_x^{2+})}{2} + u^3 \frac{(A_x^{3+} + A_x^{3-})}{2} - c_3 \frac{(A_x^{3-} - A_x^{3+})}{2}$$

$$-u^2 \frac{(A_y^{1+} + A_y^{1-})}{2} - c_2 \frac{(A_y^{1-} - A_y^{1+})}{2} - u^3 \frac{(A_z^{1+} + A_z^{1-})}{2} - c_3 \frac{(A_z^{1-} - A_z^{1+})}{2}, \quad (3.1.45a)$$

$$\begin{aligned} \frac{dA^2(t)}{dt} = & -u^1 \frac{(A_x^{2+} + A_x^{2-})}{2} - c_1 \frac{(A_x^{2-} - A_x^{2+})}{2} + u^1 \frac{(A_y^{1+} + A_y^{1-})}{2} - c_1 \frac{(A_y^{1-} - A_y^{1+})}{2} \\ & + u^3 \frac{(A_y^{3+} + A_y^{3-})}{2} - c_3 \frac{(A_y^{3-} - A_y^{3+})}{2} - u^3 \frac{(A_z^{2+} + A_z^{2-})}{2} - c_3 \frac{(A_z^{2-} - A_z^{2+})}{2}, \end{aligned} \quad (3.1.45b)$$

$$\begin{aligned} \frac{dA^3(t)}{dt} = & -u^1 \frac{(A_x^{3+} + A_x^{3-})}{2} - c_1 \frac{(A_x^{3-} - A_x^{3+})}{2} - u^2 \frac{(A_y^{3+} + A_y^{3-})}{2} - c_2 \frac{(A_y^{3-} - A_y^{3+})}{2} \\ & + u^1 \frac{(A_z^{1+} + A_z^{1-})}{2} - c_1 \frac{(A_z^{1-} - A_z^{1+})}{2} + u^2 \frac{(A_z^{2+} + A_z^{2-})}{2} - c_2 \frac{(A_z^{2-} - A_z^{2+})}{2}, \end{aligned} \quad (3.1.45c)$$

at (x_i, y_j, z_k) , where

$$c_1 = \max_{i,j,k} |u_{i,j,k}^1|, \quad c_2 = \max_{i,j,k} |u_{i,j,k}^2|, \quad \text{and} \quad c_3 = \max_{i,j,k} |u_{i,j,k}^3|.$$

Similarly, we use 1D kernel-based formulation to approximate the derivatives of the magnetic vector potential components $A_x^{*\pm}$, $A_y^{*\pm}$, and $A_z^{*\pm}$, where $*$ denotes 1, 2 and 3. In addition, since the density or pressure may become negative in some problems such as the blast wave problem, we use the positivity preserving limiter idea developed in our previous work [29]. For more details on positivity limiter, see [26, 28, 66]

3.2 Central finite difference discretization of $\nabla \times \mathbf{A}$

According to the Constrained Transport formulation, we applied a discrete curl operator to the magnetic potential at each stage of CT framework for the purpose of obtaining a divergence free magnetic field. Here we will present the strategy we used to approximate the

curl operator.

3.2.1 Curl in 2D

We apply a discrete version of 2D curl to the equation (2.3.8) as

$$B_{i,j}^1 := D_y|_{i,j}A^3 \quad \text{and} \quad B_{i,j}^2 := -D_x|_{i,j}A^3, \quad (3.2.1)$$

where D_x and D_y are the discrete versions of the partial derivatives ∂_x and ∂_y . We use these version of curls to satisfy the discrete divergence free constraint as follows

$$\nabla \cdot B_{i,j} := D_x|_{i,j}B^1 + D_y|_{i,j}B^2 = D_xD_y|_{i,j}A^3 - D_yD_x|_{i,j}A^3 = 0.$$

Here, we choose 4th-order central finite differences to get high order accuracy

$$D_x|_{i,j}A^3 := \frac{1}{12\Delta x}(A_{i-2,j}^3 - 8A_{i-1,j}^3 + 8A_{i+1,j}^3 - A_{i+2,j}^3), \quad (3.2.2a)$$

$$D_y|_{i,j}A^3 := \frac{1}{12\Delta y}(A_{i,j-2}^3 - 8A_{i,j-1}^3 + 8A_{i,j+1}^3 - A_{i,j+2}^3), \quad (3.2.2b)$$

where $A = A^3$ is only third component of magnetic potential.

3.2.2 Curl in 3D

We use the following discrete version of the 3D curl

$$B_{i,j,k}^1 := D_y|_{i,j,k}A^3 - D_z|_{i,j,k}A^2, \quad (3.2.3a)$$

$$B_{i,j,k}^2 := D_z|_{i,j,k}A^1 - D_x|_{i,j,k}A^3, \quad (3.2.3b)$$

$$B_{i,j,k}^3 := D_x|_{i,j,k}A^2 - D_y|_{i,j,k}A^1, \quad (3.2.3c)$$

where D_x , D_y , and D_z are notations for the discrete versions of partial derivatives ∂_x , ∂_y and ∂_z , respectively. With these versions of curls, we get the following divergence free condition satisfied

$$\begin{aligned} \nabla \cdot B_{i,j,k} &:= D_x|_{i,j,k}B^1 + D_y|_{i,j,k}B^2 + D_z|_{i,j,k}B^3 \\ &= D_xD_y|_{i,j,k}A^3 - D_xD_z|_{i,j,k}A^2 + D_yD_z|_{i,j,k}A^1 - D_yD_x|_{i,j,k}A^3 \\ &\quad + D_zD_x|_{i,j,k}A^2 - D_zD_y|_{i,j,k}A^1 \\ &= 0 \end{aligned} \quad (3.2.4)$$

As in 2D case, we use 4th-order central finite differences to get high order accuracy

$$D_x|_{i,j,k}A^* := \frac{1}{12\Delta x}(A_{i-2,j,k}^* - 8A_{i-1,j,k}^* + 8A_{i+1,j,k}^* - A_{i+2,j,k}^*), \quad (3.2.5a)$$

$$D_y|_{i,j,k}A^* := \frac{1}{12\Delta y}(A_{i,j-2,k}^* - 8A_{i,j-1,k}^* + 8A_{i,j+1,k}^* - A_{i,j+2,k}^*), \quad (3.2.5b)$$

$$D_z|_{i,j,k}A^* := \frac{1}{12\Delta z}(A_{i,j,k-2}^* - 8A_{i,j,k-1}^* + 8A_{i,j,k+1}^* - A_{i,j,k+2}^*). \quad (3.2.5c)$$

3.3 Positivity Limiter

In this section we will give an explanation of the positivity limiter strategy that is used in several test problems in this work. Some test problems that has strong shock sometimes cause negative density or pressure in simulations. These negative quantities can create complex wave speeds which violates the hyperbolicity of the MHD system and ruin the numerical simulations. In the literature there have been many works addressing this problem

[7, 80, 77, 76, 27, 66]. A positivity limiting strategy was developed in the previous work [29] is also being utilized in this work to avoid negative density and pressure.

We will present a brief overview of the positivity limiter on one-dimensional MHD system,

$$\frac{\partial q}{\partial t} + \frac{\partial \mathbf{F}(q)}{\partial x} = 0 \quad (3.3.1)$$

The base scheme WENO-HCL is applied to the MHD equations to update the conserved quantities with a conservative form as

$$\frac{dq_i(t)}{dt} + \frac{1}{\Delta x} \left(\hat{\mathbf{F}}_{i+\frac{1}{2}} - \hat{\mathbf{F}}_{i-\frac{1}{2}} \right) = 0 \quad (3.3.2)$$

where $\hat{\mathbf{F}}_{i+\frac{1}{2}}$ is a numerical flux obtained by WENO-HCL scheme. We can apply time discretization to the semi-discrete equation (3.3.2) with third-order SSP-RK method

$$L(q_i^n) = -\frac{1}{\Delta x} \left(\hat{\mathbf{F}}_{i+\frac{1}{2}}^n - \hat{\mathbf{F}}_{i-\frac{1}{2}}^n \right). \quad (3.3.3)$$

The numerical fluxes reconstructions based on q^n , $q^{(1)}$, and $q^{(2)}$ are $\hat{\mathbf{F}}_{i+\frac{1}{2}}^n$, $\hat{\mathbf{F}}_{i+\frac{1}{2}}^{(1)}$, and $\hat{\mathbf{F}}_{i+\frac{1}{2}}^{(2)}$, respectively. Thus, considering $\hat{\mathbf{F}}_{i+\frac{1}{2}}^{rk}$ a linear combination of numerical fluxes from different stages, the final stage of RK scheme can be written as

$$q_i^{n+1} = q_i^n - \lambda \left(\hat{\mathbf{F}}_{i+\frac{1}{2}}^{rk} - \hat{\mathbf{F}}_{i-\frac{1}{2}}^{rk} \right) \quad (3.3.4)$$

where

$$\lambda = \frac{\Delta t}{\Delta x}, \quad \hat{\mathbf{F}}_{i+\frac{1}{2}}^{rk} = \frac{1}{6} \left(\hat{\mathbf{F}}_{i+\frac{1}{2}}^n + 4\hat{\mathbf{F}}_{i+\frac{1}{2}}^{(2)} + \hat{\mathbf{F}}_{i+\frac{1}{2}}^{(1)} \right). \quad (3.3.5)$$

The idea of the positivity limiter is to modifying the numerical flux $\hat{\mathbf{F}}_{i+\frac{1}{2}}^{rk}$ by a positivity preserving flux to guarantee the positivity of the high order solutions by the WENO method as follows

$$\tilde{\mathbf{F}}_{i+\frac{1}{2}} = \theta_{i+\frac{1}{2}}(\hat{\mathbf{F}}_{i+\frac{1}{2}}^{rk} - \hat{\mathbf{f}}_{i+\frac{1}{2}}) + \hat{\mathbf{f}}_{i+\frac{1}{2}} \quad (3.3.6)$$

with the limiting parameter $\theta_{i+\frac{1}{2}} \in [0, 1]$. Here, the $\hat{\mathbf{f}}_{i+\frac{1}{2}}$ is the Lax-Friedrichs flux and formulated as

$$\hat{\mathbf{f}}_{i+\frac{1}{2}} = \frac{1}{2}(\mathbf{f}(q_{j+1}^n) + \mathbf{f}(q_i^n) - \alpha(q_{j+1}^n - q_i^n)) \quad (3.3.7)$$

where the α is the maximal wave speed

$$\alpha = \max_i (|u^x| + c_f) \quad (3.3.8)$$

with c_f as the fast speed of the MHD system. There are two steps for the positivity preserving limiting procedure. The first step is to guarantee the positivity of the computed density. We will give the following notations: \hat{f}^ρ is the first order flux of the density in $\hat{\mathbf{f}}$; f^ρ and \tilde{f}^ρ are the flux components in \mathbf{F}^{rk} and $\tilde{\mathbf{F}}$, respectively. We seek upper bounds $\Lambda_{\pm\frac{1}{2}, I_i}^\rho$ of the limiting parameters $\theta_{i\pm\frac{1}{2}}$ at each cell I_i so that

$$(\theta_{i-\frac{1}{2}}, \theta_{i+\frac{1}{2}}) \in S_{\rho, I_i} = [0, \Lambda_{-\frac{1}{2}, I_i}^\rho] \times [0, \Lambda_{+\frac{1}{2}, I_i}^\rho] \quad (3.3.9)$$

and the computed density is being positive.

$$\rho_i^{n+1}(\theta_{i-\frac{1}{2}}, \theta_{i+\frac{1}{2}}) \geq \epsilon_p^{n+1}. \quad (3.3.10)$$

The second step is to preserve positive pressure. We describe a subset of the S_{ρ, I_i} as

$$S_{p, I_i} = \{(\theta_{i-\frac{1}{2}}, \theta_{i+\frac{1}{2}}) \in [0, \Lambda_{-\frac{1}{2}, I_i}^\rho] \times [0, \Lambda_{+\frac{1}{2}, I_i}^\rho]\} \quad (3.3.11)$$

and then we describe a rectangle inside of S_{p, I_i} as

$$R_{\rho, p, I_i} = [0, \Lambda_{-\frac{1}{2}, I_i}] \times [0, \Lambda_{+\frac{1}{2}, I_i}]. \quad (3.3.12)$$

such that the pressure function $p_i^{n+1}(\theta_{i-\frac{1}{2}}, \theta_{i+\frac{1}{2}})$ is positive,

$$p_i^{n+1}(\theta_{i-\frac{1}{2}}, \theta_{i+\frac{1}{2}}) \geq \epsilon_p^{n+1}. \quad (3.3.13)$$

At the end of the this procedure for all j , we get

$$\theta_{i+\frac{1}{2}} = \min(\Lambda_{-\frac{1}{2}, I_i}, \Lambda_{+\frac{1}{2}, I_i}) \quad (3.3.14)$$

The positivity preserving limiter strategy is used to guarantee the positivity of the solution at the final RK stage. So, we preserve numerical solutions with positive density and pressure at the end of the step 1 in the Constrained Transport procedure. Also, we use option 2 in the CT framework to preserve positive pressure after magnetic field is updated.

The details are omitted here. For the details, see [29].

3.4 Numerical Results

In this section, we present the numerical results to demonstrate the accuracy and efficiency of the new method. We demonstrate the robustness of the proposed method on the field loop test problem in 2D and 3D. We validate that the new method works well for the blast wave and strong shocks by comparing with the old method [29] and then adding diffusion limiter into the new method. The main accomplishment is that the new method achieves a peak of 320, which is 23% higher than the old method, and thus is far less isotropic around the peak than the old method. We use third order SSP RK method for time discretization. Time step is chosen as

$$\Delta t = \frac{\text{CFL}}{em * cd} \quad (3.4.1)$$

where the $\beta = 0.8$, the CFL number is 0.5, $em = \max(\lambda^5, \lambda^6)$, $cd = \frac{1}{\Delta x} + \frac{1}{\Delta y}$ for 2D and $cd = \frac{1}{\Delta x} + \frac{1}{\Delta y} + \frac{1}{\Delta z}$ for 3D. In all examples, unless stated, the results being presented are from kernel based-CT. We denote the new method as kernel based-CT and our WENO-HJ-CT method as our previous method.

3.4.1 Smooth vortex test in MHD

We first test the smooth vortex problem in 2D with non zero magnetic field to show the accuracy of the method within the constrained transport formulation. The initial conditions are

$$(\rho, u^1, u^3, u^3, p, B^1, B^2, B^3) = (1, 1, 1, 0, 1, 0, 0, 0)$$

with perturbations on u^1, u^2, B^1, B^2 and p as :

$$\begin{aligned}(\delta u^1, \delta u^2) &= \frac{\mu}{2\pi} e^{0.5(1-r^2)}(-y, x). \\(\delta B^1, \delta B^2) &= \frac{\kappa}{2\pi} e^{0.5(1-r^2)}(-y, x). \\ \delta p &= \frac{\mu y(1-r^2) - \kappa^2}{8\pi^2} e^{(1-r^2)}.\end{aligned}$$

And the initial condition for magnetic potential is

$$A^3(0, x, y) = \frac{\mu}{2\pi} e^{0.5(1-r^2)}$$

where $r^2 = x^2 + y^2$. The vortex strength is taken as $\mu = 5.389489439$ and $\kappa = \sqrt{2}\mu$ such that the lowest pressure is around 5.3×10^{-12} which happens in the center of the vortex. The domain is $[-10, 10] \times [-10, 10]$ and periodic boundary condition is used on all four boundaries. In Table 3.2, we present the errors of B at $t = 0.05$ with the mesh size 160×160 . We observe fourth order accuracy in space for \mathbf{B} . Note that we use fifth order WENO scheme for the solution of \mathbf{A} , but since we take derivative of the magnetic potential equation to get magnetic field equation, we loose an order of accuracy for \mathbf{B} , thus we get fourth order in space.

Additionally, in Figure 3.2 we show the results at the final time $t = 20$ with 160×160 mesh size. Those plots show the solution after one period at $t = 20$.

3.4.2 2D Orszag-Tang Vortex

The Orszag-Tang vortex problem is a standard model problem for testing $\nabla \cdot \mathbf{B} = 0$ condition, since the solution of the problem is sensitive to divergence errors at late times.

Table 3.2: Smooth vortex problem. Errors of B and orders of accuracy.

| $N_x \times N_y$ | L_1 error | order | L_∞ error | order |
|------------------|-------------|-------|------------------|-------|
| 20×20 | 2.827E-03 | – | 1.479E-01 | – |
| 40×40 | 2.982E-04 | 3.245 | 1.839E-02 | 3.007 |
| 80×80 | 1.861E-05 | 4.003 | 1.327E-03 | 3.793 |
| 160×160 | 1.102E-06 | 4.078 | 1.126E-04 | 3.559 |
| 320×320 | 7.260E-08 | 3.924 | 1.170E-05 | 3.267 |

The initial conditions are given as

$$(\rho, u^1, u^2, u^3, p, B^1, B^2, B^3) = (\gamma^2, -\sin(y), \sin(x), 0, \gamma, -\sin(y), \sin(2x), 0),$$

where $\gamma = 5/3$ is the ideal gas constant and the initial magnetic potential:

$$A^3 = 0.5 \cos(2x) + \cos(y)$$

The computational domain is $[0, 2\pi] \times [0, 2\pi]$ and periodic boundary conditions are used everywhere. We test the schemes with 192×192 grid points. Although the problem has smooth initial condition, as solution progresses, several shock waves and a vortex shape appear in the center of the domain. In Figure 3.3, we show density ρ at time $t = 3$, and compare the results with our previous method [29]. We can see that they are in good agreement.

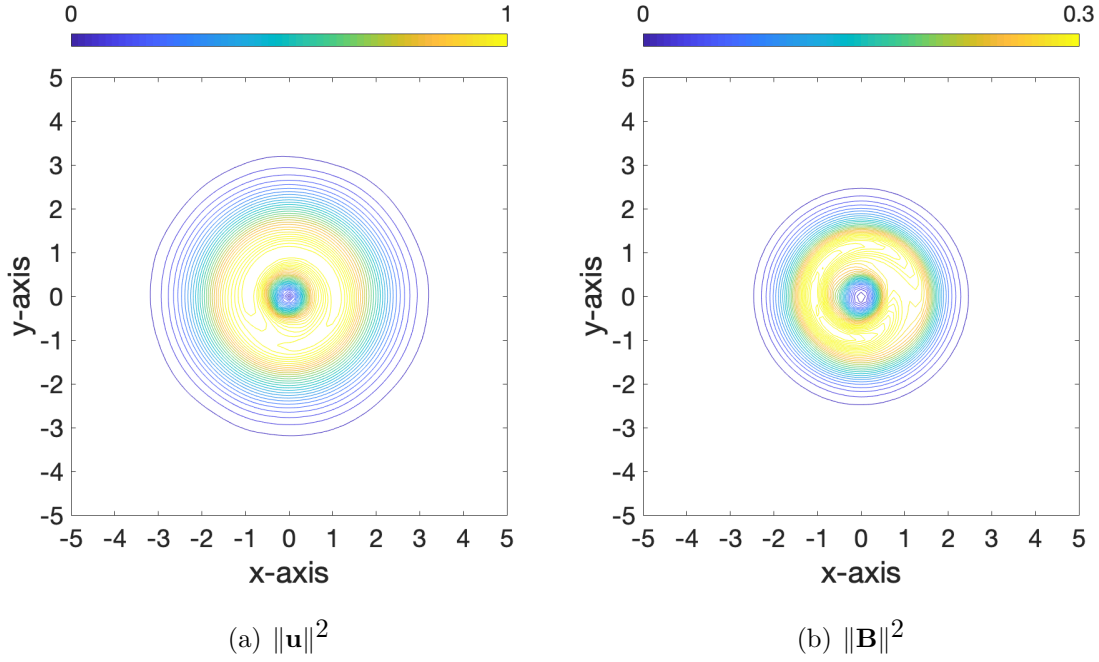


Figure 3.2: Smooth vortex problem. L^2 norms of \mathbf{u} and \mathbf{B} at $t = 20$ with 160×160 grid points. Domain for the plots is $[-5, 5] \times [-5, 5]$.

3.4.3 Cloud Shock

In this section we consider the 2D cloud-shock interaction problem, which models a strong shock passing through a dense stationary bubble. The initial conditions include

$$(\rho, u^1, u^2, u^3, p, B^1, B^2, B^3) = \begin{cases} (3.86859, 11.2536, 0, 0, 167.345, 0, 2.1826182, -2.1826182) & x < 0.05, \\ (1, 0, 0, 0, 1, 0, 0.56418958, 0.56418958) & x > 0.05, \end{cases}$$

and a circular cloud of density $\rho = 10$ and radius $r = 0.15$ centered at $(x, y) = (0.25, 0.5)$.

The computational domain is $[0, 1] \times [0, 1]$ with mesh 512×512 . We use inflow boundary condition at left boundary and outflow boundary condition elsewhere. The initial condition

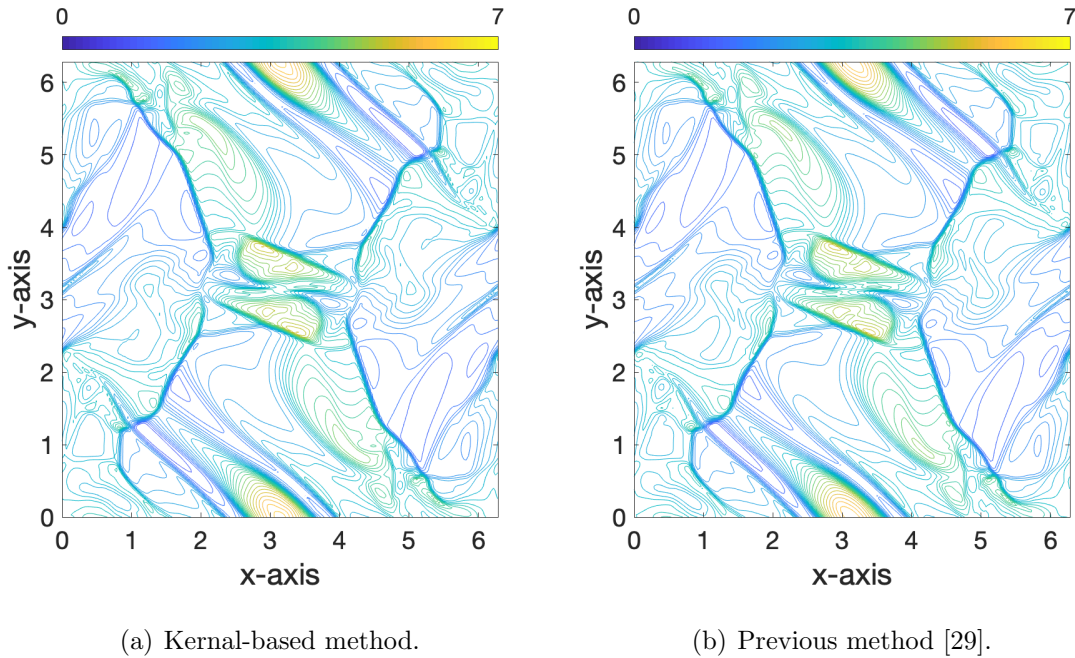


Figure 3.3: Orszag-Tang vortex problem. Contour plots of density at $t = 3$ with 192×192 grid points.

for magnetic potential:

$$A^3 = \begin{cases} -2.1826182(x - 0.05) & x \leq 0.05, \\ -0.56418958(x - 0.005) & x \geq 0.05, \end{cases}$$

Figure 3.4 presents Schlieren plots of $\|\mathbf{B}\|$ at $t = 0.06$. The new method matches well with our numerical results of our previous method [29].

3.4.4 2D Blast wave

Here we investigate the 2D blast wave test problem, which has a strong shock causing negative density or pressure in simulations. To avoid negative density or pressure, we use

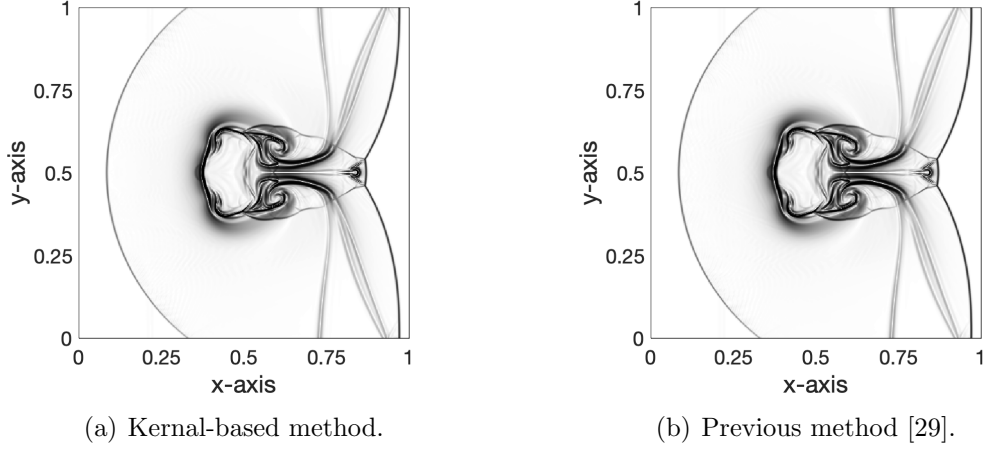


Figure 3.4: Cloud shock problem. Contour plots of $\|\mathbf{B}\|$ at $t = 0.06$ with 512×512 grid points.

the positivity preserving limiter we developed in reference [29]. The initial conditions are

$$(\rho, u^1, u^2, u^3, B^1, B^2, B^3) = (1, 0, 0, 0, 50/\sqrt{2\pi}, 50/\sqrt{2\pi}, 0)$$

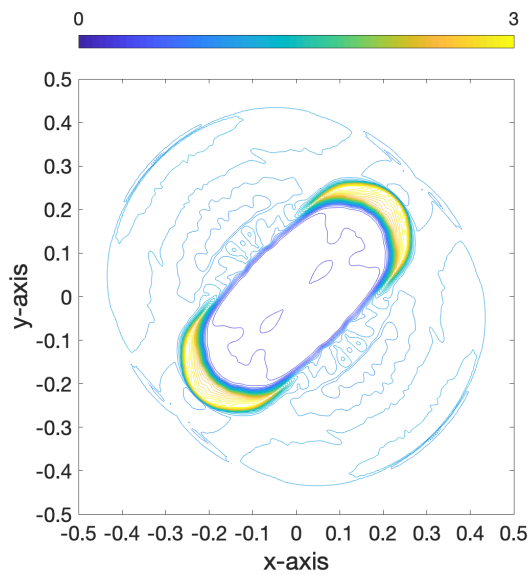
with a spherical pressure pulse

$$p = \begin{cases} 1000 & r \leq 0.1, \\ 0.1 & \text{otherwise.} \end{cases}$$

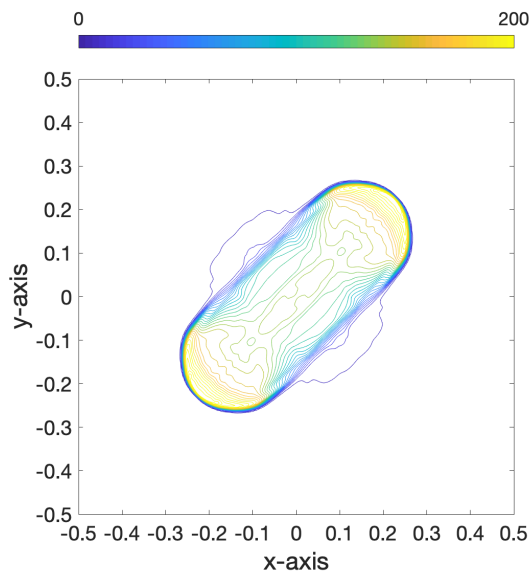
The initial condition for magnetic potential can be obtained as

$$A^3 = (0, 0, 50/\sqrt{2\pi}(y - x)).$$

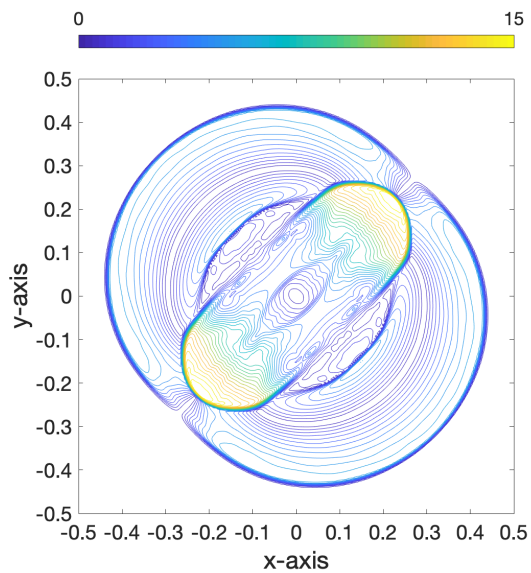
We use a domain $[-0.5, 0.5] \times [-0.5, 0.5]$ with 256×256 mesh. Outflow boundary conditions are applied everywhere. The results are shown in Figure 3.5 and they have good agreement with the results that we got in our previous paper.



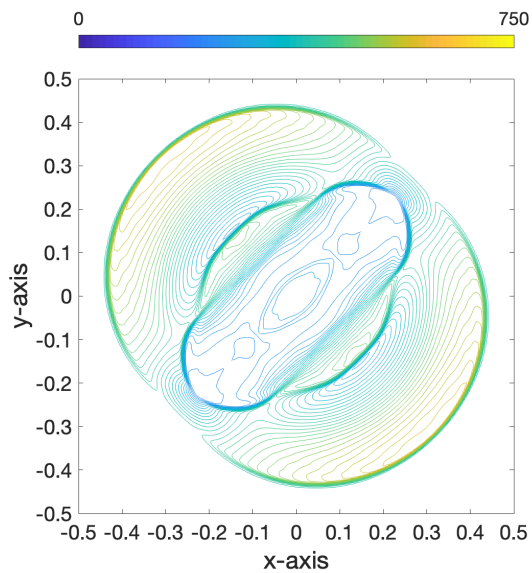
(a) density ρ



(b) pressure p



(c) $\|\mathbf{u}\|$



(d) $\|\mathbf{B}\|$

Figure 3.5: 2D Blast wave problem. Contour plots at time $t = 0.01$ with 256×256 grid points. (a) density; (b) pressure; (c) the norm of \mathbf{u} ; (d) magnetic pressure $\|\mathbf{B}\|$.

3.4.5 2D Field Loop

The field loop problem is a strenuous test problem that moves a steady state. Here we test our recent method on this strenuous test case. The initial conditions are

$$(\rho, u^1, u^2, p) = (1, \sqrt{5} \cos(\theta), \sqrt{5} \sin(\theta), 1)$$

with the angle $\theta = \arctan(0.5)$. The initial conditions for magnetic field \mathbf{B} are determined by taking the curl of the magnetic potential, which is initialized with

$$A^3 = \begin{cases} 0.001(R - r), & r \leq R, \\ 0, & \text{otherwise,} \end{cases}$$

where $r = \sqrt{x^2 + y^2}$ and $R = 0.3$. We use a domain $[-0.5, 0.5] \times [-0.5, 0.5]$ with 128×128 mesh. Periodic boundary conditions are applied to all sides. The loop is started in the middle of the domain and advected around the grid once, returned to initial location at time $t = 1$ as shown in Figure 3.6. We observe that the solution maintains the circular symmetry of the initial condition.

3.4.6 3D Field Loop

We tested an advecting field loop which moved diagonally across the boundary with an arbitrary initial angle. The initial conditions are

$$(\rho, u^1, u^2, u^3, p) = (1, 2/\sqrt{6}, 1/\sqrt{6}, 1/\sqrt{6}, 1)$$

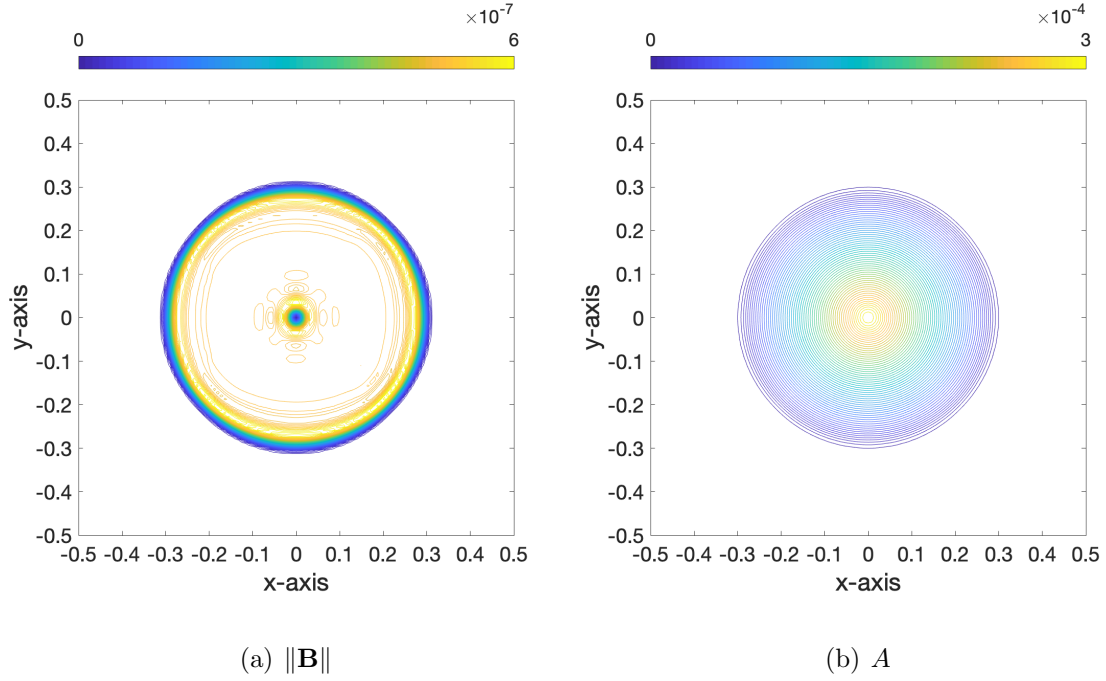


Figure 3.6: 2D Field loop. Contour plots at time $t = 1$ with 128×128 grid points. a) Magnetic Pressure $\|\mathbf{B}\|$; b) Magnetic Potential A^3 .

The initial conditions for magnetic field are determined by taking the curl of the magnetic potential, which is given as magnetic potential :

$$A^3 = \begin{cases} 0.001(R - r) & r \leq R \\ 0 & \text{otherwise,} \end{cases}$$

where $A^1 = 0$, $A^2 = 0$, and $r = \sqrt{x^2 + y^2}$ and $R = 0.3$. We use a domain size $[-0.5, 0.5] \times [-0.5, 0.5] \times [-0.5, 0.5]$ with $128 \times 128 \times 128$ mesh. Periodic boundary conditions are applied to all sides. We observe that the field loop integrity is maintained, after advecting diagonally around the domain, until the final time, $t = 1$. The results shown in Figure 3.7 are a 2D slice of the 3D solution taken at $z = 0$.

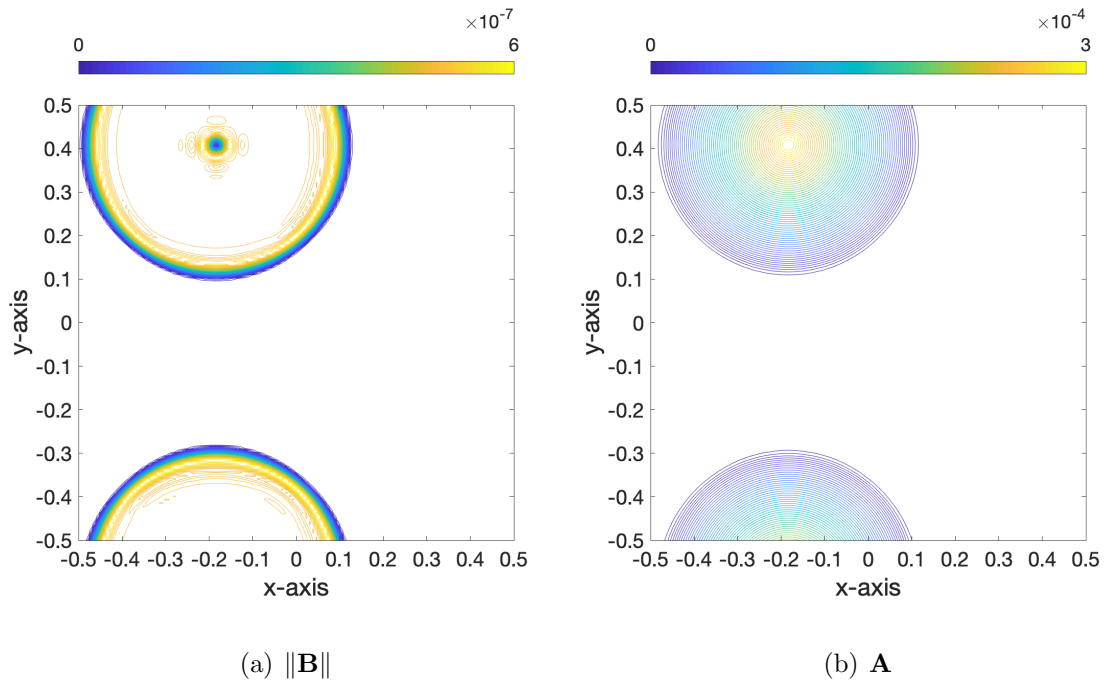


Figure 3.7: 3D Field loop. Contour plots at time $t = 1$ with 128×128 grid points. The loop has been advected around the grid once. a) Magnetic Pressure; b) Magnetic Potential.

3.4.7 3D Blast wave

In this section we investigate the 3D version of the blast wave problem to show the strength of the new method, which eliminating the need for the diffusion limiter. The initial conditions are

$$(\rho, u^1, u^2, u^3, B^1, B^2, B^3) = (1, 0, 0, 0, 50/\sqrt{2\pi}, 50/\sqrt{2\pi}, 0)$$

with a spherical pressure pulse

$$p = \begin{cases} 1000 & r \leq 0.1 \\ 0.1 & \text{otherwise.} \end{cases}$$

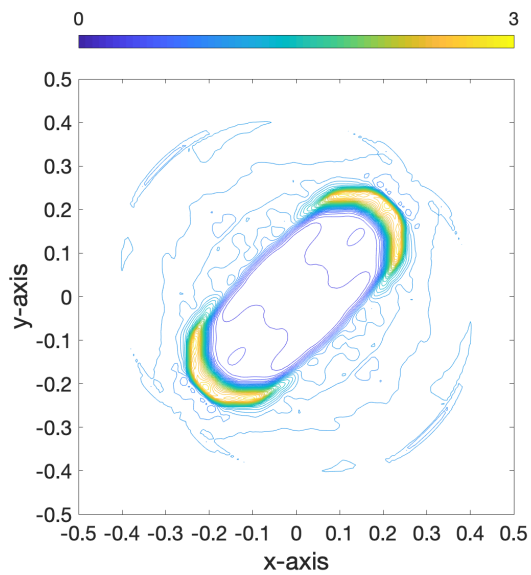
where $r = \sqrt{x^2 + y^2 + z^2}$. The initial condition for magnetic potential :

$$\mathbf{A}(0, x, y, z) = (0, 0, 50/\sqrt{2\pi}y - 50/\sqrt{2\pi}x).$$

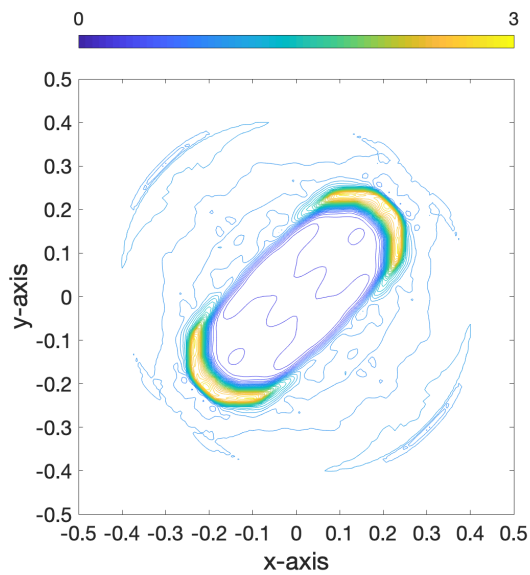
We use a domain size $[-0.5, 0.5] \times [-0.5, 0.5] \times [-0.5, 0.5]$ with $150 \times 150 \times 150$ mesh. Outflow boundary conditions are applied everywhere. The results presented in Figure 3.8 and Figure 3.9 are the solutions cut at $z = 0$. The sub plots highlight the differences between the two methods. The key differences are the new method has a maximum value that achieves a peak of 320, which is 23% higher than the old method, and is far less isotropic around the peak than the old method. As demonstrated in a latter test, the isotropic behavior and lower the peak in the strong blast wave is due to the diffusion limiter that was needed with the old explicit constrained transport method.

3.4.8 Kernel-based method with Diffusion Terms

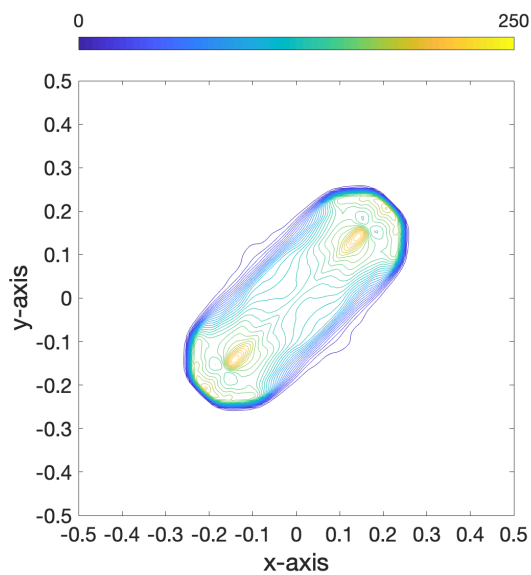
In this section we demonstrate the advantage of the new approach in the context of strong shocks. In the previous approach [29], we needed to add in a diffusion limiter to stabilize the update for \mathbf{A} in the vicinity of a sharp change in the solution. This had no impact on smooth solutions, and minimal impact on problems like the cloud shock. But in the context of the blast wave problem, while the diffusion limiter stabilized the solution, comparing $\|\mathbf{u}\|$ for both schemes, we have the max value of the previous method is 261, while it is 320 for the kernel-based method. This involved decreasing the maximum values, making the solution more isotropic, and changing the structure of the contours away from the blast. In Figure 3.10, we show the solution generated by the new method with the diffusion limiter used in our previous code. In this case, the max value of $\|\mathbf{u}\|$ is 265. These results confirm that the



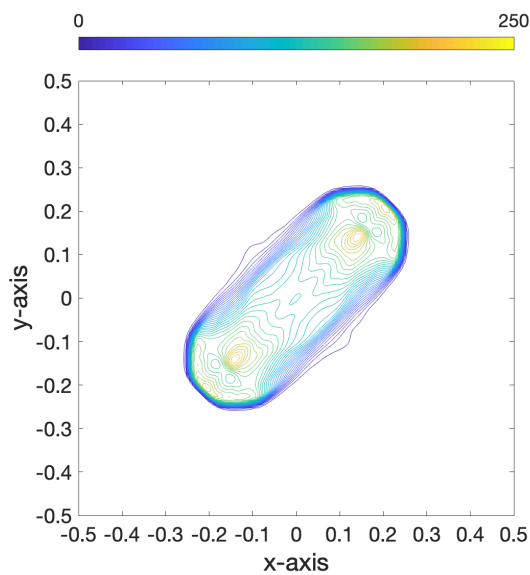
(a) density with kernel-based method



(b) density with previous method [29].

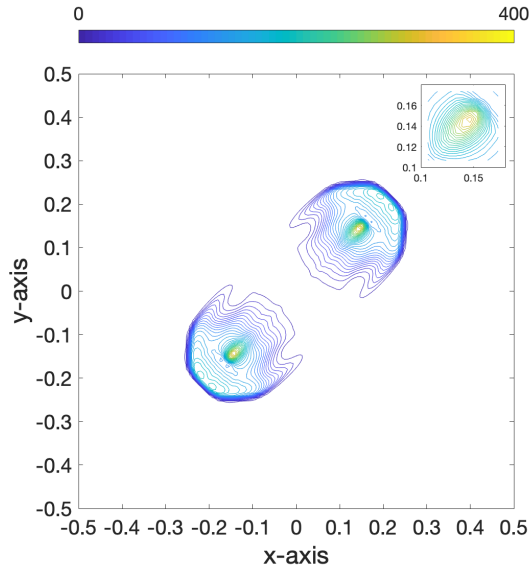


(c) pressure with kernel-based method

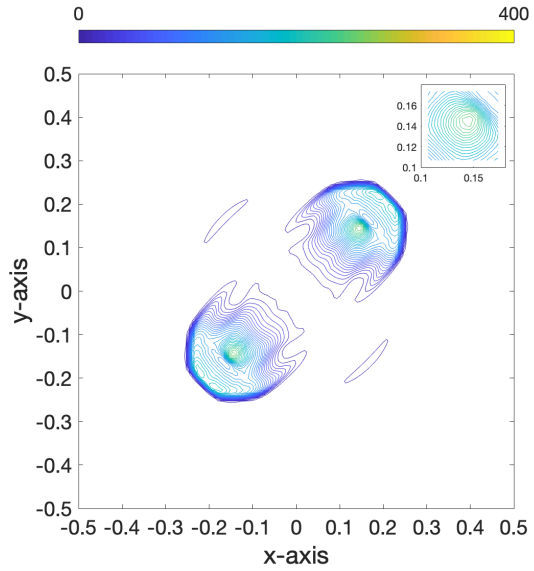


(d) pressure with previous method [29]

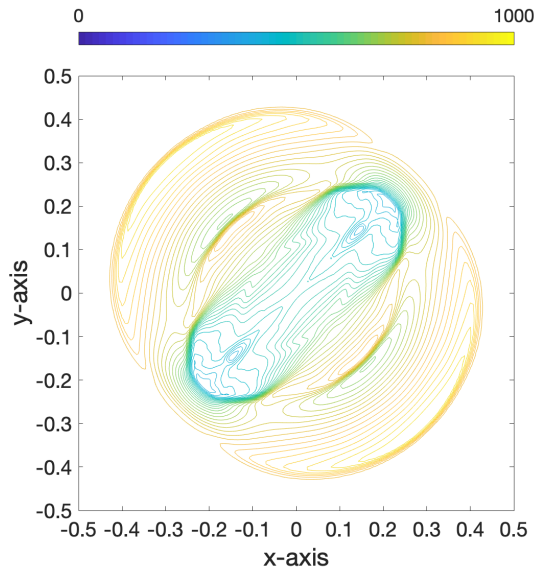
Figure 3.8: 3D Blast wave problem. Contour plots at time $t = 0.01$ with 150×150 grid points



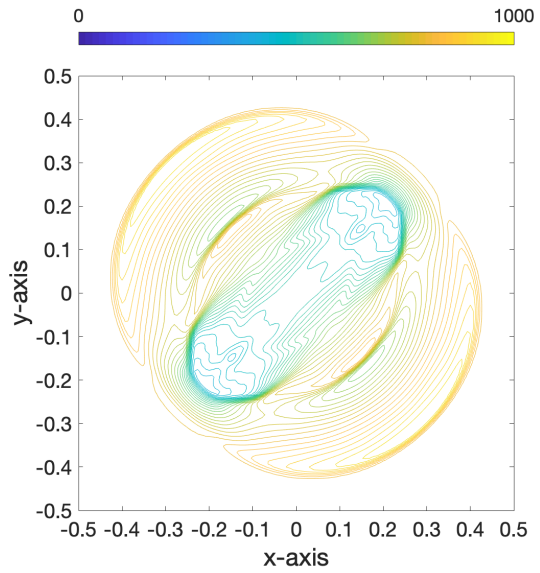
(a) $\|\mathbf{u}\|$ with kernel-based method



(b) $\|\mathbf{u}\|$ with previous method [29]



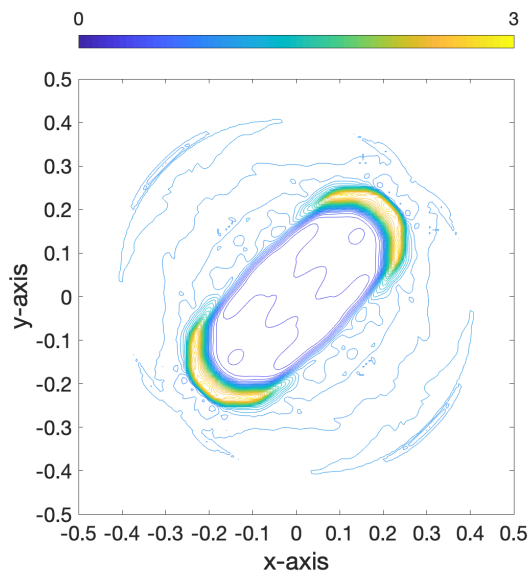
(c) $\|\mathbf{B}\|$ with kernel-based method



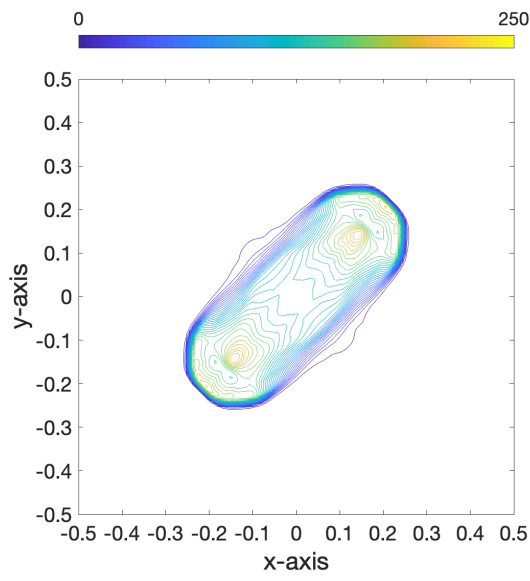
(d) $\|\mathbf{B}\|$ with previous method [29]

Figure 3.9: 3D Blast wave problem. Contour plots at time $t = 0.01$ with 150×150 grid points. While the max $\|\mathbf{u}\|$ value for previous method is 261, it is 320 for the kernel-based method. Note that this is 23% higher than the old method, and is far less isotropic around the peak than the old method

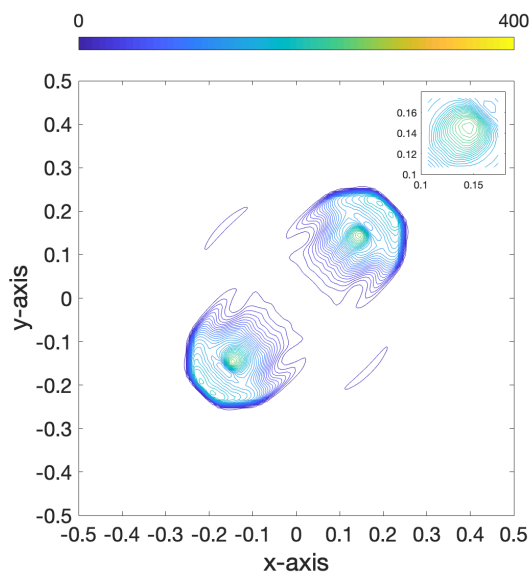
limiter is what is causing a change in the solution structure for problems with strong shocks. Adding the diffusion limiter caused the solution to revert from the results of the new method to those obtained by the old method.



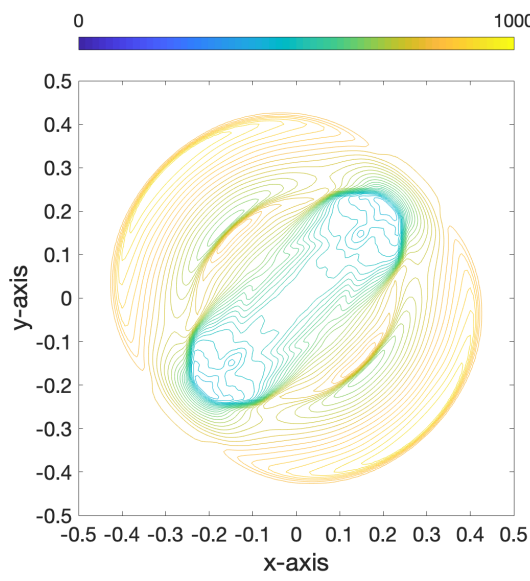
(a) density



(b) pressure



(c) $\|\mathbf{u}\|$



(d) $\|\mathbf{B}\|$

Figure 3.10: 3D Blast wave from the kernel based method with having added the diffusion limiter. The max $\|\mathbf{u}\|$ value is 265. We note that these results are nearly identical to the old WENO-HJ method, which required the diffusion limiter.

Chapter 4

MOLT for PEC for ideal MHD

In this chapter we expand our proposed scheme to work for perfectly electrically conducting (PEC) boundary conditions. We develop PEC boundary conditions for magnetic potential in MOLT-HJ scheme. Then, we go over the derivation of a key test problem called the Hartmann Flow problem and demonstrate the new method on this test problem.

4.1 MOLT for PEC for ideal MHD

We have seen in the previous chapters that our kernel based approximation is working well for the periodic and outflow boundary conditions. In this section, we will explain the numerical boundary condition for bounded domains in ideal MHD. We will define the perfectly electrically conducting (PEC) boundary conditions for the conserved variables and the magnetic potential. In particular, we will derive these boundary conditions in the context of MOLT and show that it is equivalent to enforcing Dirichlet conditions.

Following the ideas in [25], we can define the PEC boundary condition. Let's assume that the PEC boundary exists at $\xi = \xi_0$. Then on a PEC boundary, we have the following conditions,

$$u_1(\xi_0, \eta, t) = 0, \tag{4.1.1}$$

$$B_1(\xi_0, \eta, t) = 0. \tag{4.1.2}$$

According to the local characteristics analysis, forward fast magnetosonic waves is moving into the domain, while backward fast magnetosonic waves is exiting the domain. Remaining characteristics are shown to propagate along the boundary. Note that the PEC boundary condition on the magnetic field (4.1.2) guarantees that the remaining four characteristics, Alfvén and slow magnetosonic waves, are moving along the boundary. Thus, these PEC boundary conditions are consistent with the analysis of local characteristic. A numerical implementation of these boundary conditions requires a careful treatment, as many characteristics are moving parallel to the boundary.

We will describe the analytic boundary condition for the magnetic potential A in the constrained transport method before discussing the numerical boundary conditions. The PEC boundary condition for magnetic field (4.1.2) at the boundary $\xi = \xi_0$ satisfies the following relation

$$\begin{aligned}
 B_1 &= \partial_x \xi \partial_y A - \partial_y \xi \partial_x A, \\
 &= (\partial_x \xi \partial_y \eta - \partial_x \eta \partial_y \xi) \partial_\eta A, \\
 &= 0,
 \end{aligned}
 \tag{4.1.3}$$

which gives that

$$\partial_\eta A = 0.
 \tag{4.1.4}$$

Hence, the magnetic potential equation at the boundary satisfies

$$\partial_t A + (u_1 \partial_x \xi + u_2 \partial_y \xi) \partial_\xi A = 0.
 \tag{4.1.5}$$

Also, due to the velocity boundary condition (4.1.1), along with $(u_1 \partial_x \xi + u_2 \partial_y \xi) \partial_\xi = \nabla_x \xi \cdot \mathbf{u}$,

we obtain the analytical boundary condition for the magnetic potential as

$$A(\xi_0, \eta, t) = A^0, \quad (4.1.6)$$

where A^0 is some constant number that is given in the initial condition.

A Dirichlet boundary condition is applied to the magnetic potential

$$A_i = A^0, \quad \text{on } i = 0. \quad (4.1.7)$$

Note that values at the ghost points are approximated, here, by using extrapolation of sufficiently high order. More details can be found in [25].

4.1.1 Derivation of the Boundary Conditions for MOLT for Dirichlet BC

In the previous section, we showed that the PEC boundary condition is equivalent to enforcing a Dirichlet boundary condition on the magnetic vector potential. Our next task is to connect this to the MOLT scheme using a simple example.

$$\partial_t v - c \partial_x v = 0, \quad (4.1.8)$$

we define the operator \mathcal{L}_R as

$$\mathcal{L}_R = \mathcal{I} - \frac{1}{\alpha} \partial_x, \quad (4.1.9)$$

where $\alpha = \frac{\beta}{c\Delta t}$. For the Backward Euler time discretization, we obtain

$$\frac{v^{n+1} - v^n}{\Delta t} - c\partial_x v^{n+1} = 0, \quad (4.1.10)$$

where t^n is the current time level and t^{n+1} is the new time step. Then,

$$(v^{n+1} - v^n) - c\Delta t\partial_x v^{n+1} = 0, \quad (4.1.11)$$

then if we rearrange terms, we obtain the semi-discrete equation

$$(1 - c\Delta t\partial_x)v^{n+1} = v^n, \quad (4.1.12)$$

which can be compactly stated as

$$\mathcal{L}_R v^{n+1} = v^n. \quad (4.1.13)$$

We can then solve this equation by applying the integrating factor method. With the aid of equation (4.1.13), we find that

$$\begin{aligned} \partial_x(e^{-\alpha x} v^{n+1}(x)) &= -\alpha e^{-\alpha x} v^{n+1}(x) + e^{-\alpha x} \partial_x v^{n+1}(x), \\ &= -\alpha e^{-\alpha x} (v^{n+1}(x) - \frac{1}{\alpha} \partial_x v^{n+1}(x)), \\ &= -\alpha e^{-\alpha x} v^n(x). \end{aligned} \quad (4.1.14)$$

We integrate the relation (4.1.14) from x to b , which result in

$$\int_x^b \partial_x(e^{-\alpha y} v^{n+1}(y)) dy = -\alpha \int_x^b e^{-\alpha y} v^n(y) dy, \quad (4.1.15)$$

after which, we see that

$$e^{-\alpha b}v^{n+1}(b) - e^{-\alpha x}v^{n+1}(x) = -\alpha \int_x^b e^{-\alpha y}v^n(y)dy. \quad (4.1.16)$$

If we rewrite this equation to solve for v^{n+1} , we obtain the formula

$$v^{n+1}(x) = \alpha \int_x^b e^{-\alpha(y-x)}v^n(y)dy + e^{-\alpha(b-x)}v^{n+1}(b). \quad (4.1.17)$$

In the above, we use the definitions

$$I^R[v^n](x) = \alpha \int_x^b e^{-\alpha(y-x)}v^n(y)dy \quad \text{and} \quad B_R = v^{n+1}(b). \quad (4.1.18)$$

The equation (4.1.17) is actually $v^{n+1}(x) = \mathcal{L}_R^{-1}[v^n](x)$ and we need \mathcal{L}_R^{-1} in our infinite series of \mathcal{D}_R , which is defined as $\mathcal{D}_R = \mathcal{I} - \mathcal{L}_R^{-1}$. Remember that we use the infinite series of \mathcal{D}_R to approximate the first order derivative term as follow in short

$$\partial_x = -\alpha \sum \mathcal{D}_R^p. \quad (4.1.19)$$

Now we show how to approximate the boundary term B_R using a Taylor expansion. For non-linear problems, we have observed that using linear operators results in inconsistencies at the boundaries. Using a Taylor expansion around the previous time level's data allows us to correct this issue. Applying Taylor expansion on v^{n+1} gives

$$B_R := v^{n+1}(b) = v^n(b) + \Delta t v_t^n(b) + \dots \quad (4.1.20)$$

Employing Cauchy-Kowalevski theorem and equation (4.1.8), we have

$$v_t^n = cv_x^n + \mathcal{O}(\Delta x^2), \quad (4.1.21)$$

hence equation (4.1.20) becomes

$$B_R = v^n(b) + c\Delta t v_x^n(b) + \mathcal{O}(\Delta x^2 \Delta t), \quad (4.1.22)$$

$$= v^n(b) + \frac{1}{\alpha} v_x^n(b).$$

In the next section, we describe a well-known benchmark problem, called Hartmann Flow, to test our formulation of PEC boundary conditions in the MOLT using the above correction.

4.2 Hartmann Flow

In general, the non-linearity of the MHD equations makes it difficult to write analytical solutions. However, there is a restricted version of MHD model where non-linear terms of MHD equations are excluded. For this special case of the MHD model, with the aid of stationary conditions, it is possible to obtain a steady-state analytical solution. One such example of this is the so-called Hartmann Flow problem, in which the flow is taken to be incompressible. The importance of this test problem is that it allows us to assess the capabilities of our code for both restrictive and ideal MHD models with PEC boundary conditions. Even though the model for Hartmann Flow includes diffusion terms, we can ignore them to test the PEC boundaries in ideal MHD. Here, we provide a brief derivation

of the Hartmann Flow problem, which includes the diffusion terms.

We will start with the MHD equations and end up with the Hartmann Flow. Since the model for MHD is taken to be incompressible,

$$\nabla \cdot \mathbf{v} = 0. \quad (4.2.1)$$

Further, in Hartmann flow, $\rho = 1$ in the domain as well as $p = 1$. Additionally, the momentum and magnetic field equations are given as

$$\rho \left[\frac{\partial \mathbf{v}}{\partial t} + (\mathbf{v} \cdot \nabla) \mathbf{v} \right] = -\nabla p + \mathbf{f} + N(\mathbf{j} \times \mathbf{B}) + \frac{1}{R} \nabla^2 \mathbf{v} \quad (4.2.2)$$

$$\frac{\partial \mathbf{B}}{\partial t} + (\mathbf{v} \cdot \nabla) \mathbf{B} = (\mathbf{B} \cdot \nabla) \mathbf{v} + \frac{1}{Rm} \nabla^2 \mathbf{B} \quad (4.2.3)$$

where the last term at the right hand side of the equation (4.2.3) represents magnetic diffusion. With the assumptions of linearity in equations (4.2.2) and (4.2.3), we have that $\mathbf{v} = v_x(y) \hat{\mathbf{x}}$ and $\mathbf{B} = \hat{\mathbf{y}} + \frac{Rm}{Ha} B_x(y) \hat{\mathbf{x}}$, where the subscript x denotes the x-component of the velocity and magnetic field, respectively. Note that, these components are functions of a single variable y only.

The geometry of the problem consists of two infinite parallel plates and there is flow in the gap between the plates. The externally applied magnetic field is perpendicular to the parallel plates, and there is no boundary at the x direction. Because of the stationary condition and the assumptions above, left hand side of equation (4.2.3) is identically zero. Thus, the induction equation simplifies to

$$\frac{\partial^2 B_x}{\partial y^2} + Ha \frac{\partial v_x}{\partial y} = 0. \quad (4.2.4)$$

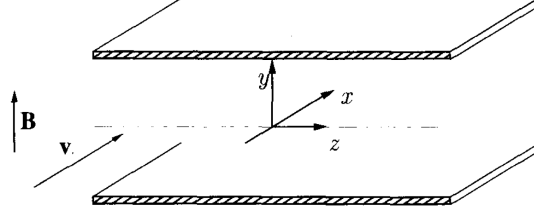


Figure 4.1: Sketch of a Hartmann type of flow [58].

One can also verify that, under these assumptions, the left hand side of the momentum equation (4.2.2) vanishes. Terms on the right hand side can be multiplied by R so that the magnitude of the gradient of the uniform pressure becomes unity. Also, the Ampere's law gives a relation between the induced magnetic field and the current density

$$\mathbf{j} = \frac{1}{Ha} \nabla \times B_x \hat{\mathbf{x}} = \frac{1}{Ha} \frac{-\partial B_x}{\partial y} \hat{\mathbf{z}}, \quad (4.2.5)$$

so that the Lorenz force $\mathbf{j} \times \mathbf{B}$ can be given with respect to B_x . Therefore, the momentum equation simplifies to

$$\frac{\partial^2 v_x}{\partial y^2} + Ha \frac{\partial B_x}{\partial y} = -1. \quad (4.2.6)$$

Thus, we obtain the Hartman flow problem,

$$\frac{\partial^2 v_x}{\partial y^2} + Ha \frac{\partial B_x}{\partial y} = -1, \quad (4.2.7)$$

$$\frac{\partial^2 B_x}{\partial y^2} + Ha \frac{\partial v_x}{\partial y} = 0, \quad -1 < y < 1, \quad (4.2.8)$$

and

$$v_x = 0, \quad \pm \frac{\partial B_x}{\partial y} = 0, \quad \text{at } y = \pm 1, \quad (4.2.9)$$

where the walls are perfectly conducting. The analytic solutions of the equations above can be found as

$$v_x(y) = \frac{-1}{Ha^2 \cosh(Ha)} \left(\cosh(Ha y) - \cosh(Ha) \right) \quad (4.2.10)$$

$$B_x(y) = \frac{-y}{Ha} + \frac{1}{Ha^2} \frac{\sinh(Ha y)}{\cosh(Ha)} \quad (4.2.11)$$

More details can be found in [58]. Moreover, we can derive the magnetic potential equation in 2D as

$$A = \frac{-y^2}{2Ha} + \frac{1}{Ha^3} \frac{\cosh(Ha y)}{\cosh(Ha)}. \quad (4.2.12)$$

4.2.1 Numerical Results for ideal MHD with PEC Boundary Conditions

A refinement study is done for the Hartmann Flow problem for the ideal MHD, where the diffusion effect is zero, $\eta = 0$ and the Hartmann number is $Ha = 10$. We use a CFL number of 0.5 and $\beta = 0.8$. In Table (4.1), we obtained high order accuracy for magnetic field, in the case of ideal MHD with PEC boundary conditions.

Table 4.1: Hartmann Flow for ideal MHD. Errors of B and orders of accuracy.

| $N_x \times N_y$ | L_1 error | order | L_∞ error | order |
|------------------|-------------|-------|------------------|-------|
| 64×64 | 9.6462E-007 | – | 5.3007E-006 | – |
| 128×128 | 7.2391E-008 | 3.74 | 7.9204E-007 | 2.74 |
| 256×256 | 4.9457E-009 | 3.87 | 1.0718E-007 | 2.89 |
| 512×512 | 3.2161E-010 | 3.94 | 1.1407E-008 | 3.23 |

In Figure 4.2, we have 1D cross-sections of the magnetic potential A and the induced magnetic field B_x for the resolution 128×128 and the final time $t = 1$. We see that exact solutions overlap the numerical results.

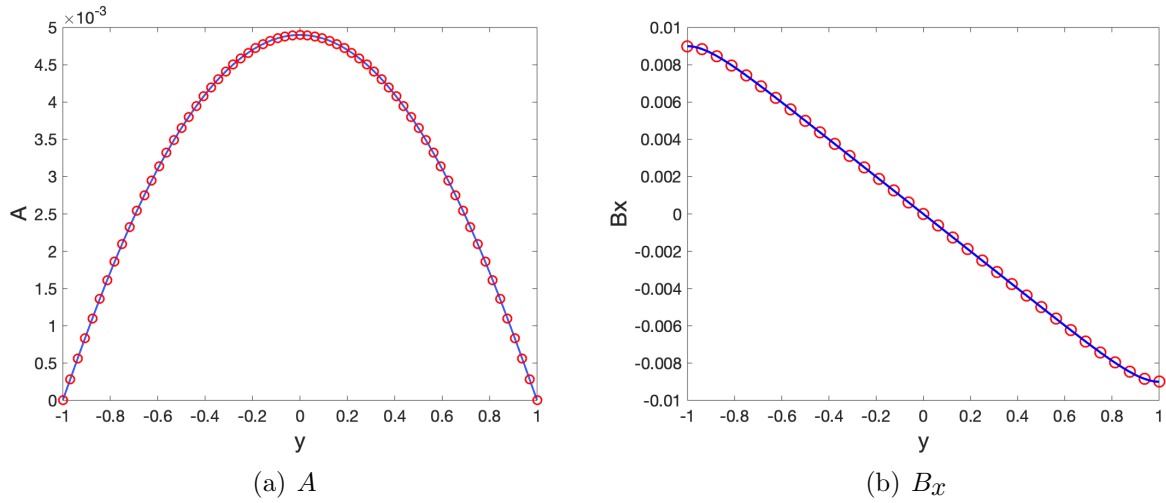


Figure 4.2: 1D cross-sections of Hartmann problem for $Ha = 10$ at $t = 1$ with 128×128 .

In Figures 4.3, 4.4, 4.5, we have 2D contour plots of exact and numerical results of u_x , B_x , and A , respectively. The numerical results have good agreement with the exact solutions.

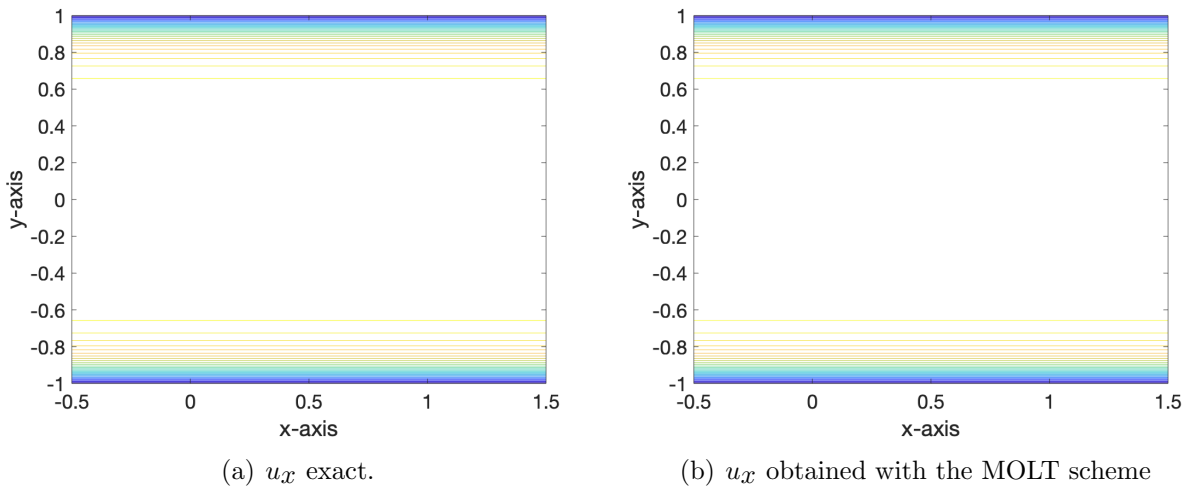
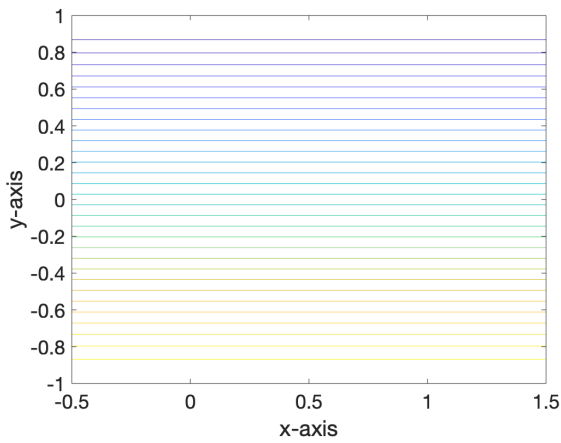
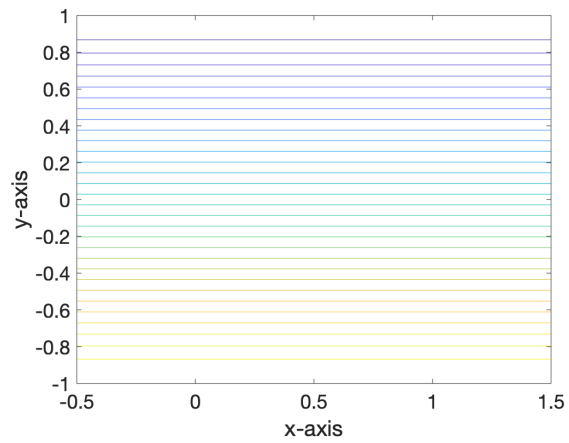


Figure 4.3: Velocity profile for the Hartmann problem for $Ha = 10$ in 2D at $t = 1$ with 128×128 .

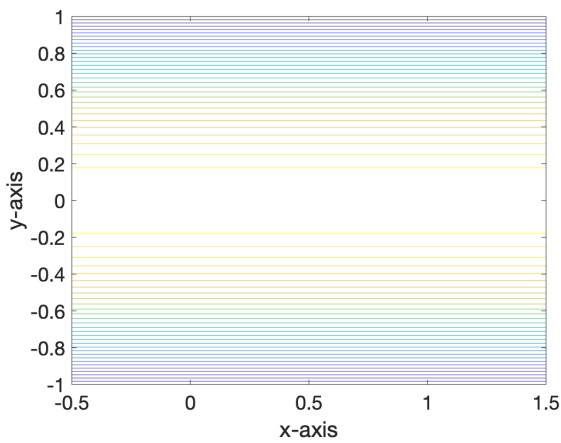


(a) B_x exact solution.

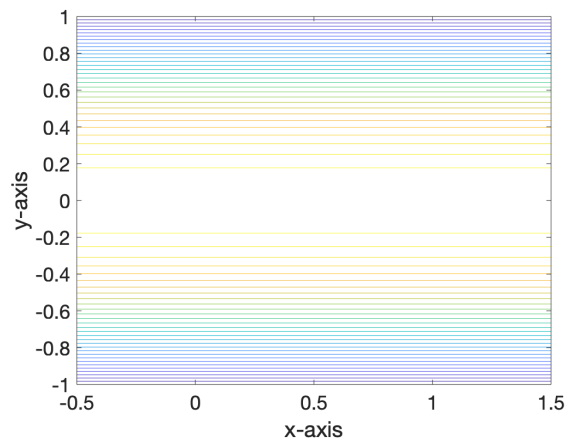


(b) B_x obtained with the MOLT scheme

Figure 4.4: Induced magnetic field for the Hartmann problem for $Ha = 10$ at $t = 1$ with 128×128 .



(a) A exact solution.



(b) A obtained with the MOLT scheme

Figure 4.5: Magnetic potential A for the Hartmann problem at $Ha = 10$.

Chapter 5

Non-Ideal MHD Equations

5.1 NON- IDEAL MHD

In this chapter we will describe the non-ideal MHD equations. The structure of this system is similar to that of the ideal case, with the difference being the introduction of certain terms in the equation for the magnetic field. These terms, which come from a generalized form of Ohm's law, result in the collection of equations given by

$$\partial_t \begin{bmatrix} \rho \\ \rho \mathbf{u} \\ \mathcal{E} \\ \mathbf{B} \end{bmatrix} + \nabla \cdot \begin{bmatrix} \rho \mathbf{u} \\ \rho \mathbf{u} \otimes \mathbf{u} + p_{\text{tot}} \mathbb{I} - \mathbf{B} \otimes \mathbf{B} \\ \mathbf{u}(\mathcal{E} + p_{\text{tot}}) - \mathbf{B}(\mathbf{u} \cdot \mathbf{B}) \\ \mathbf{u} \otimes \mathbf{B} - \mathbf{B} \otimes \mathbf{u} \end{bmatrix} = \begin{bmatrix} 0 \\ 0 \\ 0 \\ \nabla \times (\eta \mathbf{J} + \frac{1}{ne} \mathbf{J} \times \mathbf{B}) \end{bmatrix}, \quad (5.1.1)$$

$$\nabla \cdot \mathbf{B} = 0, \quad (5.1.2)$$

with the equation of state as

$$\mathcal{E} = \frac{p}{\gamma - 1} + \frac{\rho \|\mathbf{u}\|^2}{2} + \frac{\|\mathbf{B}\|^2}{2}.$$

Here, $\eta\mathbf{J}$ is commonly referred to as the resistive term, while $\frac{1}{ne}\mathbf{J} \times \mathbf{B}$ is known as the Hall term. In this work, we focus on the resistive form of MHD, leaving the Hall term as part of future work.

Compared with plasmas modeled with ideal MHD, there is no "frozen-in" condition for the resistive MHD model. This condition can be explained as follows: if some particles of the plasma are attached by a magnetic field line at one time, they will stay attached by a magnetic field line at future times and the magnetic topology of plasma is preserved. In other words, the magnetic field and the plasma move together once we have this condition. The frozen-in condition is valid when the following conditions are satisfied:

$$\text{The ideal Ohm's law : } \quad \mathbf{E} + \frac{\mathbf{u} \times \mathbf{B}}{c} = 0, \quad (5.1.3)$$

$$\text{Faraday's law : } \quad \frac{\partial \mathbf{B}}{\partial t} = -\nabla \times \mathbf{E}. \quad (5.1.4)$$

However, the resistive Ohm's law is

$$\mathbf{E} + \frac{\mathbf{u} \times \mathbf{B}}{c} = \eta\mathbf{J}, \quad (5.1.5)$$

As will be derived in the next section, under equation 5.1.5, the field equation becomes which doesn't satisfy the frozen-in condition.

$$\frac{\partial \mathbf{B}}{\partial t} = \nabla \times (\mathbf{u} \times \mathbf{B}) + c\eta\nabla^2\mathbf{B}, \quad (5.1.6)$$

where $c\eta\nabla^2\mathbf{B}$ is the diffusion term. Thus the magnetic topology of the resistive MHD is changing with the effect of resistivity since there is no "frozen-in" condition anymore and it

leads to a "reconnection" of different magnetic field lines, which is an important effect in the macroscopic processes of MHD plasmas. Magnetic field lines reconnection happens in a very thin layer in which the resistivity effect cannot be neglected since the parallel electric field locally vanishes. The main goal of this work will be analyzing this important phenomenon.

Our approach to solve the resistive MHD system is through the magnetic potential equation derived from the magnetic induction equation for resistive MHD. The derivation of the magnetic potential equation is given in the next section.

5.2 Magnetic Vector Potential Formulation for Resistive MHD

In this section we will derive the magnetic potential equation for the resistive MHD model. The resulting equations will be the dominant part for our constrained transport method for resistive MHD.

Let's write down Generalized Ohm's Law for MHD [12, 60],

$$\mathbf{E} + \frac{\mathbf{u} \times \mathbf{B}}{c} = \eta \mathbf{J} + \frac{\mathbf{J} \times \mathbf{B}}{en_e c} - \frac{\nabla \cdot \mathbf{P}_e}{n_e e c} + \frac{m_e}{n_e e^2} \frac{d\mathbf{J}}{dt}, \quad (5.2.1)$$

where η is the collision frequency. In deriving the resistive model, we shall keep only the first term on the right hand side of the equation (5.2.1), i.e.,

$$\mathbf{E} + \frac{\mathbf{u} \times \mathbf{B}}{c} = \eta \mathbf{J}. \quad (5.2.2)$$

Let's recall the Maxwell's equations

$$\frac{1}{c^2} \partial_t \mathbf{E} = -\eta_0 \mathbf{J} + \nabla \times \mathbf{B}, \quad (5.2.3)$$

$$\partial_t \mathbf{B} = -\nabla \times \mathbf{E}, \quad (5.2.4)$$

with involutions

$$\nabla \cdot \mathbf{B} = 0, \quad (5.2.5)$$

$$\nabla \cdot \mathbf{E} = -\frac{\rho}{\epsilon_0}. \quad (5.2.6)$$

We also know that

$$\mathbf{B} = \nabla \times \mathbf{A}, \quad (5.2.7)$$

$$\frac{1}{c^2} \partial_t \mathbf{E} = 0 \quad (5.2.8)$$

in MHD. Then, using (5.2.4) and (5.2.7) we obtain

$$\nabla \times \partial_t \mathbf{A} = -\nabla \times \mathbf{E} \quad (5.2.9)$$

$$\Rightarrow \quad \nabla \times [\partial_t \mathbf{A} = -\mathbf{E}]. \quad (5.2.10)$$

The relation (5.2.10) implies the existence of a scalar function ψ such that

$$\partial_t \mathbf{A} = -\mathbf{E} + \nabla \psi. \quad (5.2.11)$$

Moreover, if we apply the curl operator to the final term of the (5.2.11), we will get $\nabla \times \nabla \psi = 0$. Note that the function ψ is a gauge function, which is a degree of the freedom. Here, we

make use of the Weyl gauge, $\psi = 0$ [42]. Hence (5.2.11) becomes

$$\partial_t \mathbf{A} = -\mathbf{E}. \quad (5.2.12)$$

Using the equation (5.2.2) into (5.2.13), we get

$$\partial_t \mathbf{A} = -\left[\frac{-\mathbf{u} \times \mathbf{B}}{c} + \eta \mathbf{J}\right], \quad (5.2.13)$$

Because of the (5.2.8) and the (5.2.3), we get

$$\mathbf{J} = \frac{1}{\eta_0} \nabla \times \mathbf{B}. \quad (5.2.14)$$

Using (5.2.7) into (5.2.14), we get

$$\mathbf{J} = \frac{1}{\eta_0} \nabla \times (\nabla \times \mathbf{A}). \quad (5.2.15)$$

Using the Grassmann identity, $a \times (b \times c) = (a \cdot c)b - (a \cdot b)c = b(a \cdot c) - (a \cdot b)c$, we obtain

$$\mathbf{J} = \frac{1}{\eta_0} [\nabla(\nabla \cdot \mathbf{A}) - (\nabla \cdot \nabla)\mathbf{A}]. \quad (5.2.16)$$

Equation (5.2.16) can be rewritten as

$$\mathbf{J} = \frac{1}{\eta_0} \begin{bmatrix} \partial_{xy}A^2 + \partial_{xz}A^3 - \partial_{yy}A^1 - \partial_{zz}A^1 \\ \partial_{xy}A^1 + \partial_{yz}A^3 - \partial_{xx}A^2 - \partial_{zz}A^2 \\ \partial_{xz}A^1 + \partial_{yz}A^2 - \partial_{xx}A^3 - \partial_{yy}A^3 \end{bmatrix}. \quad (5.2.17)$$

Now we need to get $\mathbf{u} \times \mathbf{B}$ to complete the equation (5.2.13). So,

$$\mathbf{u} \times (\nabla \times \mathbf{A}) = \begin{bmatrix} (u^2(\partial_x A^2 - \partial_y A^1) - u^3(\partial_z A^1 - \partial_x A^3)) \\ (u^3(\partial_y A^3 - \partial_z A^2) - u^1(\partial_x A^2 - \partial_y A^1)) \\ (u^1(\partial_z A^1 - \partial_x A^3) - u^2(\partial_y A^3 - \partial_z A^2)) \end{bmatrix} \quad (5.2.18)$$

Then combining (5.2.17) and (5.2.18) will give the equation (5.2.13) in component-wise as

$$\frac{\partial A^1}{\partial t} = \frac{1}{c} [u^2 \partial_x A^2 + u^3 \partial_x A^3 - u^2 \partial_y A^1 - u^3 \partial_z A^1] - \frac{\eta}{\eta_0} [\partial_{xy} A^2 + \partial_{xz} A^3 - \partial_{yy} A^1 - \partial_{zz} A^1] \quad (5.2.19)$$

$$\frac{\partial A^2}{\partial t} = \frac{1}{c} [u^3 \partial_y A^3 + u^1 \partial_y A^1 - u^3 \partial_z A^2 - u^1 \partial_x A^2] - \frac{\eta}{\eta_0} [\partial_{xy} A^1 + \partial_{yz} A^3 - \partial_{xx} A^2 - \partial_{zz} A^2] \quad (5.2.20)$$

$$\frac{\partial A^3}{\partial t} = \frac{1}{c} [u^1 \partial_z A^1 + u^2 \partial_z A^2 - u^1 \partial_x A^3 - u^2 \partial_y A^3] - \frac{\eta}{\eta_0} [\partial_{xz} A^1 + \partial_{yz} A^1 - \partial_{xx} A^3 - \partial_{yy} A^3] \quad (5.2.21)$$

The resulting system for magnetic vector potential equation becomes a system of Hamilton-Jacobi equations with diffusion terms since the velocity variables are given from the previous time step. The approximation used for the Hamilton-Jacobi terms was studied in Chapter-3, in which we applied the MOLT. In the next chapter, we discuss the approximations used for the second order derivative terms. Note that in 2D, $\mathbf{A} = (0, 0, A^3)$, so the system (5.2.19) - (5.2.21) reduces to a single Hamilton-Jacobi equation with diffusion equation given by

$$\frac{\partial A^3}{\partial t} = \frac{1}{c} [-u^1 \partial_x A^3 - u^2 \partial_y A^3] - \frac{\eta}{\eta_0} [-\partial_{xx} A^3 - \partial_{yy} A^3] \quad (5.2.22)$$

In this work we focus on the 2D resistive MHD system, so we will use the scalar equation

for the magnetic potential.

5.3 Outline for Constrained Transport Framework for Non-ideal MHD

In this section, we provide an outline of the steps used to solve the 2D non-ideal MHD system using our constrained transport methodology. The basic idea of constrained transport (CT) for non-ideal MHD is similar to the one used for ideal MHD. The approach begins by updating the conserved variables $\mathbf{q} = (\rho, \rho\mathbf{u}, \mathcal{E}, \mathbf{B})$ using a standard HCL-WENO scheme. Then, the updated magnetic field is replaced with a discrete curl of the magnetic potential. The importance of the last step is that it automatically maintains the divergence free condition on the magnetic field. Here, we provide the important steps of the CT methodology to advance the solution from current time step $t = t^n$ to the new time step t^{n+1} .

Because we are using explicit time stepping, the values in the update only depend on the old data in each of the stages of an RK method. We start by considering a single Euler step. The values of \mathbf{B} at level t^n are all that are needed for the update of the energy and momentum. Hence, our proposed method is to update the variables using ideal MHD, followed by correcting \mathbf{B} at time t^{n+1} with the non-ideal solution to \mathbf{A} at t^{n+1} . This avoids the still CFL restrictions of having a diffusion term on the right hand side of \mathbf{B} when doing the update. This has to be done in the stage values in RK.

Consider a semi-discrete system of ordinary differential equations for ideal MHD equations (2.1.1)

$$\mathbf{q}'_{mhd}(t) = \mathcal{L}(\mathbf{q}_{mhd}(t)) \tag{5.3.1}$$

where $\mathbf{q}_{mhd}(t)$ represents the grid function at time t consisting of all point-wise values of the conserved quantities in the ideal MHD system $\mathbf{q}_{mhd} = (\rho, \rho\mathbf{u}, \mathcal{E}, \mathbf{B})$. The details about $\mathcal{L}(\mathbf{q}_{mhd}(t))$ were presented in [29]. Next, note that the evolution equation for the magnetic potential in 2D is of the form

$$\mathbf{q}'_A(t) = \mathcal{H}(\mathbf{q}_A(t), \mathbf{u}(t)) + \mathcal{G}(\mathbf{q}_A(t)), \quad (5.3.2)$$

where \mathbf{q}_A denotes the magnetic scalar potential, A^3 , in 2D, and \mathcal{G} is the diffusion part of the equation which involves second order derivative terms of the A^3 . In order to update this equation, we proceed as follows:

- step 0: Start with the given current time step $\mathbf{q}_{mhd}^n = (\rho^n, \rho\mathbf{u}^n, \mathcal{E}^n, \mathbf{B}^n)^T$ and \mathbf{q}_A^n .
- step 1: Apply a standard HCL - WENO method designed for the ideal MHD and obtain \mathbf{q}_{mhd}^* , where

$$\mathbf{q}_{mhd}^* = (\rho^{n+1}, \rho^{n+1}\mathbf{u}^{n+1}, \mathcal{E}^{n+1}, \mathbf{B}^*).$$

Here, \mathbf{B}^* is given with a * superscript instead of $n+1$ to indicate that the predicted \mathbf{B} . Note that since explicit time stepping depends on old data, the only wrong variable is \mathbf{B}^* and it will be corrected using our CT method at each stage of Runge Kutta method before the end of the time step.

- step 2: Solve the magnetic potential equation with diffusion \mathbf{q}_A^{n+1} by applying our proposed MOLT scheme for the Hamilton-Jacobi with diffusion equation (5.3.2).

- step 3: Replace \mathbf{B}^* to \mathbf{B}^{n+1} by a discrete curl of \mathbf{q}_A^{n+1} :

$$\mathbf{B}^{n+1} = \nabla \times \mathbf{q}_A^{n+1}.$$

Note that we do not provide two options for energy density \mathcal{E} as we saw for in the ideal MHD case. Instead, we choose to conserve the total energy of the system. Also, note that as we explained in the section 3.2, we satisfy the divergence free condition automatically, since the divergence of the curl is identically zero.

In the next section, we will explain how we apply a MOLT scheme to approximate the second derivatives appearing in the magnetic potential equation.

Chapter 6

Kernel Based Approximation with Constrained Transport for Resistive MHD

The magnetic potential equation that we have derived for resistive MHD in (5.2) is a Hamilton Jacobi equation with diffusion terms. In this chapter, we will develop a kernel based approximation for that HJ with diffusion equation [22], which now involves second order spatial derivative terms different than the magnetic potential equation for ideal MHD. As in the MOLT framework for the first spatial derivative term we developed in the chapter (3), we also transform second order spatial derivative terms into a kernel based representation. Such representations are also based on successive convolutions. The proposed method in this chapter is a key part of the constrained transport methodology to update the magnetic field solutions in our hybrid resistive MHD solver. We test the performance of the proposed scheme on some benchmark problems in 2D and show some results for different diffusion constant numbers η .

6.1 Hamilton Jacobi with Diffusion terms

The magnetic potential equation for the resistive-MHD system is considered as a Hamilton-Jacobi equation with a diffusion term

$$A_t + H(A_x) = G(A)_{xx}. \quad (6.1.1)$$

The main difference with the ideal case is the appearance of second derivative terms in the equation for the magnetic vector potential. As with the first derivative terms, we transform the second order spatial derivative terms into a kernel based representation. The scheme we propose in this section also keeps the unconditional stability property. For the idea we use in this chapter, we utilize the works [24, 17] and combined it with our HJ solver.

6.2 Approximation of the second order derivative ∂_{xx}

In this subsection, we review the approximations used to form second order derivatives, following the ideas of [24]. Let's define \mathcal{L}_0 operator

$$\mathcal{L}_0 = \mathcal{I} - \frac{1}{\alpha^2} \partial_{xx}, \quad x \in [a, b], \quad (6.2.1)$$

where the \mathcal{I} is the identity operator and $\alpha > 0$ is a constant. For a given function $v(x)$, assume $w(x)$ is the solution of the following differential equation

$$\mathcal{L}_0[w, \alpha](x) = w(x) - \frac{1}{\alpha^2} w_{xx}(x) = v(x). \quad (6.2.2)$$

and $w(x)$ can be found by analytically constructing the inverse of the operator \mathcal{L}_0 as

$$w(x) = \mathcal{L}_0^{-1}[v, \alpha](x) = I^0[v, \alpha](x) + A_0 e^{-\alpha(x-a)} + B_0 e^{-\alpha(b-x)}, \quad (6.2.3)$$

where

$$I^0[v, \alpha](x) := \frac{\alpha}{2} \int_a^b e^{-\alpha|x-y|} v(y) dy, \quad (6.2.4)$$

and A_0 and B_0 are constant values calculated by boundary conditions. For instance, for periodic boundary conditions we have $w(a) = w(b)$ and $w_x(a) = w_x(b)$, then we obtain

$$A_0 = \frac{I^0[v, \alpha](b)}{1 - \mu} \quad \text{and} \quad B_0 = \frac{I^0[v, \alpha](a)}{1 - \mu}, \quad (6.2.5)$$

with $\mu = e^{-\alpha(b-a)}$.

Before we show how we approach second order derivative terms, we present how we evaluate the convolution integral $I^0[v, \alpha_0](x)$. Note that, as stated in section (3.1.2.3), the convolution integrals $I_i^L = I^L[v, \alpha](x_i)$ and $I_i^R = I^R[v, \alpha](x_i)$ satisfy a recursive relation

$$I_i^L = e^{-\alpha \Delta x_i} I_{i-1}^L + J_i^L, \quad i = 1, \dots, N, \quad I_0^L = 0, \quad (6.2.6a)$$

$$I_i^R = e^{-\alpha \Delta x_{i+1}} I_{i+1}^R + J_i^R, \quad i = 0, \dots, N-1, \quad I_N^R = 0, \quad (6.2.6b)$$

where,

$$J_i^L = \alpha \int_{x_{i-1}}^{x_i} v(y) e^{-\alpha(x_i-y)} dy, \quad J_i^R = \alpha \int_{x_i}^{x_{i+1}} v(y) e^{-\alpha(y-x_i)} dy. \quad (6.2.7)$$

Then the convolution integral $I^0[v, \alpha_0](x)$ can be broken into a left-biased integral $I^L[v, \alpha_0](x)$

and right-biased integral $I^R[v, \alpha_0](x)$ such that

$$I^0[v, \alpha_0](x) = \frac{1}{2}(I^L[v, \alpha_0](x) + I^R[v, \alpha_0](x)). \quad (6.2.8)$$

Hence, $I^0[v, \alpha_0](x)$ can be calculated based on left-biased and right-biased integrals, which leads to $\mathcal{O}(N)$ evaluation, see [22, 24].

Now we define a new operator \mathcal{D}_0 as

$$\mathcal{D}_0 = \mathcal{I} - \mathcal{L}_0^{-1}, \quad (6.2.9)$$

and find that $\mathcal{L}_0 = (\mathcal{I} - \mathcal{D}_0)^{-1}$. By using the definition (6.2.1), we can construct the second derivative term with respect to infinite series of the \mathcal{D}_0 as

$$\frac{1}{\alpha^2} \partial_{xx} = \mathcal{I} - \mathcal{L}_0 = \mathcal{L}_0(\mathcal{L}_0^{-1} - \mathcal{I}) = -\mathcal{D}_0(\mathcal{I} - \mathcal{D}_0^{-1}) = -\sum_{p=1}^{\infty} \mathcal{D}_0^p, \quad (6.2.10)$$

where operators are described successively as

$$\mathcal{D}_0^p = \mathcal{D}_0[\mathcal{D}_0^{p-1}]. \quad (6.2.11)$$

Therefore, the term at the right hand side of the equation (6.1.1) can be approximated as

$$G(A)_{xx} = -\alpha^2 \sum_{p=1}^{\infty} \mathcal{D}_0^p[G(A), \alpha](x). \quad (6.2.12)$$

Remember that we have already seen the approximation to the ∂_x in the chapter 3. With that in mind, we can now approximate to the $-H(A_x) + G(A)_{xx}$ with the following combination

of infinite series,

$$\hat{H}\left(-\alpha_L \sum_{p=1}^{\infty} \mathcal{D}_L^p[A^+, \alpha_L], +\alpha_R \sum_{p=1}^{\infty} \mathcal{D}_R^p[A^-, \alpha_R]\right) - \alpha_0^2 \sum_{p=1}^{\infty} \mathcal{D}_0^p[G(A), \alpha_0] \quad (6.2.13)$$

where \hat{H} is numerical Hamiltonian. Here, α_0 , α_L , and α_R are chosen as

$$\alpha_0 = \sqrt{\frac{\beta}{b\Delta t}}, \quad b = \max_A |G'(A)|,$$

$$\alpha_L = \alpha_R = \frac{\beta}{c\Delta t}, \quad c = \max_A |H'(A)|.,$$

where Δt is time step and β is a prescribed constant. We need to truncate the series and calculate only the corresponding partial sums. In particular, $-H(A_x) + G(A)_{xx}$ is approximated by k^{th} partial sums as

$$\begin{aligned} -H(A_x) + G(A)_{xx} \approx \hat{H}\left(-\frac{\beta}{c\Delta t} \sum_{p=1}^k \mathcal{D}_L^p[A^+, \frac{\beta}{c\Delta t}](x), +\frac{\beta}{c\Delta t} \sum_{p=1}^k \mathcal{D}_R^p[A^-, \frac{\beta}{c\Delta t}](x)\right) \\ -\frac{\beta}{b\Delta t} \sum_{p=1}^k \mathcal{D}_0^p[G(A), \sqrt{\frac{\beta}{b\Delta t}}](x) \end{aligned} \quad (6.2.14)$$

with accuracy $\mathcal{O}(\Delta t^k)$. As explained in [22, 24], we have an extra term for the advection part of the Hamilton Jacobi equation, which achieves fourth order accuracy for the case $b \ll c$, i.e., convection dominates. Hence,

$$\begin{aligned} -H(A_x) + G(A)_{xx} \approx \hat{H}\left(-\frac{\beta}{c\Delta t} \sum_{p=1}^k \mathcal{D}_L^p[A^+, \frac{\beta}{c\Delta t}](x), +\frac{\beta}{c\Delta t} \sum_{p=1}^k \mathcal{D}_R^p[A^-, \frac{\beta}{c\Delta t}](x)\right) \\ -\frac{\beta}{b\Delta t} \sum_{p=1}^k \mathcal{D}_0^p[G(A), \sqrt{\frac{\beta}{b\Delta t}}](x) \end{aligned} \quad (6.2.15)$$

$$\hat{H}\left(+\frac{\beta}{c\Delta t}\mathcal{D}_0\left[\mathcal{D}_L^2[A^+, \frac{\beta}{c\Delta t}], -\mathcal{D}_R^2[A^-, \frac{\beta}{c\Delta t}], \frac{\beta}{c\Delta t}\right](x)\right)$$

6.2.0.1 Periodic boundary conditions

For periodic boundary conditions, we require

$$A(a, t) = A(b, t), \quad A_x(a, t) = A_x(b, t), \quad t \geq 0, \quad (6.2.16)$$

the convolution operators are required to satisfy

$$\mathcal{D}_0^p[G(A), \alpha_0](a) = \mathcal{D}_0^p[G(A), \alpha_0](b),$$

$$\mathcal{D}_L^p[H^+(A), \alpha_L](a) = \mathcal{D}_L^p[H^+(A), \alpha_L](b), \quad (6.2.17)$$

$$\mathcal{D}_R^p[H^-(A), \alpha_R](a) = \mathcal{D}_R^p[H^-(A), \alpha_R](b).$$

For periodic boundary conditions, the coefficients A_0 and B_0 are prescribed by equation (6.2.5). Recall that the coefficients A_L and B_R for periodic boundary conditions were provided in section (3.1.2).

6.3 Numerical Results for Resistive MHD for Periodic Boundary Condition

In this section we will show some numerical results using resistive MHD equations for our proposed scheme. The results shown here are to test our method using periodic boundary conditions. We use third order SSP RK method for time discretization. Time step is chosen

as

$$\Delta t = \frac{\text{CFL}}{em * cd} \quad (6.3.1)$$

where the CFL number is 1, $em = \max(\lambda^5, \lambda^6)$, $cd = \frac{1}{\Delta x} + \frac{1}{\Delta y}$ for 2D. This is CFL condition of hyperbolic conservation laws, where the magnetic potential equation \mathbf{A} with diffusion is solved by kernel based method which is unconditionally stable. We choose $\beta = 0.8$ for α_L and α_R whereas $\beta = 0.4$ for α_0 . In the numerical experiments here, we have used kernel based method for $k=3$. As stated in section (6.2), the approximation to magnetic potential equation is expected to be fourth order accurate. In this section, we compare our MHD solver based on MOLT with the WENO-FD solver, which was originally designed for Hamilton Jacobi equations, but we add a second order explicit in time approximation for diffusion term. Note that, the WENO-FD scheme is designed based on explicit time stepping and has a restricted CFL condition for diffusion terms by von Neumann stability analysis. Thus, for finite difference with explicit diffusion we use $\Delta t < \min(\frac{1}{em*cd}, \frac{(\Delta x)^2}{2b})$, where b is the diffusivity and em is the maximum wave speed coming from the eigenvalues. We are comparing the CFL restriction of the advection part and the diffusion part and make sure we take the smallest time step. However, our MOLT solver is capable to take larger time steps comparing to WENO-FD since our proposed HJ based on MOLT with diffusion behaves unconditionally stable.

6.3.1 Refinement Study for Smooth Vortex Problem

We performed a successive spatial refinement study for the smooth vortex problem with diffusion with 100×100 at final time $t = 0.03$ for the diffusion $\eta = 0.1$. For refinement study

we choose CFL=1 and $\beta = 0.6$ for advection while $\beta = 0.4$ for diffusion part.

In Table (6.1), we provide a table of error results, which demonstrate that the method achieves high order accuracy (almost 5th order of accuracy) in space since 5th order WENO-quadrature is used.

Table 6.1: Smooth vortex problem. Errors of A and orders of accuracy.

| $N_x \times N_y$ | L_1 error | order | L_∞ error | order |
|------------------|-------------|-------|------------------|-------|
| 32×32 | 1.9162E-04 | – | 6.6734E-02 | – |
| 64×64 | 1.1876E-05 | 4.01 | 3.9467E-03 | 4.08 |
| 128×128 | 4.7350E-07 | 4.65 | 2.6466E-04 | 3.90 |
| 256×256 | 1.6577E-08 | 4.84 | 1.0801E-05 | 4.61 |

6.3.2 Smooth Vortex Problem for Resistive MHD

In Figures 6.1 and 6.2 we show the results at the final time $t = 20$ using a 100×100 mesh and CFL=. At time $t = 20$, the solution has advanced by one period. The results are for different diffusion coefficients $\eta = 0, 0.001, 0.1, 0.5, 1$. We compare the FD-WENO scheme with our MOLT scheme. While the FD-WENO scheme can only give results up to $\eta = 0.5$, our method works well, even for $\eta = 1$. Moreover, the ability of taking CFL=1 for MOLT is computationally efficient. For example, for the case of $\eta = 0.5$ our solver requires %23 less time than the FD with diffusion method due to its CFL restriction $\Delta t < \min(\frac{1}{2*em*cd}, \frac{(\Delta x)^2}{2b})$. Note that once we refine the problem in space, $\frac{(\Delta x)^2}{2b}$ will dominate the CFL selection and we will get more time steps, thus we will get square more efficiency comparing to explicit scheme. This is a simple benchmark problem and there are better ways to solve the diffusion terms.

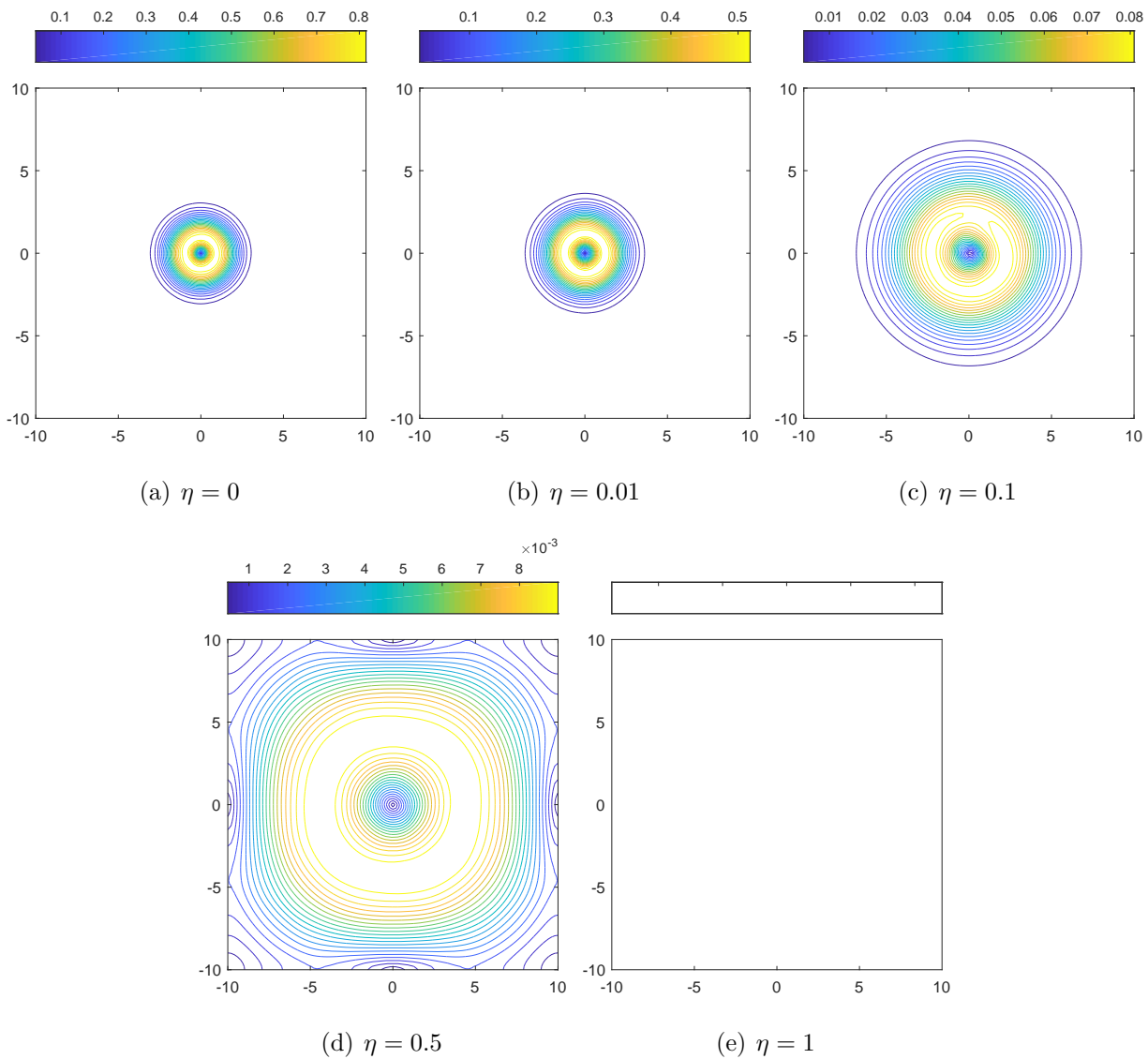


Figure 6.1: (FD) Contour plots of $\|\mathbf{B}\|$ at time $t = 20$ with $\Delta x = \Delta y = 0.2$.

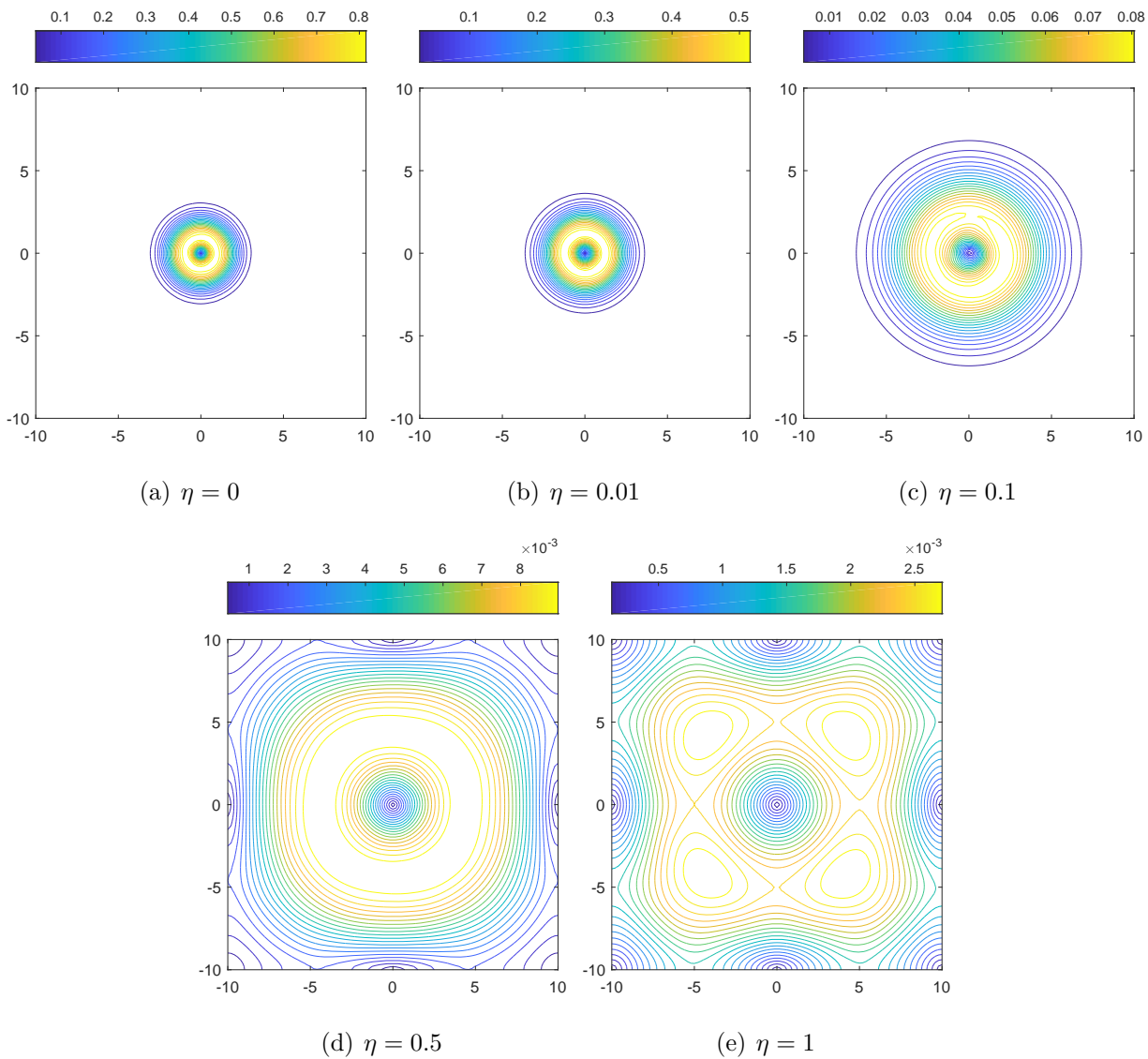


Figure 6.2: (Kernel based method) Contour plots of $\|\mathbf{B}\|$ at time $t = 20$ with $\Delta x = \Delta y = 0.2$.

6.4 Orszag Tang Vortex problem for Resistive MHD

In this section we conduct a refinement study and show 2D contour plots of the density for the Orszag Tang Vortex problem with a resistive MHD model. The Orszag Tang Vortex problem is a good benchmark for numerical schemes, as the solution is sensitive to divergence errors in the magnetic field. We have two-way periodic boundary conditions on a domain $[0, 2\pi] \times [0, 2\pi]$. We use 192×192 for mesh size, and $\beta = 0.8$ for advection part whereas $\beta = 0.2$ for the diffusion part. We are able to take a CFL of 1 for MOLT, while CFL relation is $\Delta t < \min(\frac{1}{em*cd}, \frac{(\Delta x)^2}{2b})$ for WENO-FD due to the stability condition for the diffusion terms for the explicit time stepping. With this CFL, MOLT requires less time to run the problem.

6.4.1 Refinement Study for Orszag Tang Vortex problem for Resistive MHD

We show the successive refinement study in this section. The mesh size is 192×192 at time $t = 0.03$. we choose $\beta = 0.8$ for advection part whereas $\beta = 0.4$ for the diffusion part and use CFL=0.5 for refinement study. In table (6.2) we obtain 5th order accuracy in space for A and in table (6.3) we show the time refinement and observe 4th order in time, which thereby verifying the analysis presented in section (6.2). Note that we use 5th order WENO-based quadrature for space discretization and observe 5th order accuracy in space as expected based on the analysis presented in section (6.2), which confirms the theory.

Table 6.2: Errors of A and orders of accuracy.

| $N_x \times N_y$ | L_1 error | order | L_∞ error | order |
|------------------|-------------|-------|------------------|-------|
| 16×16 | 1.7425E-03 | – | 9.4445E-03 | – |
| 32×32 | 1.0593E-04 | 4.04 | 7.7115E-04 | 3.61 |
| 64×64 | 3.1380E-06 | 5.08 | 3.1896E-05 | 4.60 |
| 128×128 | 6.7905E-08 | 5.53 | 8.3855E-07 | 5.25 |

Table 6.3: Errors of A and orders of temporal accuracy.

| CFL | L_1 error | order | L_∞ error | order |
|-------|-------------|-------|------------------|-------|
| 0.5 | 2.4474E-03 | – | 1.1966E-03 | – |
| 0.25 | 1.5242E-04 | 4.01 | 6.6924E-05 | 4.16 |

6.4.2 Orszag Tang Vortex problem with diffusion for Resistive MHD

We add diffusion terms for the magnetic potential for this problem and we want to see the evolution of the problem for the different diffusion constants $\eta = 0, 0.001, 0.1$ and 1 . In Figures 6.3 and 6.4 we compare the solutions obtained from a FD scheme to those of our proposed MOLT scheme, at the final time $t = 3$ with a 192×192 mesh. We are able to use CFL of one for MOLT, while we can use the CFL relation $\Delta t < \min(\frac{1}{em*cd}, \frac{(\Delta x)^2}{2b})$ for WENO-FD. With the ability of taking larger time steps, we need less time to run the problems. For example, for the case of $\eta = 0.01$ MOLT code requires 40% less time comparing to FD-WENO code. Note that as stated in the previous example, once we refine the problem in space, then the diffusion restriction of CFL will dominate the CFL selection for Finite Differencing method and cause more time steps, thus we will get square more efficiency comparing the WENO-FD method.

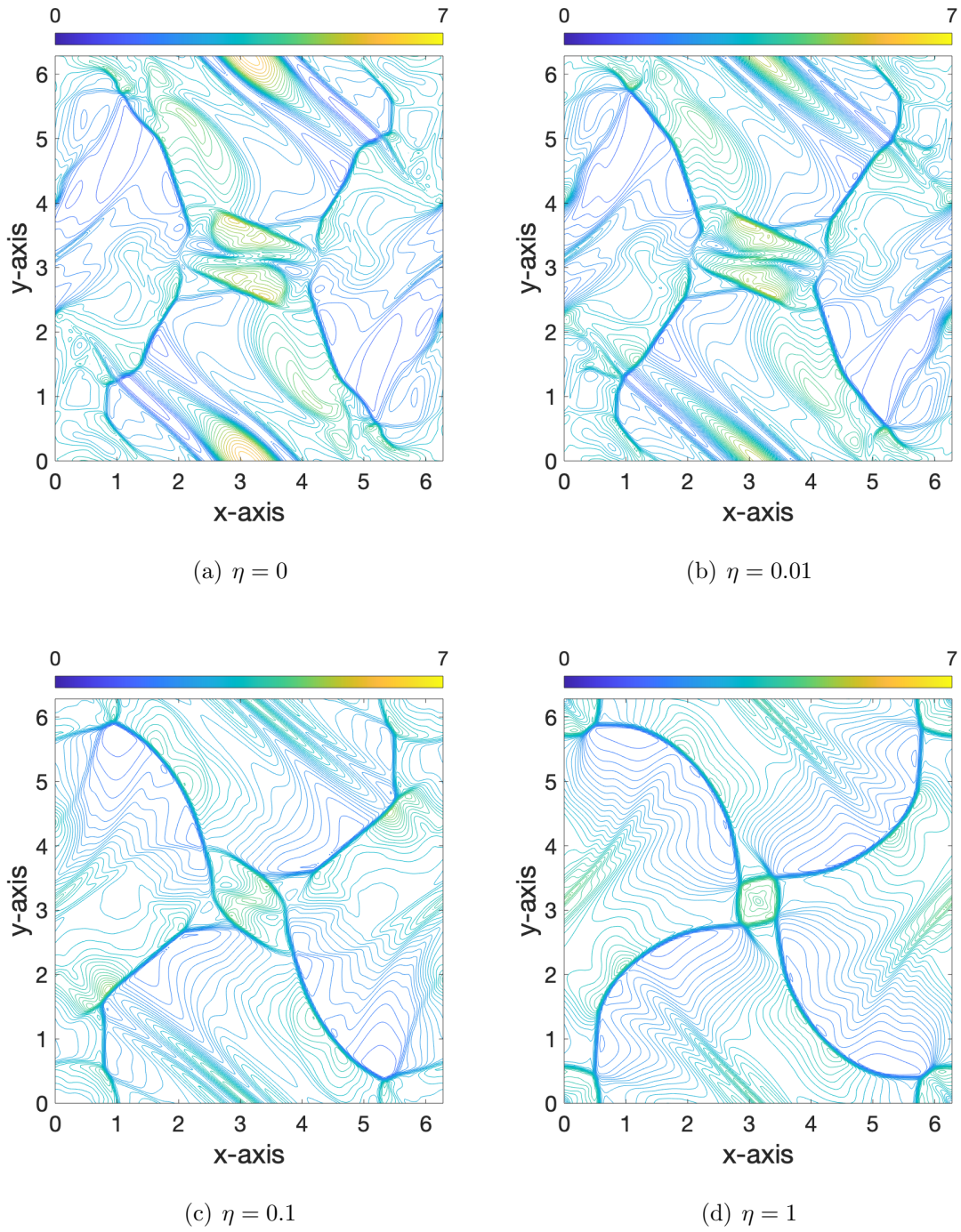


Figure 6.3: (FD) Contour plots of ρ at time $t = 3$ with 192×192 .

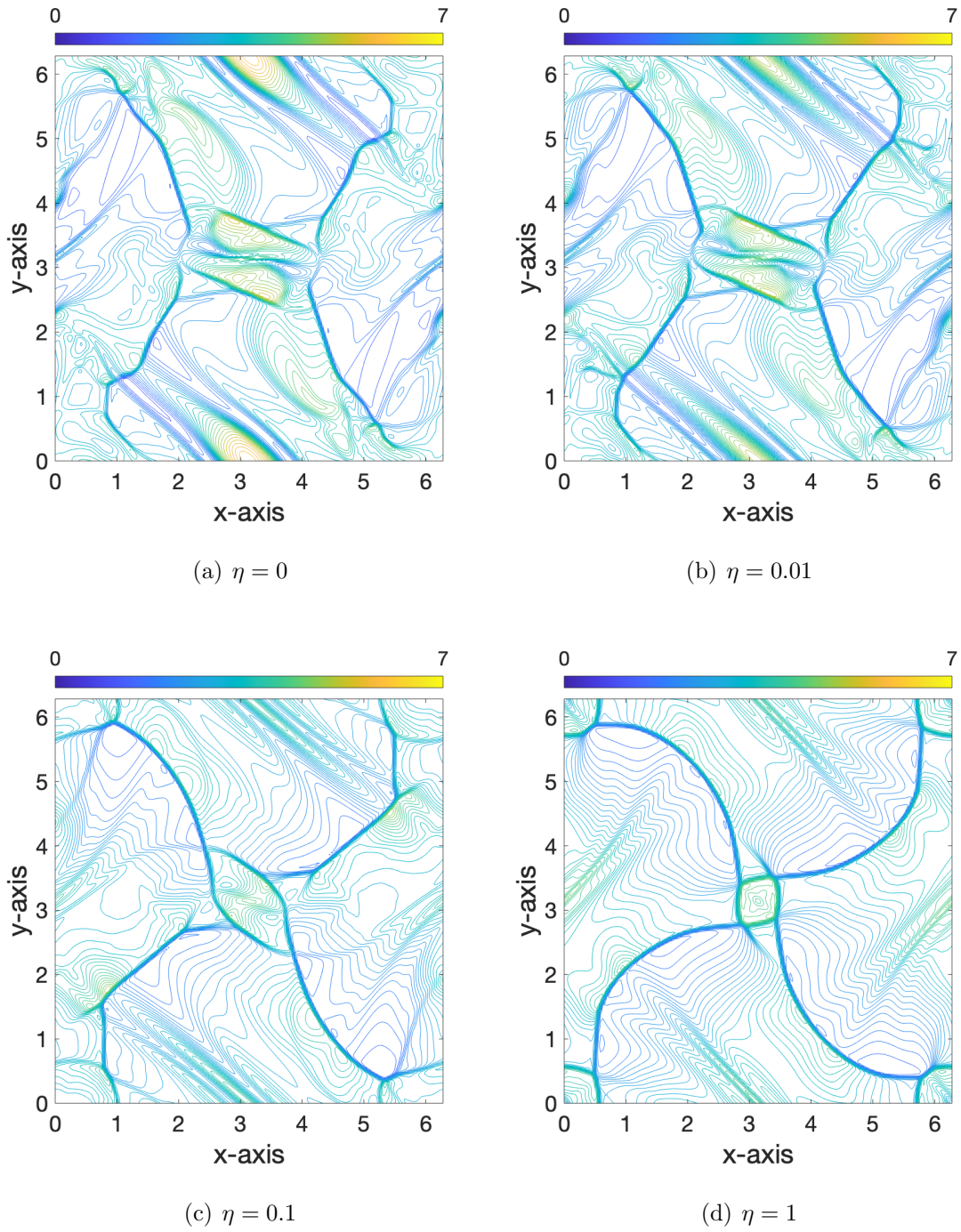


Figure 6.4: (MOLT) Contour plots of ρ at time $t = 20$ with 192×192 .

Chapter 7

MOLT for PEC for non-ideal MHD

Equations

In this chapter we will expand our resistive MHD solver to work for perfectly electrically conducting (PEC) boundary condition. In the chapter 4, we have presented the PEC boundary conditions for ideal MHD case, which we only had first order spatial derivative terms in the magnetic potential equation. We have utilized the Cauchy-Kowalevski theorem there to derive boundary terms A_L and B_R . However, it is not that easy to use Cauchy-Kowalevski theorem for the second order derivative cases. Thus, we are using the method for diffusion that is consistent with our approach that is only 1st order at the boundary. Note that we are not correcting at the boundary and leaving that for future work to achieve higher order accuracy. Then we will demonstrate the results on several test problems such as the Hartmann Flow and the GEM challenge problem.

7.1 MOLT for PEC for non-ideal MHD

In this section we examine the operator D_0 for non periodic boundary condition, which we use for the approximation of the second order derivative terms.

$$\mathcal{D}_0[v, \alpha](x) = v(x) - \frac{\alpha}{2} \int_a^b e^{-\alpha|x-y|} v(y) dy - A_0 e^{-\alpha(x-a)} - B_0 e^{-\alpha(b-x)}. \quad (7.1.1)$$

where A_0 and B_0 are determined by the boundary conditions. Following the idea in [23], if we require non periodic boundary conditions, we assume that we are given numbers C_a and C_b . If we require

$$\mathcal{D}_0[v, \alpha](a) = C_a, \quad \text{and} \quad \mathcal{D}_0[v, \alpha](b) = C_b,$$

then, the boundary coefficients are obtained as

$$A_0 = \frac{1}{1 - \mu^2} (\mu (I^0[v, \alpha](b) - v(b) + C_b) - (I^0[v, \alpha](a) - v(a) + C_a)), \quad (7.1.2a)$$

$$B_0 = \frac{1}{1 - \mu^2} (\mu (I^0[v, \alpha](a) - v(a) + C_a) - (I^0[v, \alpha](b) - v(b) + C_b)). \quad (7.1.2b)$$

In the next section we will test our code on several test problems such as the Hartmann Flow problem and the GEM Magnetic Reconnection problem.

7.2 Numerical results for Hartmann Flow problem with diffusion

The kernel based approximation based on the MOLT for PEC boundary conditions for the second order derivative term will be tested on the Hartmann Flow which is derived in the section (4.2). This benchmark problem is a good test problem to test the code both for ideal and non-ideal MHD models. Here, we will let the diffusion variable η be nonzero and we will test our code for the diffusion effect.

We choose $\beta = 0.8$ for α_L and α_R whereas $\beta = 0.6$ for α_0 . Since the Hartmann problem assumes the MHD model to be incompressible, we use $\rho = 1$ and $p = 1$. We show refinement study in the table (7.1) at time $t = 0.1$ for diffusion $\eta = 0.1$ and we choose CFL=0.5 for

refinement study. We get low order of accuracy in space since we only use first order accurate boundary terms A_0 and B_0 for PEC boundary conditions for diffusion, while we use higher order approximations in the domain. In this test problem we observe that we get first order accuracy for magnetic potential equation as expected by the theory. Note that we intend to achieve higher order approximations for PEC boundary conditions for diffusion in the future by correcting boundary terms A_0 and B_0 . For resolution 128×128 , final time $t = 1$,

Table 7.1: Hartmann flow problem. Errors of A and orders of accuracy.

| $N_x \times N_y$ | L_1 error | order | L_∞ error | order |
|------------------|-------------|-------|------------------|-------|
| 32×32 | 3.1362E-07 | – | 3.0554E-06 | – |
| 64×64 | 1.8958E-07 | 0.73 | 2.1523E-06 | 0.51 |
| 128×128 | 1.0127E-07 | 0.90 | 1.2318E-06 | 0.81 |
| 256×256 | 5.2168E-08 | 0.96 | 6.5960E-07 | 0.90 |

CFL=1 and $\eta = 0.001$, the velocity and the induced magnetic field solutions for the different Hartmann numbers are shown in figures 7.1 and 7.3. In Figures 7.2 and 7.4, we presented 1D cross sections of velocity and induced magnetic field for different Hartmann numbers $Ha = 0, 2, 5, 10$. The numerical results overlap on the exact solutions.

7.3 Magnetic reconnection: GEM challenge problem

The main motivation of going beyond the ideal MHD by including additional physics in the plasma model is to observe the magnetic reconnection phenomenon, which is a significant cosmic plasma process. This phenomenon has an effect on the dynamics of the magnetosphere by facilitating the entry of particles and energy from the Sun’s atmosphere into the Earth’s magnetosphere at the magnetopause by the solar wind. When the high energy parti-

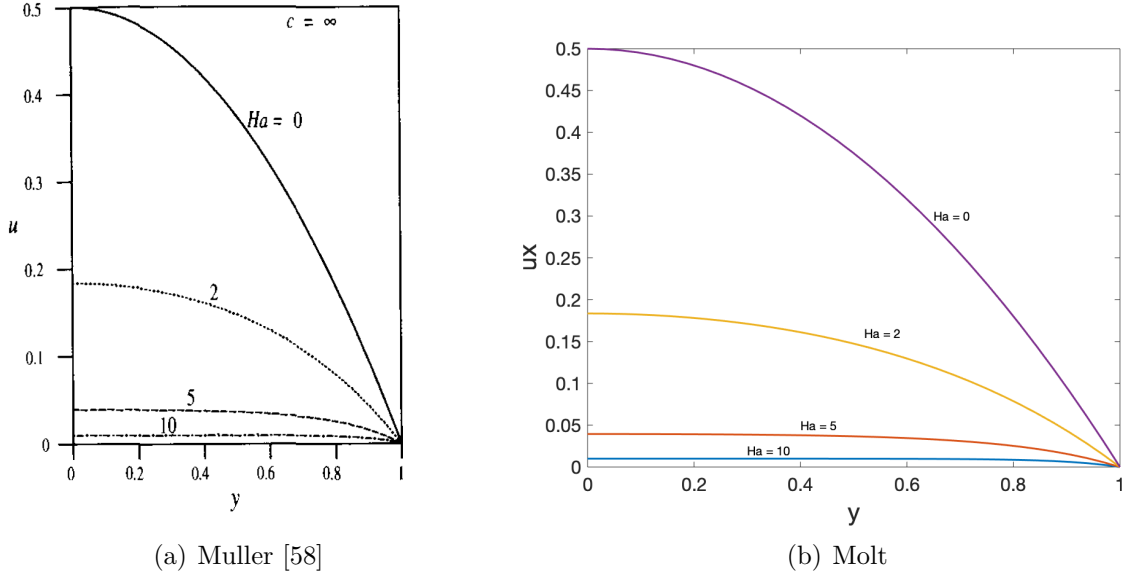


Figure 7.1: Velocity profile for the Hartmann problem at $Ha = 0, 2, 5, 10$.

cles reach Earth and magnetic reconnection happens, then this restricts the performance of fusion reactors and also affects the geospace weather which can damage power grids, communication systems, GPS navigation and threaten spacecraft and satellites. One other effect of reconnection is believed to be helping trigger aurora, also known as the northern and southern lights. What the magnetic reconnection really is the breaking and reconnecting of magnetic field lines in a highly conducting plasma. The magnetic field lines get squeezed together as magnetized plasma flows are going toward each other. The particles resist being squeezed together and the field lines are broken and the reconnection happens in the tiny diffusion region.

In plasma physics, it is known that for magnetic reconnection to occur, a mechanism is required to break the "frozen-in" flux condition, which could be resistivity, electron inertia or anisotropic electron pressure, which appear in the generalized Ohm's law. This phenomenon does not occur in the ideal MHD plasma (infinitely conductive plasma). In this work, it is

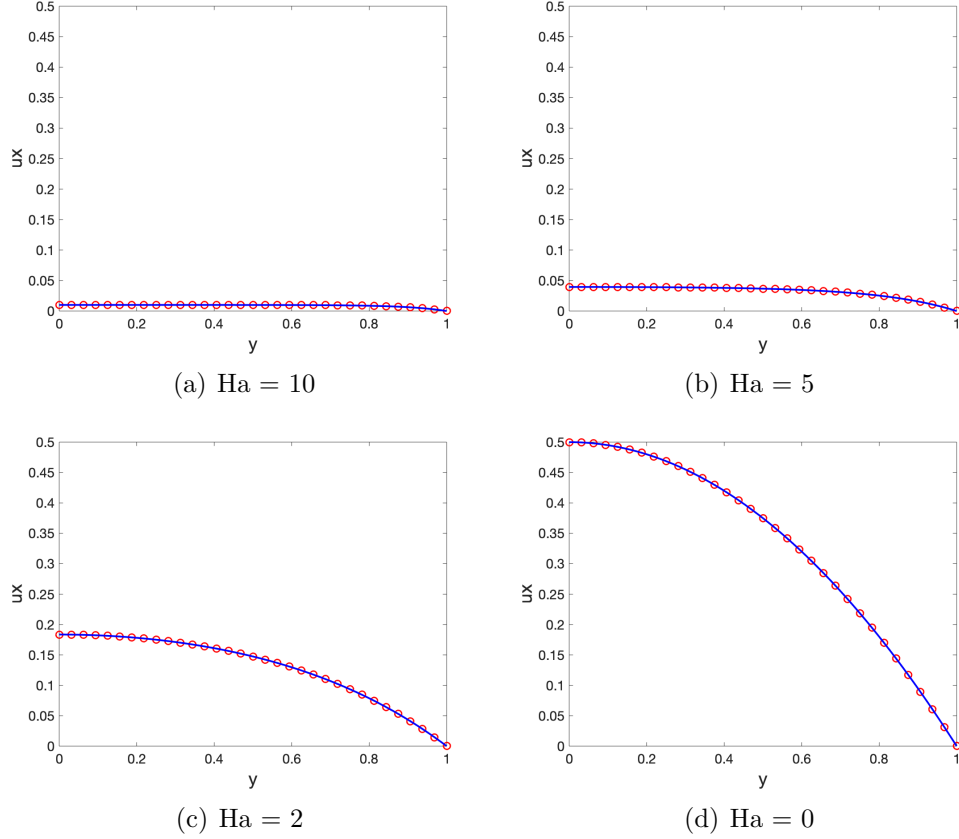


Figure 7.2: Exact and Numerical velocity solutions for the Hartmann problem at $Ha = 0, 2, 5, 10$.

the resistivity that breaks this condition since we work within the resistive MHD model.

The Geospace Environment Modeling (GEM) Magnetic Reconnection Challenge Problem [9] is one of the benchmark problems of magnetic reconnection and it is studied in this work. The study of Magnetic Reconnection is on a simple 2D current-sheet, called the Harris sheet configuration, with a specified set of initial conditions and magnetic island perturbation to trigger the dynamics. The Harris sheet configuration is a planar MHD equilibrium with a horizontal magnetic field given by

$$B^1(y) = B_0 \tanh(y/\lambda_B). \tag{7.3.1}$$

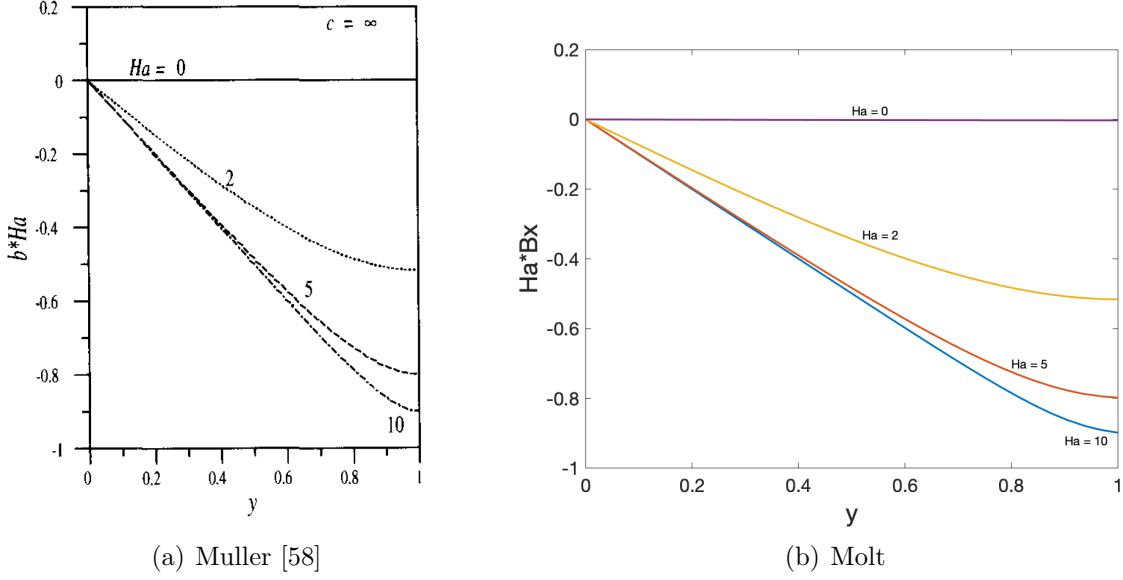


Figure 7.3: Induced magnetic field for the Hartmann problem at $Ha = 0, 2, 5, 10$.

Assume a uniform temperature $T = T_0$ and a density profile given by

$$\rho(y) = \rho_0 \cosh^{-2}(y/\lambda_B) + \rho_\infty. \quad (7.3.2)$$

The initial equilibrium is perturbed by an additional magnetic perturbation

$$\begin{aligned} \delta B^1(x, y) &= -\psi(\pi/L_y) \cos(2\pi x/L_x) \sin(\pi y/L_y) \\ \delta B^2(x, y) &= \psi(2\pi/L_x) \sin(2\pi x/L_x) \cos(\pi y/L_y). \end{aligned} \quad (7.3.3)$$

The standard case takes $-\frac{1}{2}L_x < x < \frac{1}{2}L_x$ and $-\frac{1}{2}L_y < y < \frac{1}{2}L_y$ with $L_x = 25.6$ and $L_y = 12.8$. The simulations use periodic boundary conditions horizontally, while perfectly conducting impenetrable walls are assumed at $y = \pm\frac{1}{2}L_y$. A perfectly conducting wall is a solid wall boundary and can be given as follows

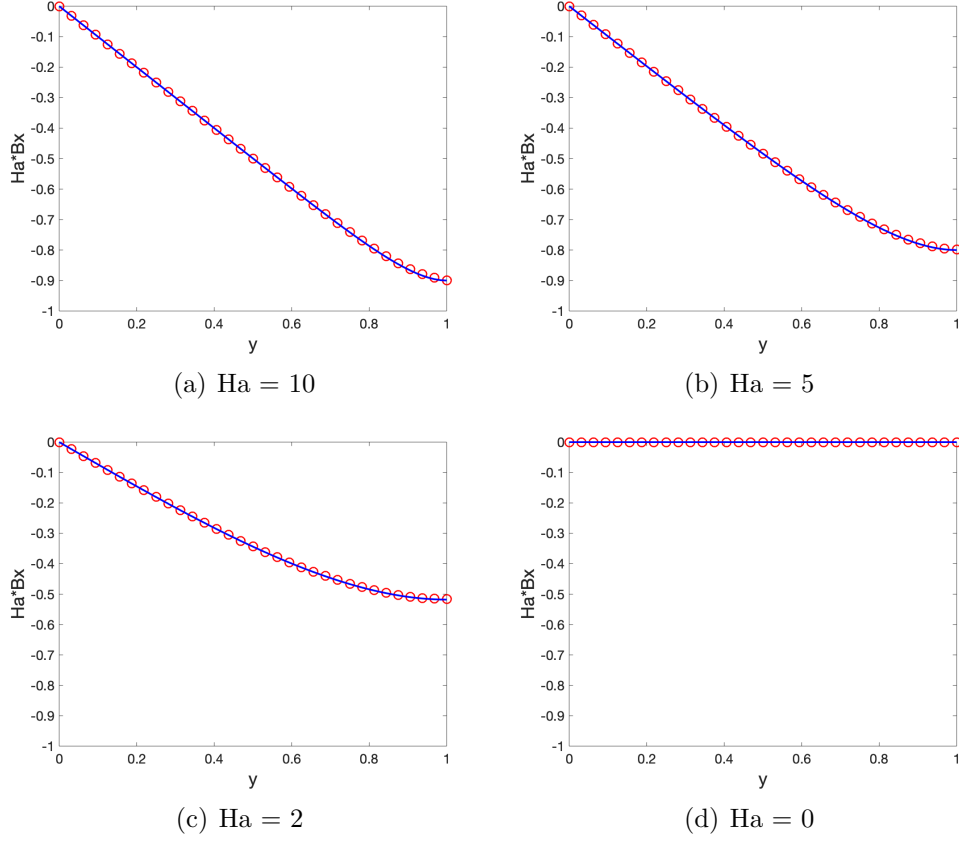


Figure 7.4: Exact and Numerical induced magnetic field solutions for the Hartmann problem at $Ha = 0, 2, 5, 10$.

$$\partial_y \rho = 0, \quad \partial_y \mathbf{B}_x = \mathbf{B}_y = \partial_y \mathbf{B}_z = 0 \quad (7.3.4)$$

$$\partial_y \mathbf{u}_x = \mathbf{u}_y = \partial_y \mathbf{u}_z = 0, \quad \mathbf{E}_x = \partial_y \mathbf{E}_y = \mathbf{E}_z = 0 \quad (7.3.5)$$

In Figure (7.7), we have presented our kernel based method results for the GEM challenge problem and compared it with the work done by Birn et. al., [9]. The mesh spacing is 128×128 with $CFL = 1$. We use $\beta = 0.8$ for the advection part of the equation while $\beta = 0.6$ for the diffusion part. The plots show the evolution of the magnetic field lines and current density for the resistive MHD for uniform resistivity $\eta = 0.001$. The formation of the

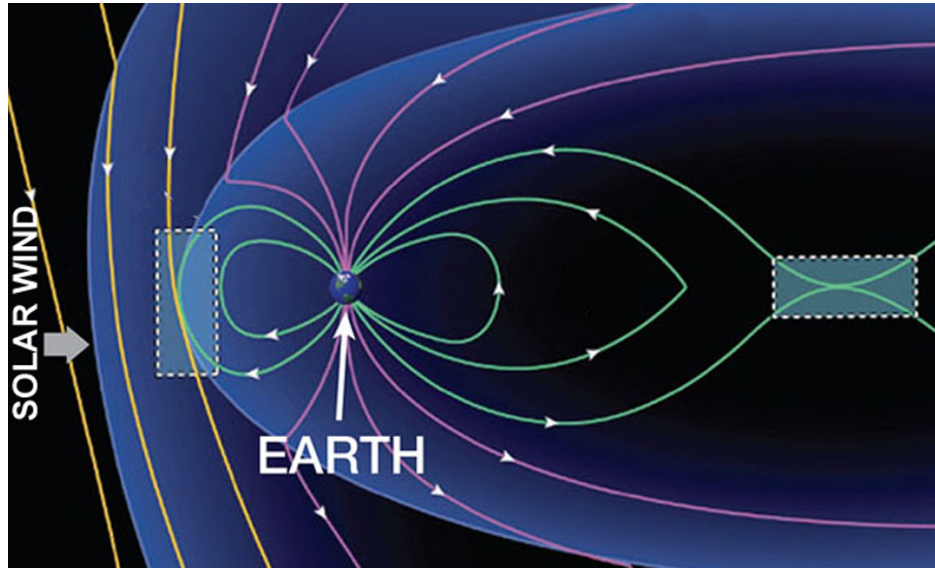


Figure 7.5: Magnetic Reconnection in Space. **Credits: NASA**

magnetic island in the center of the current sheet matches the work done by the Birn et. al., [9]. The magnetic island is increasing over the time and then merging with the bigger island to the left.

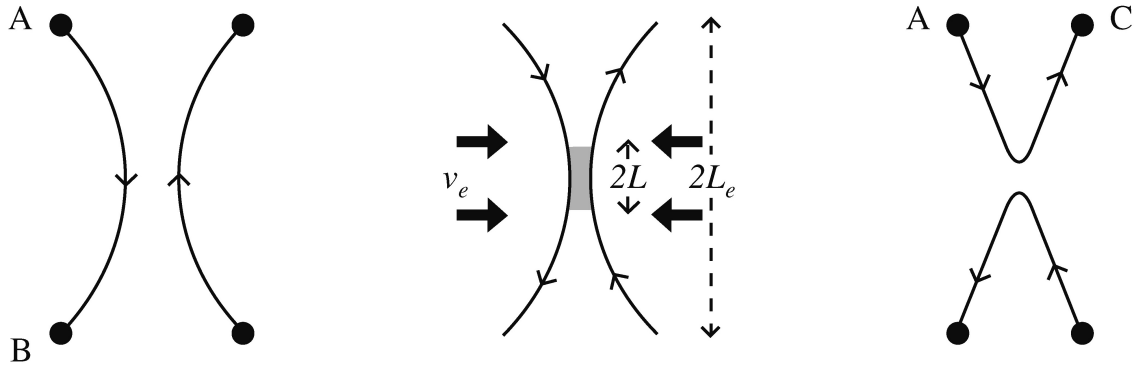


Figure 7.6: Breaking and rejoining of magnetic field lines due to the presence of localized diffusion region (shaded). (Priest, E. R [63])

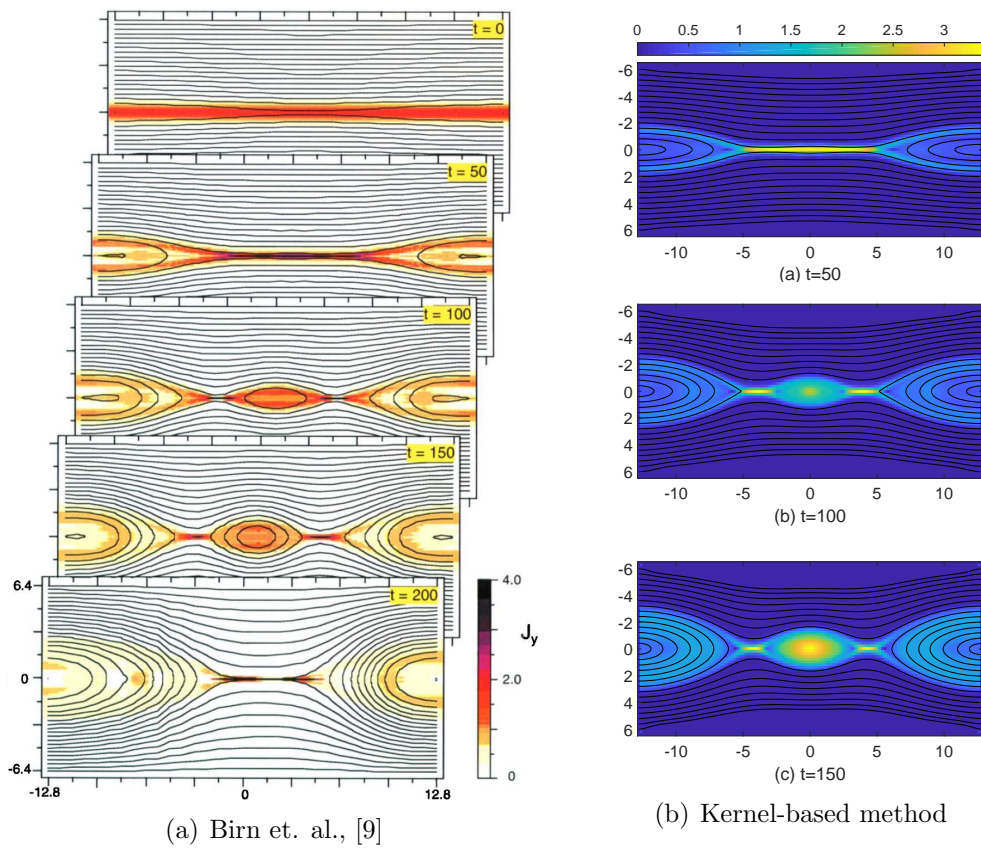


Figure 7.7: GEM Magnetic Reconnection Problem for diffusion $\eta = 0.001$.

Chapter 8

Conclusion and Future Work

8.1 Conclusion

In this work we developed a kernel based constrained transpose scheme based on the magnetic vector potential equations in 2D and 3D for ensuring that the solution of the magnetic field in ideal MHD is divergence free. The development of the method relies on a kernel based formulation of the spatial derivatives. The framework of the current method is derived from the method of lines transpose methodology and the key idea of successive convolution. The method relies on the idea of replacing a local operator with a global operator that is as efficient as an explicit method, but because it is global it provides an unconditionally stable method when coupled with explicit time stepping. For time integration, we coupled the method with the high order explicit strong stability preserving Runge-Kutta scheme. The most important conclusion of this work is that the newly proposed method offers an approach to constrained transport that is mesh aligned for AMR and does not rely on diffusion limiter for stability in 3D, which we needed in our previous work [29]. Eliminating the need of diffusion limiter improves solutions where there are strong shocks, and as demonstrated in numerical simulations, the approach also works well for smooth problems. In addition, the new method is unconditionally stable and achieves high order accuracy. The method is robust and has been tested on a range of 2D and 3D test problems, such as the field loop

and blast wave problems.

In Chapter 4, we developed the PEC boundary conditions for magnetic potential equation in MOLT-HJ scheme. In fact, the PEC boundary condition is equivalent enforcing Dirichlet boundary conditions. We derived the MOLT-HJ scheme for Dirichlet boundary conditions for magnetic potential equation. Then we go over the derivation of the Hartmann Flow problem, which is a benchmark problem to test PEC boundary conditions both for ideal and non ideal MHD equations. We get high order accuracy for ideal Hartmann problem. We also showed that the exact solution and the numerical solutions overlap each other by showing 1D cross sections and 2D contour plots.

In Chapter 5, we further our work from ideal MHD to resistive Magnetohydrodynamics model. We derived the magnetic potential equation from the magnetic field equation which has the diffusion term in it. We obtained Hamilton-Jacobi with diffusion type of equation for magnetic potential equation, which still satisfies the divergence free condition for the magnetic field. We had a kernel based approximation for the first derivative terms in the ideal MHD in Chapter 3, then in the Chapter 6 we developed a similar approximation for the second order derivative terms existed in the magnetic potential equation for the resistive MHD. We presented MOLT-HJ method for the periodic boundary conditions. We tested our code for periodic boundary conditions on the several 2D test problems. We get high order accuracy on these examples, Smooth Vortex and Orszag Tang Vortex problems. We also presented 2D plots of these problems both for FD-WENO code and our MOLT-HJ code for different diffusion constants η . We observe that MOLT-HJ is working well and requires less time since our kernel based approximation is unconditionally stable and allows taking larger time steps.

In Chapter 7, we introduced the PEC boundary conditions for the MOLT method for

non-ideal case of MHD equations. We tested our work on both Hartmann Flow problem and GEM Magnetic Reconnection Problems. For the resistive flow example, we get first order of accuracy for the Hartmann problem and left the study of making it higher order for the future.

8.2 Future Work

The main objective of resistive MHD work is to solve the Magnetic Reconnection problem for the PEC boundary condition at the top and bottom and periodic boundary conditions at the left and right boundaries. The non-ideal evaluation of code gave us low order of accuracy so far. For such an important problem we will endeavor to obtain a higher order of accuracy in future work.

We also will seek to further our resistive MHD work to the Hall MHD equations by including more physics in Ohm's law. That problem is more sensitive to diffusions and is challenging to solve. Keeping the Hall terms in the equations will not change the structure of the magnetic potential equation, thus we will be able to use our Constrained Transpose methodology for resistive MHD model to the Hall MHD model.

APPENDIX

Appendix

WENO-Integration Formulation

Here, we show all coefficients in WENO quadrature. We denote $\gamma = \alpha\Delta x$, then we have

$$\begin{aligned}c_0^{(0)} &= \frac{6 - 6\nu + 2\nu^2 - (6 - \nu^2)e^{-\nu}}{6\nu^3}, \\c_1^{(0)} &= -\frac{6 - 8\nu + 3\nu^2 - (6 - 2\nu - 2\nu^2)e^{-\nu}}{2\nu^3}, \\c_2^{(0)} &= \frac{6 - 10\nu + 6\nu^2 - (6 - 4\nu - \nu^2 + 2\nu^3)e^{-\nu}}{2\nu^3}, \\c_3^{(0)} &= -\frac{6 - 12\nu + 11\nu^2 - 6\nu^3 - (6 - 6\nu + 2\nu^2)e^{-\nu}}{6\nu^3}, \\c_0^{(1)} &= \frac{6 - \nu^2 - (6 + 6\nu + 2\nu^2)e^{-\nu}}{6\nu^3}, \\c_1^{(1)} &= -\frac{6 - 2\nu - 2\nu^2 - (6 + 4\nu - \nu^2 - 2\nu^3)e^{-\nu}}{2\nu^3}, \\c_2^{(1)} &= \frac{6 - 4\nu - \nu^2 + 2\nu^3 - (6 + 2\nu - 2\nu^2)e^{-\nu}}{2\nu^3}, \\c_3^{(1)} &= -\frac{6 - 6\nu + 2\nu^2 - (6 - \nu^2)e^{-\nu}}{6\nu^3}, \\c_0^{(2)} &= \frac{6 + 6\nu + 2\nu^2 - (6 + 12\nu + 11\nu^2 + 6\nu^3)e^{-\nu}}{6\nu^3}, \\c_1^{(2)} &= -\frac{6 + 4\nu - \nu^2 - 2\nu^3 - (6 + 10\nu + 6\nu^2)e^{-\nu}}{2\nu^3}, \\c_2^{(2)} &= \frac{6 + 2\nu - 2\nu^2 - (6 + 8\nu + 3\nu^2)e^{-\nu}}{2\nu^3}, \\c_3^{(2)} &= -\frac{6 - \nu^2 - (6 + 6\nu + 2\nu^2)e^{-\nu}}{6\nu^3}u_{i+2}.\end{aligned}$$

And the linear weights are

$$d_0 = \frac{6 - \nu^2 - (6 + 6\nu + 2\nu^2)e^{-\nu}}{3\nu((2 - \nu) - (2 + \nu)e^{-\nu})}$$

$$d_2 = \frac{60 - 60\nu + 15\nu^2 + 5\nu^3 - 3\nu^4 - (60 - 15\nu^2 + 2\nu^4)e^{-\nu}}{10\nu^2(6 - \nu^2 - (6 + 6\nu + 2\nu^2)e^{-\nu})}$$

$$d_1 = 1 - d_0 - d_2.$$

The smoothness indicator β_r have the expressions as

$$\beta_0 = \frac{13}{12}(-v_{i-3} + 3v_{i-2} - 3v_{i-1} + v_i)^2 + \frac{1}{4}(v_{i-3} - 5v_{i-2} + 7v_{i-1} - 3v_i)^2,$$

$$\beta_1 = \frac{13}{12}(-v_{i-2} + 3v_{i-1} - 3v_i + v_{i+1})^2 + \frac{1}{4}(v_{i-2} - v_{i-1} - v_i + v_{i+1})^2,$$

$$\beta_2 = \frac{13}{12}(-v_{i-1} + 3v_i - 3v_{i+1} + v_{i+2})^2 + \frac{1}{4}(-3v_{i-1} + 7v_i - 5v_{i+1} + v_{i+2})^2.$$

BIBLIOGRAPHY

BIBLIOGRAPHY

- [1] D. S. Balsara. Divergence-free adaptive mesh refinement for magnetohydrodynamics. *Journal of Computational Physics*, 174(2):614–648, 2001.
- [2] D. S. Balsara. Second-order-accurate schemes for magnetohydrodynamics with divergence-free reconstruction. *The Astrophysical Journal Supplement Series*, 151(1):149, 2004.
- [3] D. S. Balsara. Divergence-free reconstruction of magnetic fields and weno schemes for magnetohydrodynamics. *Journal of Computational Physics*, 228(14):5040–5056, 2009.
- [4] D. S. Balsara and J. Kim. A comparison between divergence-cleaning and staggered-mesh formulations for numerical magnetohydrodynamics. *The Astrophysical Journal*, 602(2):1079, 2004.
- [5] D. S. Balsara, C. Meyer, M. Dumbser, H. Du, and Z. Xu. Efficient implementation of ader schemes for euler and magnetohydrodynamical flows on structured meshes—speed comparisons with runge–kutta methods. *Journal of Computational Physics*, 235:934–969, 2013.
- [6] D. S. Balsara, T. Rumpf, M. Dumbser, and C.-D. Munz. Efficient, high accuracy ader-weno schemes for hydrodynamics and divergence-free magnetohydrodynamics. *Journal of Computational Physics*, 228(7):2480–2516, 2009.
- [7] D. S. Balsara and D. Spicer. Maintaining pressure positivity in magnetohydrodynamic simulations. *Journal of Computational Physics*, 148(1):133–148, 1999.
- [8] D. S. Balsara and D. S. Spicer. A staggered mesh algorithm using high order godunov fluxes to ensure solenoidal magnetic fields in magnetohydrodynamic simulations. *Journal of Computational Physics*, 149(2):270–292, 1999.
- [9] J. Birn and M. Hesse. Geospace environment modeling (gem) magnetic reconnection challenge: Resistive tearing, anisotropic pressure and hall effects. *Journal of Geophysical Research: Space Physics*, 106(A3):3737–3750, 2001.
- [10] D. Biskamp. Magnetic reconnection via current sheets. *The Physics of fluids*, 29(5):1520–1531, 1986.
- [11] D. Biskamp, E. Schwarz, and J. F. Drake. Two-fluid theory of collisionless magnetic reconnection. *Physics of Plasmas*, 4(4):1002–1009, 1997.
- [12] J. A. Bittencourt. *Fundamentals of plasma physics*. Springer Science & Business Media, 2013.

- [13] R. Borges, M. Carmona, B. Costa, and W. S. Don. An improved weighted essentially non-oscillatory scheme for hyperbolic conservation laws. *Journal of Computational Physics*, 227(6):3191–3211, 2008.
- [14] J. U. Brackbill and D. C. Barnes. The effect of nonzero γ on the numerical solution of the magnetohydrodynamic equations. *Journal of Computational Physics*, 35(3):426–430, 1980.
- [15] M. Causley, H. Cho, and A. Christlieb. Method of lines transpose: Energy gradient flows using direct operator inversion for phase-field models. *SIAM Journal on Scientific Computing*, 39(5):B968–B992, 2017.
- [16] M. Causley, A. Christlieb, B. Ong, and L. Van Groningen. Method of lines transpose: An implicit solution to the wave equation. *Mathematics of Computation*, 83(290):2763–2786, 2014.
- [17] M. F. Causley, H. Cho, A. J. Christlieb, and D. C. Seal. Method of lines transpose: High order L-stable $\mathcal{O}(N)$ schemes for parabolic equations using successive convolution. *SIAM Journal on Numerical Analysis*, 54(3):1635–1652, 2016.
- [18] M. F. Causley and A. J. Christlieb. Higher order a-stable schemes for the wave equation using a successive convolution approach. *SIAM Journal on Numerical Analysis*, 52(1):220–235, 2014.
- [19] M. F. Causley, A. J. Christlieb, Y. Guclu, and E. Wolf. Method of lines transpose: A fast implicit wave propagator. *arXiv preprint arXiv:1306.6902*, 2013.
- [20] Y. Cheng, F. Li, J. Qiu, and L. Xu. Positivity-preserving dg and central dg methods for ideal mhd equations. *Journal of Computational Physics*, 238:255–280, 2013.
- [21] A. Christlieb, W. Guo, and Y. Jiang. A WENO-based Method of Lines Transpose approach for Vlasov simulations. *Journal of Computational Physics*, 327:337–367, 2016.
- [22] A. Christlieb, W. Guo, and Y. Jiang. Kernel based high order “explicit” unconditionally-stable scheme for nonlinear degenerate advection-diffusion equations. *arXiv preprint arXiv:1707.09294*, 2017.
- [23] A. Christlieb, W. Guo, and Y. Jiang. A kernel based high order “explicit” unconditionally stable scheme for time dependent hamilton–jacobi equations. *Journal of Computational Physics*, 379:214–236, 2019.
- [24] A. Christlieb, W. Guo, Y. Jiang, and H. Yang. Kernel based high order “explicit” unconditionally stable scheme for nonlinear degenerate advection-diffusion equations. *Journal of Scientific Computing*, 82(3):52, 2020.

- [25] A. J. Christlieb, X. Feng, Y. Jiang, and Q. Tang. A high-order finite difference weno scheme for ideal magnetohydrodynamics on curvilinear meshes. *SIAM Journal on Scientific Computing*, 40(4):A2631–A2666, 2018.
- [26] A. J. Christlieb, X. Feng, D. C. Seal, and Q. Tang. A high-order positivity-preserving single-stage single-step method for the ideal magnetohydrodynamic equations. *Journal of Computational Physics*, 316:218–242, 2016.
- [27] A. J. Christlieb, Y. Liu, Q. Tang, and Z. Xu. High order parametrized maximum-principle-preserving and positivity-preserving weno schemes on unstructured meshes. *Journal of Computational Physics*, 281:334–351, 2015.
- [28] A. J. Christlieb, Y. Liu, Q. Tang, and Z. Xu. Positivity-preserving finite difference weighted eno schemes with constrained transport for ideal magnetohydrodynamic equations. *SIAM Journal on Scientific Computing*, 37(4):A1825–A1845, 2015.
- [29] A. J. Christlieb, J. A. Rossmannith, and Q. Tang. Finite difference weighted essentially non-oscillatory schemes with constrained transport for ideal magnetohydrodynamics. *Journal of Computational Physics*, 268:302–325, 2014.
- [30] B. Cockburn and C.-W. Shu. Tvb runge-kutta local projection discontinuous galerkin finite element method for conservation laws. ii. general framework. *Mathematics of computation*, 52(186):411–435, 1989.
- [31] W. Dai and P. R. Woodward. A simple finite difference scheme for multidimensional magnetohydrodynamical equations. *Journal of Computational Physics*, 142(2):331–369, 1998.
- [32] H. De Sterck. Multi-dimensional upwind constrained transport on unstructured grids for 'shallow water' magnetohydrodynamics. In *AIAA Computational Fluid Dynamics Conference, 15 th, Anaheim, CA*, 2001.
- [33] A. Dedner, F. Kemm, D. Kröner, C.-D. Munz, T. Schnitzer, and M. Wesenberg. Hyperbolic divergence cleaning for the mhd equations. *Journal of Computational Physics*, 175(2):645–673, 2002.
- [34] C. R. DeVore. Flux-corrected transport techniques for multidimensional compressible magnetohydrodynamics. *Journal of Computational Physics*, 92(1):142–160, 1991.
- [35] E. Dorfi. Numerical methods for astrophysical plasmas. *Computer Physics Communications*, 43(1):1–15, 1986.
- [36] L. Dubuc, F. Cantariti, M. Woodgate, B. Gribben, K. Badcock, and B. Richards. Solution of the unsteady euler equations using an implicit dual-time method. *AIAA journal*, 36(8):1417–1424, 1998.

- [37] C. R. Evans and J. F. Hawley. Simulation of magnetohydrodynamic flows—a constrained transport method. *The Astrophysical Journal*, 332:659–677, 1988.
- [38] M. Fey and M. Torrilhon. A constrained transport upwind scheme for divergence-free advection. In *Hyperbolic problems: theory, numerics, applications*, pages 529–538. Springer, 2003.
- [39] P. Fu, F. Li, and Y. Xu. Globally divergence-free discontinuous galerkin methods for ideal magnetohydrodynamic equations. *Journal of Scientific Computing*, 77(3):1621–1659, 2018.
- [40] S. Gottlieb, C.-W. Shu, and E. Tadmor. Strong stability-preserving high-order time discretization methods. *SIAM review*, 43(1):89–112, 2001.
- [41] A. Harten, B. Engquist, S. Osher, and S. R. Chakravarthy. Uniformly high order accurate essentially non-oscillatory schemes, iii. In *Upwind and high-resolution schemes*, pages 218–290. Springer, 1987.
- [42] C. Helzel, J. A. Rossmannith, and B. Taetz. An unstaggered constrained transport method for the 3d ideal magnetohydrodynamic equations. *Journal of Computational Physics*, 230(10):3803–3829, 2011.
- [43] C. Helzel, J. A. Rossmannith, and B. Taetz. A high-order unstaggered constrained-transport method for the three-dimensional ideal magnetohydrodynamic equations based on the method of lines. *SIAM Journal on Scientific Computing*, 35(2):A623–A651, 2013.
- [44] M. Hesse, K. Schindler, J. Birn, and M. Kuznetsova. The diffusion region in collisionless magnetic reconnection. *Physics of Plasmas*, 6(5):1781–1795, 1999.
- [45] G.-S. Jiang. Shu ch.-w.: Efficient implementation of weighted eno schemes. *Journal of Computational Physics*, 126(1):202–228, 1996.
- [46] G.-S. Jiang and D. Peng. Weighted ENO schemes for Hamilton–Jacobi equations. *SIAM Journal on Scientific computing*, 21(6):2126–2143, 2000.
- [47] G.-S. Jiang and C.-W. Shu. Efficient implementation of weighted eno schemes. *Journal of computational physics*, 126(1):202–228, 1996.
- [48] G.-S. Jiang and C.-c. Wu. A high-order weno finite difference scheme for the equations of ideal magnetohydrodynamics. *Journal of Computational Physics*, 150(2):561–594, 1999.

- [49] S. Kawai. Divergence-free-preserving high-order schemes for magnetohydrodynamics: An artificial magnetic resistivity method. *Journal of Computational Physics*, 251:292–318, 2013.
- [50] G. Laval, R. Pellat, and M. Vuillemin. Electromagnetic instabilities in a collisionless plasma; instabilites electromagnetiques des plasmas sans collisions; ehlektromagnitnye neustojchivosti besstolknovitel’nykh plazm; inestabilidad electromagnetica en un plasma sin colisiones. 1966.
- [51] R. J. LeVeque. Wave propagation algorithms for multidimensional hyperbolic systems. *Journal of Computational Physics*, 131(2):327–353, 1997.
- [52] F. Li, L. Xu, and S. Yakovlev. Central discontinuous galerkin methods for ideal mhd equations with the exactly divergence-free magnetic field. *Journal of Computational Physics*, 230(12):4828–4847, 2011.
- [53] X.-D. Liu, S. Osher, and T. Chan. Weighted essentially non-oscillatory schemes. *Journal of computational physics*, 115(1):200–212, 1994.
- [54] P. Londrillo and L. Del Zanna. High-order upwind schemes for multidimensional magnetohydrodynamics. *The Astrophysical Journal*, 530(1):508, 2000.
- [55] P. Londrillo and L. Del Zanna. On the divergence-free condition in godunov-type schemes for ideal magnetohydrodynamics: the upwind constrained transport method. *Journal of Computational Physics*, 195(1):17–48, 2004.
- [56] Z. Ma and A. Bhattacharjee. Fast impulsive reconnection and current sheet intensification due to electron pressure gradients in semi-collisional plasmas. *Geophysical research letters*, 23(13):1673–1676, 1996.
- [57] M. Mandt, R. Denton, and J. Drake. Transition to whistler mediated magnetic reconnection. *Geophysical Research Letters*, 21(1):73–76, 1994.
- [58] U. Müller and L. Bühler. *Magnetofluidynamics in channels and containers*. Springer Science & Business Media, 2013.
- [59] G. K. Parks. Physics of space plasmas-an introduction. *Redwood City, CA, Addison-Wesley Publishing Co., 1991, 547 p.*, 1991.
- [60] G. K. Parks. *Physics of space plasmas: an introduction*. CRC Press, 2019.
- [61] K. G. Powell. An approximate riemann solver for magnetohydrodynamics (that works more than one dimension). Technical report, INSTITUTE FOR COMPUTER APPLICATIONS IN SCIENCE AND ENGINEERING HAMPTON VA, 1994.

- [62] K. G. Powell, P. L. Roe, T. J. Linde, T. I. Gombosi, and D. L. De Zeeuw. A solution-adaptive upwind scheme for ideal magnetohydrodynamics. *Journal of Computational Physics*, 154(2):284–309, 1999.
- [63] E. R. Priest. MHD reconnection. *Scholarpedia*, 6(2):2371, 2011. revision #136731.
- [64] J. A. Rossmannith. An unstaggered, high-resolution constrained transport method for magnetohydrodynamic flows. *SIAM Journal on Scientific Computing*, 28(5):1766–1797, 2006.
- [65] D. Ryu, F. Miniati, T. Jones, and A. Frank. A divergence-free upwind code for multi-dimensional magnetohydrodynamic flows. *The Astrophysical Journal*, 509(1):244, 1998.
- [66] D. C. Seal, Q. Tang, Z. Xu, and A. J. Christlieb. An explicit high-order single-stage single-step positivity-preserving finite difference weno method for the compressible euler equations. *Journal of Scientific Computing*, 68(1):171–190, 2016.
- [67] M. A. Shay and J. F. Drake. The role of electron dissipation on the rate of collisionless magnetic reconnection. *Geophysical Research Letters*, 25(20):3759–3762, 1998.
- [68] C.-W. Shu and S. Osher. Efficient implementation of essentially non-oscillatory shock capturing schemes, 2. 1988.
- [69] C.-W. Shu and S. Osher. Efficient implementation of essentially non-oscillatory shock-capturing schemes, ii. In *Upwind and High-Resolution Schemes*, pages 328–374. Springer, 1989.
- [70] M. Torrilhon. Locally divergence-preserving upwind finite volume schemes for magnetohydrodynamic equations. *SIAM Journal on Scientific Computing*, 26(4):1166–1191, 2005.
- [71] G. Tóth. The $\nabla \cdot B = 0$ constraint in shock-capturing magnetohydrodynamics codes. *Journal of Computational Physics*, 161(2):605–652, 2000.
- [72] B. Udrea. *An advanced implicit solver for MHD*. University of Washington, 1999.
- [73] K. J. Vanden and D. Whitfield. Direct and iterative algorithms for the three-dimensional euler equations. *AIAA journal*, 33(5):851–858, 1995.
- [74] V. M. Vasyliunas. Theoretical models of magnetic field line merging. *Reviews of Geophysics*, 13(1):303–336, 1975.
- [75] J. R. Wilson. Some magnetic effects in stellar collapse and accretion fn1. *Annals of the New York Academy of Sciences*, 262(1):123–132, 1975.

- [76] T. Xiong, J.-M. Qiu, and Z. Xu. Parametrized positivity preserving flux limiters for the high order finite difference weno scheme solving compressible euler equations. *Journal of Scientific Computing*, 67(3):1066–1088, 2016.
- [77] Z. Xu. Parametrized maximum principle preserving flux limiters for high order schemes solving hyperbolic conservation laws: one-dimensional scalar problem. *Mathematics of Computation*, 83(289):2213–2238, 2014.
- [78] K. Yee. Numerical solution of initial boundary value problems involving maxwell’s equations in isotropic media. *IEEE Transactions on antennas and propagation*, 14(3):302–307, 1966.
- [79] A. L. Zachary, A. Malagoli, and P. Colella. A higher-order godunov method for multidimensional ideal magnetohydrodynamics. *SIAM Journal on Scientific Computing*, 15(2):263–284, 1994.
- [80] X. Zhang and C.-W. Shu. On positivity-preserving high order discontinuous galerkin schemes for compressible euler equations on rectangular meshes. *Journal of Computational Physics*, 229(23):8918–8934, 2010.